BIOGEOCHEMICAL AND HYDROLOGICAL CONTROLS OF METHANE DYNAMICS AND ECOSYSTEM FUNCTION IN A TROPICAL KARST SUBTERRANEAN ESTUARY

A Dissertation

by

DÁVID BRANKOVITS

Submitted to the Office of Graduate and Professional Studies of
Texas A&M University
in partial fulfillment of the requirements for the degree of

DOCTOR OF PHILOSOPHY

Chair of Committee,	Thomas M. Iliffe
Co-Chair of Committee,	John W. Pohlman
Committee Members,	Peter J. van Hengstum
	Jaime R. Alvarado-Bremer
	Jay R. Rooker
Intercollegiate Faculty Chair,	Anna Armitage

December 2017

Major Subject: Marine Biology

ABSTRACT

Subterranean estuaries extend into carbonate platforms where extensive cave networks influence the hydrology and biogeochemistry of the coastal aquifer. How complex biological communities thrive in this globally-distributed, cryptic ecosystem (termed anchialine) is poorly understood. This dissertation explores the role of dissolved organic carbon, with an emphasis on methane, in the carbon cycling and ecosystem function of a tropical karst subterranean estuary in the Yucatan Peninsula, Mexico. The first study presents evidence for a microbial loop that shuttles methane and other dissolved organic carbon compounds to higher trophic levels of the food web. Methane and dissolved organic carbon production and consumption within the coastal groundwater correspond with a microbial community capable of methanotrophy, heterotrophy and chemoautotrophy, based on characterization by 16S rRNA amplicon sequencing and respiratory quinone composition. Fatty acid and bulk stable carbon isotope values of cave-adapted shrimp suggest that methane-derived carbon obtained through consumption of methanotrophic bacteria comprises, on average, 21% (ranging 0-55%) of their diet. The next study identifies a biogeochemical hotspot associated with a sharp (<24 cm) anoxic-oxic density-interface between methane-charged (up to 7,793 nM) fresh and methane-poor (up to 132 nM) brackish water masses. Mixing models and kinetic isotope models that incorporate undisturbed concentration and isotopic profiles of chemical constituents across density interfaces demonstrate methane oxidation is capable of removing >95% of methane in the caves. Finally, a time-series analysis of chemical constituents and physical parameters reveals that precipitation-induced hydrologic changes affect the distribution and oxidation of methane in the caves. Between 21 and 28 mg CH_4 m^{-2} yr^{-1} are consumed during the dry season within the drainage basin of the studied subterranean estuary. Overall, findings from this dissertation provide multiple pieces of evidence for a previously unaccounted for methane sink that provides carbon and energy for an anchialine ecosystem.

ACKNOWLEDGEMENTS

I would like to thank my advisor Dr. Thomas M. Iliffe for inspiring me to explore the hidden realms of underwater cave systems and to pursue my Ph.D. at Texas A&M University at Galveston. I had the chance to participate in many adventures with him around the world on the surface, underwater, and underground – giving me remarkable memories. Special thanks to my co-advisor Dr. John W. Pohlman for his mentorship in academia and beyond. His guidance helped to me bridge ecology, my original background, with biogeochemistry, allowing me to acquire a unique skillset in biology and organic chemistry that was essential for the interdisciplinary body of work that has become my dissertation. His contribution has made me grow as a scientist and a person.

Thanks to my committee, Dr. Jay R. Rooker, Dr. Jaime R. Alvarado Bremer, and Dr. Peter J. van Hengstum, for their time, comments, and suggestions that greatly improved the final products of my research. Special thanks to Dr. van Hengstum for assisting me to acquire a better appreciation of hydrogeological processes and for helping with art work used for my presentations, dissertation, and manuscripts. In addition, I would like to express my gratitude to all key collaborators in this research project (scientists listed under contributors). Their generosity and support were essential in making this study possible.

I would like to thank Dr. José Luis Villalobos, Sergio Abdiel Benitez León, Olinka Cortes, Dr. Brett C. Gonzalez, Jacob Pohlman, Jake Emmert, Tyler Winkler, Norbert Kamarás, Rogelio Mier, Bil Phillips and István Brankovits for assistance with field expeditions in the Yucatan Peninsula, and Moody Gardens (Galveston, Texas) for supporting the cave diving operations in the field. I am grateful to the late John Hayes for productive discussions and guidance during the development and preparation of the study and the dissertation. Thanks to Dr. Patricia A. Beddows for the useful discussions and to Sean P. Sylva, Michael Casso, Adrian Mann and Ian C. Herriott for helping with laboratory analyses. Gergő Balázs and Balázs Lerner helped with video and photo

documentation of my field work. I am thankful to Linda Dezső, who encouraged me to apply for a Fulbright Scholarship that allowed me to purse my Ph.D.

I would like to thank the faculty, staff and graduate students at Texas A&M University at Galveston for their friendship and support over the years as well as for their assistance to acquire my degree. Special thanks to Dr. Antonietta Quigg, Dr. Elizabeth Borda, Dr. Patrick Louchouarn, Dr. Peter Santschi, Sarah Wall, Holly Richards, and Nicole Kinslow. Thanks to the Dive Control Board and Dive Operations for their assistance with organizing field expeditions. I was fortunate to work with my labmates, Dr. Brett C. Gonzalez, Julie Neisch, Sepp Haukebo, Jacque Cresswell, Lauren Ballou, and Fernando Calderón Guitérrez. Moreover, I am grateful for all the friendships made with the graduate students in the Department of Marine Biology and Department of Marine Sciences, as well as with people outside of the university in Galveston – as we often said, good times!

Thanks to my family and friends in Hungary who encouraged me to pursue my goals despite the distance between Texas and Europe. At some times, it was difficult to overcome this distance but I always felt their honest support. Special thanks to my father (István) who introduced me to the fascinating beauties of nature that I have never stopped exploring since he first took me diving in the sea and caving underground. Love to my mom (Rena) for her everlasting support and my brother (Bence) and sister (Sára) for inspiring me by being the special people who they are. Lastly, I am thankful for Bori, my wife, with whom I have shared this adventure. Her genuine trust and encouraging support have been the pillars of my professional and personal development.

CONTRIBUTORS AND FUNDING SOURCES

Contributors

This work was supervised by a dissertation committee consisting of Dr. Thomas M. Iliffe of the Department of Marine Biology and Wildlife and Fisheries, Dr. John W. Pohlman of the U.S. Geological Survey Woods Hole Coastal and Marine Science Center, Dr. Peter J. van Hengstum of Department of Marine Sciences and Oceanography, Dr. Jay R. Rooker of the Department of Marine Biology and Wildlife and Fisheries, and Dr. Jaime R. Alvarado Bremer of the Department of Marine Biology and Wildlife and Fisheries.

The work for the dissertation was completed by the student, in collaboration with Dr. Helge Niemann (Royal Netherlands Institute for Sea Research), Dr. Mary Beth Leigh (University of Alaska Fairbanks), Dr. Mary-Catherine Lewis (U.S. Geological Survey), Dr. Kevin Becker (Woods Hole Oceanographic Institution), Dr. Fernando Alvarez Noguera (National Autonomous University of Mexico), Dr. Laura Lapham (Chesapeake Biological Laboratory), Nick Lowell (Lowell Instruments), Dr. Erich Roth (Onset), and Dr. Moritz Lehmann (University of Basel).

Funding Sources

Graduate study was supported by a USA-Hungary Fulbright Scholarship (2011-12), a TAMUG Boost Fellowship (2015-16), and a Cave Conservancy Foundation Ph.D. Fellowship (2016-17).

This work was made possible in part by the following funding sources: TAMU-CONACYT (project no: 2015-049), The U.S. Geological Survey Greenhouse Gas Project, the Research-in-Residence Program (NSF award #1137336, Inter-university Training in Continental-scale Ecology), Cave Research Foundation Graduate Student Grant, Ralph W. Stone Fellowship (National Speleological Society), Grants-in-Aid of Graduate Student Research Award (Texas Sea Grant College Program), Exploration Fund (Explorer's Club), and Rufford Foundation Award.

NOMENCLATURE

CH_4	Methane
DIC	Dissolved Inorganic Carbon
DOC	Dissolved Organic Carbon
DOM	Dissolved Organic Matter
KSE	Karst Subterranean Estuary
MBW	Meteoric Brackish Water
MFW	Meteoric Fresh Water
OM	Organic Matter
POC	Particulate Organic Carbon
SGW	Saline Groundwater

TABLE OF CONTENTS

Page

Page

CHAPTER I
INTRODUCTION

Subterranean estuaries are coastal aquifers affected by mixing of meteoric and marine-derived groundwater (e.g., Gonneea *et al*., 2014; Moore, 2010; Santoro *et al*., 2008; Schutte *et al*., 2016). The term "subterranean estuary" was originally introduced to emphasize the importance of biogeochemical reactions in coastal aquifers affecting submarine groundwater discharge (Moore, 1999), a process that has been suggested to be the dominant pathway of dissolved terrestrial materials to the global ocean (Kwon *et al*., 2014). Karst (solutionally eroded carbonate) platforms account for ~25% of coastlines globally (Ford and Williams, 2013) and ~12% of all submarine groundwater discharge (Gonneea *et al*., 2014), making karst subterranean estuaries (KSEs) a significant component of global coastal environments. These karst platforms are characterized by unconfined coastal aquifers that have strong density stratification where sharp pycnocline(s) separate meteoric fresh- and/or brackish water layer(s) from the saline groundwater (e.g., Beddows *et al*., 2007). Chemical exchange driven by subsurface hydrology is likely to play a prominent role in mediating organic matter (OM) fluxes between the terrestrial and marine environments in subterranean estuaries (e.g., Schutte *et al*., 2016), which is especially true in karst regions where large surface streams and rivers are uncommon (e.g., Beddows *et al*., 2007; Gondwe *et al*., 2010).

Karst subterranean estuaries are characterized by flooded, dissolutional karst features, such as sinkholes, cenotes, blueholes, and cave conduits that impact the hydrology, biogeochemistry and ecology of the coastal environment (Beddows *et al*., 2007; Bishop *et al*., 2015; Gonneea *et al*., 2014). These karst features have been periodically flooded and drained by oscillating sea level (e.g., van Hengstum *et al*., 2010; van Hengstum *et al*., 2011), which has contributed to the development of a complex system of habitats and sub-habitats within KSEs around the world. The discovery of characteristic biological communities and common environmental conditions from KSEs revealed that these environments also host a globally dispersed

cryptic ecosystem, termed anchialine – meaning "near the sea" (Bishop *et al*., 2015; Iliffe and Kornicker, 2009; Stock *et al*., 1986). Biologists have characterized anchialine ecosystems based on the distribution of the characteristic stygobitic (cave-limited), mostly marine-origin invertebrate fauna – also referred to as anchialine fauna (e.g., Alvarez *et al*., 2015) – from subterranean estuaries in basaltic and carbonate platforms accessed through small water-filled pools and depressions (Hawaiian Islands), coastal tectonic faults and fissures (Galapagos Islands), flooded lava tubes (Canary Islands), cave conduits (Caribbean and the Mediterranean), and deep vertical shafts (Bahamas and Australia) (Humphreys, 1999; Iliffe and Kornicker, 2009; Kornicker and Yager, 2002; Stock *et al*., 1986). The most prevalent platforms for these ecosystems are found in porous carbonate bedrock that allows precipitation to infiltrate the coastal aquifer and marine-derived groundwater to extend inland beneath the freshwater lens (Beddows *et al*., 2007; Perry *et al*., 2002), resulting in extensive KSEs (Gonneea *et al*., 2014; Menning *et al*., 2015). The world's most extensive known anchialine ecosystem is located in Mexico's Yucatan Peninsula, which contains >1,000 km of mapped cave conduits, including the Ox Bel Ha cave system, one of the longest cave systems in the world (>240 km) (Kambesis and Coke, 2013). It is poorly understood how these complex ecosystems thrive in KSEs.

Previous ecological studies in the Yucatan Peninsula suggest that cave-limited crustaceans obtain a substantial fraction of their carbon and energy derived from chemoautotrophic sources (e.g., nitrification and methanogenesis) linked to OM degradation (Pohlman, 2011; Pohlman *et al*., 1997). Similar findings have been reported from flooded freshwater caves (Opsahl and Chanton, 2006) and sunlit sinkholes (Humphreys, 1999). However, those investigations did not consider how internal and external environmental factors control ecosystem function or the microbial ecology underlying the chemoautotrophic contributions. The current hypothesis is that habitat structuring within anchialine ecosystems is dependent on the magnitude of OM influx, which will create a eutrophic sub-habitat when OM loading is high or an oligotrophic sub-habitat when OM loading is low (Fig. 1) (Pohlman, 2011). Because oligotrophic

sub-habitats receive limited particulate OM, methane and other forms of dissolved organic matter (DOM) are more likely to be important sources of nutrition for this setting.

Within the context of the global carbon cycle, methane (CH_4) is an important carbon and energy source for many ecosystems (e.g., Bastviken *et al*., 2003; He *et al*., 2015; Levin, 2005; Niemann *et al*., 2013) and accounts for ~20% of the greenhouse gas warming effect (IPCC, 2014). Insight into methane within the carbon cycle of eutrophic and oligotrophic sub-habitats in KSEs will further constrain the importance of methane as a food source for ecosystems and a potential, as yet, unconstrained atmospheric methane source.

This research explores the role of dissolved organic carbon (DOC), with an emphasis on methane, in the carbon cycling of an oligotrophic sub-habitat within a tropical KSE in the Yucatan Peninsula, Mexico. In Chapter II, I test the hypothesis that DOC (including methane) formed from decomposition of terrestrial vegetation within water saturated limestone beneath the surface forest provides carbon and energy for microbes that support the food web of the anchialine ecosystem. This goal is achieved by measuring the distribution, concentration and isotopic composition of organic and inorganic carbon compounds, and electron acceptor availability. Microbial community is characterized by sequencing of 16S rRNA genes and identifying quinone lipid biomarkers from environmental water samples. Trophic interactions between microbes and filter feeding stygobitic shrimp are investigated using bulk and compound specific stable isotope techniques. In Chapter III, I test the hypothesis that methane consumption occurs at the anoxic-oxic interface in a density-stratified KSE. A high-resolution water sampler developed for this study is used to obtain cm-scale vertical profiles across the density interfaces. Conservative mixing models and kinetic isotope models are used to test the hypothesis. In Chapter IV, using temporal records of water chemistry and environmental parameters, I test the hypothesis that methane input and consumption within the KSE are affected by the dynamic hydrology. The multidisciplinary research

presented in this dissertation provides a broad perspective for carbon transformation and exchange, with a focus on methane dynamics, in a tropical karst subterranean estuary.

CHAPTER II

METHANE- AND DISSOLVED ORGANIC CARBON-FUELED MICROBIAL LOOP SUPPORTS A TROPICAL SUBTERRANEAN ESTUARY ECOSYSTEM[*]

Introduction

Recognition that chemosynthetic biological communities capture energy and synthesize organic matter from chemicals emitted from the seafloor (Corliss *et al*., 1979; Paull *et al*., 1984) reshaped our understanding of life on Earth (Corliss *et al*., 1981) and the oceanic carbon cycle (Levin, 2005). Organic matter (OM) produced by chemosynthetic pathways and expelled from seafloor hydrothermal vents and cold seeps may exceed 10% of surface ocean productivity (Jannasch, 1985; Levin, 2005). Submarine groundwater discharge is another important source of nutrients and carbon to the ocean (Santoro *et al*., 2008), in some instances exceeding that of rivers (Moore, 2010), and therefore represents a critical exchange vector between continental landmasses and the ocean (Kwon *et al*., 2014). However, much more is known about the magnitude of submarine groundwater discharge inputs to the coastal ocean than the genesis of the material expelled (Gonneea *et al*., 2014; Moore, 2010). Evidence that a coastal aquifer ecosystem in the Yucatan Peninsula (Mexico) is partially dependent on a chemosynthetic food source (Pohlman *et al*., 1997) suggests mutual biogeochemical reactions govern the ecology of these Earth-Ocean transitional zones, yet the basic carbon cycle in this widely distributed coastal ecosystem remains largely unexplored. In the present study, methods previously used to investigate continental-margin cold seeps (Niemann *et al*., 2013; Pohlman *et al*., 2010) are adapted to delineate the biogeochemistry and functional ecology of this coastal aquifer ecosystem.

Mixing of terrestrial meteoric water with saline groundwater in coastal aquifers resembles the two-layered circulation of surface estuaries such that they have been

[*] Reprinted with permission from "Methane- and dissolved organic carbon-fueled microbial loop supports a tropical subterranean estuary ecosystem" by Brankovits *et al*., *accepted* (expected to be published in 2017) *Nature Communications*, DOI: 10.1038/s41467-017-01776-x. Copyright 2017 by Springer Nature.

termed subterranean estuaries (Moore, 1999). Subterranean estuaries are found globally along siliciclastic, basaltic and karstic (carbonate) coastlines (Ford and Williams, 2013; Gonneea *et al*., 2014; Moore, 2010). The most prevalent and human-accessible estuary type is found within porous limestone of karst coastlines where marine-derived groundwater extends inland beneath the meteoric lens flooding extensive cave passages (e.g., Beddows *et al*., 2007; Perry *et al*., 2002; van Hengstum *et al*., 2010; van Hengstum *et al*., 2011). Karst coastlines account for ~25% of coastlines globally (Ford and Williams, 2013) and ~12% of all submarine groundwater discharge (Gonneea *et al*., 2014). Research conducted by scientific divers within cave conduits of karst subterranean estuaries has led to a basic understanding of stygobitic (cave-limited) macrofaunal biodiversity (Alvarez *et al*., 2015; Gonzalez *et al*., 2013; Iliffe and Kornicker, 2009; Rubio *et al*., 2015) within this globally distributed ecosystem (termed 'anchialine' ecosystem, meaning "near the sea") (Bishop *et al*., 2015), the food web structure (Pohlman *et al*., 1997), how sea level change during the Holocene affected the habitat development (van Hengstum *et al*., 2011) and hydrologic controls that govern the mixing of fresh and marine waters within the subterranean estuary (Beddows *et al*., 2007).

The seminal investigation of anchialine ecosystems suggested OM supporting consumers in a tropical karst subterranean estuary was partially derived from a chemoautotrophic source (Pohlman *et al*., 1997). This conclusion was based on the bulk stable carbon isotopic composition of several crustacean species that were distinct (^{13}C-depleted) from available photosynthetic sources and similar to invertebrates from deep sea vent communities that rely on a chemoautotrophic production of OM. Comparable isotopic values were reported for invertebrates from a thermomineral cave in Romania with clear evidence that mantle-derived hydrogen sulfide (H_2S) was the primary energetic source (Sarbu *et al*., 1996). However, lacking H_2S and other evidences of mantle-derived sources in oligotrophic sub-habitats of the tropical anchialine ecosystem (Pohlman, 2011), it has been suggested that non-sulfurous reduced compounds (e.g., ammonium or methane) liberated during OM decomposition support microbial

communities, but the primary OM sources were not identified definitively (Pohlman *et al*., 1997). Subsequent studies from a freshwater karst aquifer (Opsahl and Chanton, 2006), a sunlit sinkhole ecosystem (Humphreys, 1999), an alluvial aquifer (DelVecchia *et al*., 2016) and freshwater lakes (Deines *et al*., 2009) also suggest higher trophic level invertebrates utilize chemoautotrophic products generated from OM degradation, supporting the possibility that ecosystems deep within a coastal aquifer are sustained by similar processes.

In this study, I investigated the carbon cycle and food web dynamics of a pristine anchialine ecosystem within a tropical karst subterranean estuary in Mexico's Yucatan Peninsula. The Yucatan is a carbonate platform that contains more than 1,000 km of mapped cave conduits within the coastal region of the Holbox fracture zone (Kambesis and Coke, 2013) (Fig. 2). These cave passages prevail within the inland portion of the subterranean estuary over an area (~1,100 km^2) comparable to surface estuaries like Galveston Bay (Texas) (~1,500 km^2), the 7th largest estuary in the U.S. Natural sinkholes, locally known as cenotes, provide scientists direct access to the flooded caves. The study site, Cenote Bang, is located ~8 km inland within a mature dry tropical forest and is one of the entrances to the Ox Bel Ha cave network (Fig. 2).

Based on the observation that a complex food web exists in a karst subterranean estuary with limited particulate organic matter, I tested the hypothesis that dissolved organic carbon (DOC) – including methane (CH_4) – formed from decomposition of terrestrial vegetation within water saturated limestone beneath the tropical forest provides carbon and energy for a microbial loop that, in turn, supports the anchialine food web (Pohlman, 2011). Carbon sources were identified and biogeochemical cycles were inferred based on the distribution, concentration and isotopic composition of organic and inorganic carbon compounds, and electron acceptor availability. Microbial community was characterized by sequencing of 16S rRNA genes and identifying quinone lipid biomarkers from environmental water samples. To link the microbes to the food web, compound-specific isotopic analysis of membrane-derived fatty acids extracted from filter feeding cave-adapted shrimp was employed. This multidisciplinary

study provides a broad perspective for carbon transformations and exchange between the terrestrial and marine realms of a tropical karst subterranean estuary.

Methods

Study sites and seasons

Between 2013 and 2016, five field campaigns were conducted to investigate flooded cave networks accessible through Cenote Bang (the primary study site; Fig. 2) within the Ox Bel Ha cave system and secondary locations (see Supplemental Material). Three sampling events took place during the dry season (typically December through April) and two during the rainy season (typically May through November). There was no visible evidence that any of the sites had been altered by direct or indirect human activity. Access to Cenote Bang was restricted to research team members during the study. All divers involved with the project followed protocols established by the American Academy of Underwater Sciences and the National Speleological Society Cave Diving Section.

Physico-chemical water column parameters

Temperature, salinity, and dissolved oxygen (DO) were measured along vertical profiles in the water column of the caves and cenotes using a YSI XLM-600 and EXO-02 multi-parameter datasonde with a measurement frequency of 0.25-1 Hz. The sonde was carried by the lead diver, slowly descending (2-4 cm s^{-1}) and advancing with the probes projecting forward to ensure an undisturbed profile of the water column.

Sample collection and processing

Water samples for geochemical analysis of dissolved materials were collected near the sonde profile locations in plastic 60 ml syringes fitted with 3-way stopcocks. The syringes were rinsed with distilled water and dried prior to the dive, and flushed with sample water prior to closing the stopcock. Samples for particulate organic carbon (POC) and lipid analyses were collected in 10 l collapsible Nalgene carboys rinsed with

distilled water prior to the dive. Samples for microbial DNA sequencing were collected in 1 l collapsible Nalgene carboys acid washed prior to the expedition. It was not possible to rinse the carboys with sample water while underground. Because the water column in the subterranean estuary is extremely stratified, data from samples collected in this study represents the water masses, not the interfaces between them where the carbon-transforming biogeochemical reactions are expected to be most active.

Samples were kept on ice during transport to the field lab and processed within eight hours of collection. Samples for aqueous geochemistry were handled and stored according to described methods (see Supplemental Material). Among those, the serum vials for methane water samples were prepared prior to sample collection by adding the preservative (0.2 ml 1 M NaOH) into the empty vial, sealing the container with 1 cm thick butyl septa, and vacating the vial of air with a pump. The water sample was then transferred through the septum with a 20-gauge syringe needle. Water samples for POC, lipid and rRNA analyses were vacuum filtered through 47 mm diameter glass fiber filters (Gelman GF/F; 0.7 µm mesh or nominal pore size), 47 mm diameter PVDF membrane filter (Millipore hydrophilic Durapore; 0.2 µm pore size), and 47 mm diameter PES membrane filter (Pall Supor membrane; 0.2 µm pore size), respectively, until the sample was exhausted or until a reduced filtration rate indicated sufficient material was collected (2-9.5 l). The filters were transported on dry ice and stored frozen at −20 °C until further analysis. Specimens of stygobitic (cave-limited) pelagic filter-feeding atyid shrimp from the genus *Typhlatya* (*T. pearsei*, *T. mitchelli*, and one specimen of *T. dzilamensis*) were collected from six locations (see Supplemental Material). *S*urface dwelling insects were collected from the forest floor around the Cenote Bang. Within 6 hours of collection, shrimp specimens were taxonomically identified, wrapped and stored at 0 °C in prebaked (450 °C for 4 h) aluminum foil. The specimens were transported frozen on dry ice, and then stored in the laboratory at −20 °C.

Geochemical analysis

Geochemical analyses were performed at the Woods Hole Oceanographic Institution (WHOI) and U.S. Geological Survey (USGS) in Woods Hole MA, USA. Headspace methane concentrations were determined using a Shimadzu 14-A gas chromatograph (GC) equipped with a flame ionization detector (FID). Gases were isothermally (50 °C) separated with a Poraplot-Q stainless steel column (8 ft x 1/8" OD) packed with 60/80 mesh and quantified against certified gas standards with a relative standard deviation (RSD) of 2.8% or less. Headspace concentrations were converted to dissolved concentrations using described methods (Magen *et al*., 2014). The stable carbon isotope composition of methane from the headspace of the serum vials was determined using a Thermo-Finnigan DELTA^{Plus} XL isotope ratio mass spectrometer (IRMS) coupled to an Agilent 6890 Gas Chromatograph (GC) via a Finnigan GC Combustion III interface. Variable volume (1-15.0 ml) gas samples, depending on concentrations, were introduced through a gas sampling valve into a 1 ml min^{-1} He carrier gas stream. Methane and other condensable gases were trapped on fused silica capillary packed with 80/100 mesh Poraplot-Q immersed in liquid nitrogen. The gases were thermally desorbed from the column at 150 °C and separated on a 30 m, 0.32 mm ID Poraplot-Q column at −40 °C prior to being oxidized to CO_2 and analyzed by IRMS. $^{13}C/^{12}C$ ratios of methane are expressed in the standard δ-notation using tank CO_2 referenced to the Vienna Pee Dee Belemnite (VPDB) standard. The standard deviation (1 σ) of a 1% CH_4 standard analyzed at least every 8 samples was 0.3‰.

For the DOC subsamples, 1:1000 trace metal grade 12N HCl:H_2O volume (Lalonde *et al*., 2014) ratio was added prior to analysis to achieve pH <2. DOC concentration and $\delta^{13}C$ were analyzed by high-temperature combustion-isotope ratio mass spectrometry (HTC-IRMS) at the USGS-WHOI Dissolved Carbon Isotope Lab (DCIL). The DCIL HTC-IRMS system consists of an OI 1030C total carbon analyzer and a Graden molecular sieve trap interfaced to a Thermo-Finnigan DELTA^{plus} XL IRMS. Stable carbon isotope ratios are reported in the standard δ notation relative to VPDB and were corrected by mass balance to account for the analytical blank, which

was less than the equivalent of 15 µM DOC in the sample. By comparison, the blank-corrected sample DOC concentrations ranged from 15 to 851 µM. Thus, the blank correction ranged from 6-50% of sample concentrations. DOC concentration was calculated using a standard curve consisting of four potassium hydrogen phthalate (KHP) calibration standards quantified against the mass-44 peak on the IRMS (Lalonde *et al*., 2014). Peak areas were corrected for analytical blanks determined from ultrapure lab water injections. The concentration RSD was 5.5% during run 1 and 12.5% during run 2. The analytical error of the δ^{13}C-DOC analysis ranged from <0.3 to 0.6‰.

Dissolved inorganic carbon (DIC) concentrations were determined with a Model 5011 UIC coulometer and quantified relative to a seawater certified reference material (CRM). After the addition of 100 µl 20% phosphoric acid, CO_2 was stripped with UHP N_2, delivered to the analyzer and measured with an RSD of 4% relative to the CRM value (2.2 mM). Prior to the stable carbon isotope analysis of DIC, 50 µl of 85% phosphoric acid was added to the headspace of the sample vial to allow the DIC to transfer into the headspace as CO_2. Samples were shaken vigorously at least once every 15 min for 2 hours. Headspace gas from the sample vial was transferred and injected with a 100 µl glass syringe into a Hewlett Packard 5890 GC, where the CO_2 was separated isothermally (50 °C) on a Poraplot-Q capillary column (30 m, 0.32 mm ID) before isotopic analysis with the Thermo-Finnigan DELTAplus XP IRMS, as described above, with analytical error (1 σ) of 1.1‰.

Sulfate and chloride concentrations were determined using a Metrohm 881 Compact Plus ion chromatograph (IC) equipped with a Metrosep A Supp 5-250 anion column. Samples from the meteoric fresh water (MFW), meteoric brackish water (MBW) and saline groundwater (SGW) were diluted by factors of 31, 61 and 101, respectively. Peak areas for sulfate and chloride were quantified against equivalently diluted International Association for the Physical Sciences of the Oceans (IAPSO) standard seawater analyzed at the beginning of the run and after every fifth sample. Chloride concentrations (mM) were converted to mg l^{-1} and multiplied by 0.0018066 to

determine salinity (psu). The analytical error for dissolved constituents was ± 3.5% of the IAPSO standard sulfate and chloride values.

Conservative mixing calculations

Similar to other studies (Chanton and Lewis, 1999; Pohlman *et al*., 2008), conservative mixing models were used to differentiate the roles of physical mixing and *in situ* reactions on the concentration and isotopic composition of biogeochemically reactive species through the salinity gradient of the subterranean estuary. Internal production yields an excess of the constituent relative to conservative mixing between fresh and saline water endmembers, while consumption results in depletion. Conservative mixing calculations for methane, DOC, DIC and sulfate between the shallow low salinity (MFW) and deep high salinity (SGW) groundwater layers were done using an established approach (Fry, 2007), adapted for the density stratified groundwater:

$$C_{mix} = f_{MFW}\, C_{MFW} + (1 - f_{MFW})\, C_{SGW} \quad (2.1)$$

Here C denotes concentration of the relevant chemical constituent and subscripts MFW and SGW represent the respective water masses used as endmembers, whereas the subscript mix denotes the water mixture consisting of the two endmembers. The f_{MFW} is the fraction of the fresh endmember present in the mixture calculated from the chloride concentration:

$$f_{MFW} = \frac{[Cl^-]_{SGW} - [Cl^-]_{mix}}{[Cl^-]_{SGW} - [Cl^-]_{MFW}} \quad (2.2)$$

where $[Cl^-]$ denotes chloride concentrations, and the subscripts are the same as above. Using the above equations, the conservative mixing regimes for methane, DOC, DIC and sulfate were calculated, adopting as endmember concentrations the values from the low salinity water mass at shallow depths (in MFW) and high salinity water mass at the deepest accessible parts of the cave (in SGW). The large chloride concentration differences between the shallow portion of the groundwater and the deeper part permits

application of the method over a vertical length scale of meters in the subterranean estuary, in contrast to a horizontal length scale of kilometers typical of surface estuaries. In this study, chloride content was converted to and expressed as salinity (psu) by multiplying chloride concentrations (mg l^{-1}) by 0.0018066. Conservative mixing was calculated between the lowest C_{MFW} and lowest C_{SGW}, as well as between the highest C_{MFW} and highest C_{SGW} endmembers for each sampling event. These calculations are represented as conservative mixing lines (CMLs) on the salinity-property diagrams. The absolute highest and absolute lowest results of the mixing calculations are reported for each constituent across all seasons. The area in between the two reported mixing calculations is considered the general mixing field that incorporates all mixing lines (CML_{area}) where the distribution of the constituent is most likely determined by physical mixing. Positive excursion from the CML_{area} shows *in situ* production of a chemical species, whereas negative excursion demonstrates consumption.

Stable carbon Isotope mixing diagrams for methane, DOC and DIC were used to identify the isotopic composition of constituents produced in the mixing field or isotopic fractionation associated with their removal. Conservative stable isotope mixing models were calculated using described methods (Chanton and Lewis, 1999), also adapted for density-stratified groundwater:

$$\delta_{mix} = \frac{f_{MFW}\, C_{MFW}\, \delta_{MFW} + (1 - f_{MFW})\, C_{SGW}\, \delta_{SGW}}{C_{mix}} \tag{2.3}$$

where the subscripts are the same as in previous equations, and δ denotes $\delta^{13}C$ values of the constituents. Similar to the conservative approach taken above, the mixing field is determined by the two extreme conservative mixing lines that were observed when generating an ensemble of the mixing lines based on solute concentration data for all samplings.

All concentration and isotope mixing diagrams were constructed with log scale on the y-axis to illustrate the full extent of the vertical salinity gradient through the three water masses (MFW, MBW, and SGW). Log scale was also applied on the x-axis of

methane and DOC because of the extreme differences in their concentrations across the salinity gradient.

Comparing the measured values within the mixing region to the conservative mixing models allowed to estimate the percentage of methane and DOC removed in the shallow portion of the coastal aquifer. For this model, it is assumed that: (1) environmental conditions (e.g., overlying vegetation, permeable bedrock matrix, passage morphology and groundwater flow) do not change laterally in the inland portion of aquifer; (2) each sampled water layer (MFW, MBW, SGW) is representative in terms of general redox and organic matter conditions in that salinity regime across the inland portion of the aquifer; and therefore (3) the variation observed along the vertical salinity gradient is primarily the result of biogeochemical processes whose activity is horizontally homogenous; (4) the primary biogeochemical processes influencing the concentrations of DOC and methane are resulting in the production (OM degradation or methanogenesis) in the MFW and consumption (heterotrophy or methanotrophy, respectively) in the MBW. With these assumptions, the net percent loss of reduced organic carbon due to biological oxidation of methane (methanotrophy) and DOC (heterotrophy) are calculated with respect to concentrations expected if physical mixing were the only process that modulates the distribution of CH_4 and DOC in the water column, using the following equation:

$$\% \text{ constituent consumed due to oxidation} = \frac{C_{mix} - C_{MBW}}{C_{MFW}} \times 100 \quad (2.4)$$

where ($C_{mix} - C_{MBW}$) determines the reduction in the concentration of the constituent due to microbial oxidation. C_{MBW} and C_{MFW} are the averaged measured constituent concentrations in the MBW and MFW.

Environmental lipid biomarkers

Respiratory quinones are lipid-soluble components of the electron transport chain (Elling *et al*., 2016; Nowicka and Kruk, 2010) that provide information for metabolically active microbial functional groups. Respiratory quinones were extracted using a

modified Bligh and Dyer extraction (Bligh and Dyer, 1959; Popendorf *et al*., 2013) with DNP-PE-$C_{16:0}$/$C_{16:0}$-DAG (2,4-dinitrophenyl phosphoethanolamine diacylglycerol; Avanti Polar Lipids, Inc., Alabaster, AL) as internal standard and analyzed using a Thermo Q Exactive Orbitrap high resolution mass spectrometer (ThermoFisher Scientific, Waltham, MA, USA) equipped with an electrospray ion source (ESI) connected to an Agilent 1200 high performance liquid chromatography (HPLC) system (Agilent, Santa Clara, CA, USA). Detection of quinones was achieved using positive ion ESI, while scanning a *m/z* range from 100 to 1500. The mass spectrometer was set to a resolving power of 140,000 (FWHM at *m/z* 200) and to 17,500 for MS^2 scans. Every analysis was mass calibrated by lock mass correction. The full scan mass resolution setting corresponded to an observed resolution of 75,100 at the *m/z* 875.5505 of the internal standard, DNP-PE. Ion source and other full scan mass spectrometry parameters were set according to established protocols (Collins *et al*., 2016). MS^2 spectra were obtained in data dependent mode. For each MS full scan, five ions of highest intensity were selected in series using the quadrupole for MS^2 fragmentation (4 Da isolation window) with a Stepped Normalized Collision Energy of 20, 50 and 80. Analytes were separated using reversed phase HPLC on an C_8 XBridge column (2.1 × 150 mm, 5 µm particle size, Waters Corp., Milford, MA, USA) as described as described elsewhere (Collins *et al*., 2016; Hummel *et al*., 2011). Quinones were identified by retention time as well as accurate molecular mass of proposed sum formulas in full-scan mode and tandem MS fragment spectra (see Supplemental Material). Integration of peaks was performed on extracted ion chromatograms using an isolation width of 4 ppm and included the $[M + H]^+$, $[M + NH_4]^+$ and $[M + Na]^+$ ions. Quinone abundances were corrected for the relative response of ubiquinone ($UQ_{10:10}$) standard (Sigma Aldrich, St. Louis, MO, USA) versus the DNP-PE standard.

Bulk stable isotopic analysis

Prior to stable carbon isotopic analyses, particulate organic matter filters, soil and invertebrate samples were exposed to 10% HCl to remove inorganic carbon, rinsed with

ultrapure water, dried, and wrapped in baked (at 450 °C for 4 h) aluminum cups (Peterson and Fry, 1987). Fauna and soil samples were analyzed for stable carbon ($\delta^{13}C$) and deuterium isotopic contents (δD or $\delta^{2}H$), and POC for $\delta^{13}C$ at the University of Alaska Fairbanks (UAF) Stable Isotope Facility using established internal protocols. $\delta^{13}C$ values were measured by Elemental Analyzer Isotope Ratio Mass Spectrometry (EA-IRMS) using a Thermo Fisher Scientific Elemental Analyzer (Flash 2100) combined with Thermo Fisher Scientific DeltaV^{Plus} isotope ratio mass spectrometer and a Conflo IV interface. $\delta^{13}C$ values are reported in reference to international isotope standards. The 44 m/z peaks were used to quantify the C content of the sample. Samples for $\delta^{2}H$ values were analyzed on an ANCA-GSL elemental analyzer (Sercon, Crewe, U.K.) coupled to a Geo20-20 continuous flow IRMS at Iso-Analytical and on a Finnigan ThermoQuest thermochemical reactor elemental analyzer (TCEA; Finnigan ThermoQuest, Bremen, Germany) attached via a Conflo III to a Thermo Finnigan Delta^{Plus} IRMS. The analytical procedures for D analysis followed previously published protocols (Deines *et al*., 2009; Greenberg *et al*., 2007). All stable isotope ratios are reported using the delta (δ) notation expressed in units per mill (‰) and D results are expressed relative to Vienna Standard Mean Ocean Water (V-SMOW). Standard deviation of $\delta^{13}C$ was ± 0.04‰, and of δD was better than ± 1.9‰. POC concentrations were quantified by comparing the response of the mass 44 peak area from the samples to peptone standards of known carbon content.

Contribution of methane-derived carbon to the biomass

A simple two-source mixing model (Fry, 2007) was used to calculate relative contributions of methane-derived carbon and the soil-derived carbon (DOC and POC) in the shrimp tissue. The following equation was used for this calculation:

$$\% \text{ methane carbon contribution in biomass} = \frac{\delta_{shrimp} - \delta_{OM}}{\delta_{methane} - \delta_{OM}} \times 100 \quad (2.5)$$

where δ_{shrimp} is the measured $\delta^{13}C$ value of the shrimp, $\delta_{methane}$ is the average $\delta^{13}C$-CH_4 value of methane in the MFW (−66.3 ± 0.7‰; Table 1), δ_{OM} is the average $\delta^{13}C$ value of

DOC in the MFW (−28.0 ± 0.1‰), which is assumed to represent the isotopic content of soil-derived organic matter. This calculation does not consider carbon isotope fractionation by methanotrophic bacteria (Summons *et al*., 1994), the presumed dietary source of methane-derived carbon for the shrimp.

Lipid biomarkers from fauna

Compound-specific stable carbon isotopic analysis of membrane-bound fatty acids (FAs) extracted from tissue of *Typhlatya* specimens (n = 31) were performed. The examined tissue was removed from under the carapace and did not contain gut material. Lipid biomarkers were extracted according to a modification of established methods (Blees *et al*., 2014). Double bond positions were determined through analysis of their dimethyl-disulfide adducts (Nichols *et al*., 1986). Reproducibility was monitored by repeated injections and monitoring of internal standards. Reported $\delta^{13}C$ values have an analytical error of ± 1%.

Phylogenetic analysis and sequence processing

DNA was extracted from ¼ of a 47 mm diameter 0.2 µm pore size filter (Pall Supor) using a PowerViral Environmental RNA/DNA Isolation Kit (MoBio, Carlsbad, CA) following the manufacturer's recommendations. DNA was eluted into 50 µl of elution buffer and stored at −20 °C. Eluted DNA quality and quantity were evaluated on a NanoDrop ND-100 Spectrophotometer (Thermo Fischer Scientific, USA). The hypervariable V4 region of 16S rRNA was amplified using modified 515F and 806R primers (Earth Microbiome Project; April 2015). Primers for two step PCR amplicon barcoding library preparation were designed using the TaggiMatrix spreadsheet (Glenn & Faircloth 2013). Briefly, internal fusion PCR primers were constructed with the priming region for the 16S rRNA locus, a variable length tag (5-8 bp), and a 5' sequence to target for further TruSeq library preparation. The resulting PCR1 products were purified using AMPure XP Beads (Agencourt, Beckman Coulter, USA). PCR2 was used on cleaned PCR1 products to complete TruSeq library fragment and Illumina indexing.

Ampure XP cleanup was conducted, libraries were assessed for quality on a BioAnalyzer 2100, quantified on Qubit 2.0 and qPCR was conducted using the New England Biolabs Illumina Library Quantification kit. The library was sequenced on an Illumina MiSeq at the Core Facility for Nucleic Acid Analysis at the University of Alaska Fairbanks. Amplicons derived from sequencing were processed using the DADA2 R-package (Callahan *et al*., 2016). This package implements filtering of low quality sequences using Q20 individual nucleotide cutoff, merging of paired-end reads, and chimera identification. Reads less than 150 bp were removed from the analysis and only samples with more than 3000 high-quality reads were included in down-stream analyses. Taxonomic identification was assigned also in the DADA2 package using RDP (Wang *et al*., 2007) as the reference database. Functional (metabolic) groups were determined by using RDP to search for representative sequences from each of the operational taxonomical unit. Demultiplexed reads were deposited in NCBI Sequence Read Archive (SRA) database under accession number SRP109857.

Results

Water column properties

To characterize the physical and chemical environment of caves accessed from Cenote Bang (Fig. 2b), sonde profiles were collected during four sampling campaigns (Fig. 3) between 2013 and 2016 in the Ox Bel Ha Cave System. For all events, three distinct water masses were observed separated by thin (<12 cm) haloclines (H1 and H2) that were relatively constant in depth (Fig. 3). Salinity in the layer nearest the cave ceiling of the shallowest passages (~3 m water depth) ranged from 0.3 to 0.7 psu, which was slightly less than the cenote pool (0.9 to 1.8 psu). Salinity ranged from 2.0 to 2.5 psu in the middle layer, and from 34.8 to 37.6 psu in the deepest layer. Sampling of the deep saline groundwater was restricted to 22 m depth below groundwater table due to the geometry of the cave passages. To differentiate subterranean water masses, I hereafter refer to the low salinity water mass in the shallow meteoric lens as meteoric fresh water (MFW), the intermediate salinity water mass in the deeper meteoric lens as meteoric

brackish water (MBW) and the deepest water layer as saline groundwater (SGW). Moreover, the coastal sea water is referred to as SEA and the open-to-air sinkhole/cenote as POOL, recognizing that the POOL is part of the meteoric lens (Fig. 2e).

Dissolved oxygen in the MFW was at or near anoxia (0 to 15 µM) and constant in the vertical extent for each campaign. The SGW displayed the highest DO content (45 to 55 µM) (Fig. 3), but was still always hypoxic (<60 µM). The MBW showed two distinct profile types. During August 2014 and January 2015, DO was mostly invariant with depth in the MBW (22 to 29 µM). By contrast, during December 2013 and January 2016, MBW was anoxic near the shallow halocline (H1) and increased gradually with increasing depth towards the deeper halocline (H2). During the days preceding the sonde profilings, there was substantially more rainfall in December 2013 (457 mm) and January 2016 (253 mm) than during August 2014 (52 mm) and January 2015 (39 mm) (see Supplemental Material). DO in the POOL was consistently low (10 to 37 µM), but always elevated relative to the MFW and MBW during each event.

Aqueous biogeochemistry

To investigate the distribution, sources and turnover of dissolved and particulate carbon in the water masses, a total of 63 samples from the three water layers were collected and analyzed for concentration and $\delta^{13}C$ measurements of DIC, POC, DOC and CH_4, as well as sulfate and chloride concentrations. Table 1 provides average values for each parameter measured during the course of the study as a baseline for characteristic concentrations and carbon isotopic contents for each water mass, including the open-to-air cenote pool and the coastal ocean.

The anoxic-MFW had the highest methane concentrations (3,550 to 9,522 nM) with $\delta^{13}C$-CH_4 values (−66.3 ± 0.7‰; Fig. 4a-b) that are characteristic of microbial methane (Whiticar, 1999). Methane concentrations in the hypoxic-MBW (43 to 275 nM) were lower than those from the POOL (100 to 890 nM), and about an order of magnitude less than the MFW. MBW (−52.7 ± 1.9‰) and POOL (−50.6 ± 4.9‰) $\delta^{13}C$-CH_4 values were similar to each other, but substantially more ^{13}C-enriched than observed for the

MFW. The $\delta^{13}C$-CH_4 values from December 2013, following a period of exceptional precipitation (see Supplemental Material), were the most ^{13}C-enriched. The hypoxic-SGW had the lowest methane concentrations in the aquifer (37 to 208 nM) and were similar to the coastal sea values (43 to 235 nM). The $\delta^{13}C$-CH_4 values in the SGW (−56.3 ± 1.5‰) were comparable to those in nearby coastal ocean waters (−59.0 ± 2.1‰) and were ^{13}C-enriched relative to the MFW. Compared to the concentration and carbon isotopic ranges predicted from conservative (non-reactive) mixing models that use MFW and deep SGW methane endmember values (Fig. 4a-b), the intermediate depth MBW methane concentrations were lower and $\delta^{13}C$-CH_4 values were higher, indicating methane removal by oxidation (Whiticar, 1999).

Like methane, DOC concentrations were highest in the anoxic-MFW (402 to 834 µM), an order of magnitude lower in the MBW (37 to 203 µM), and lowest in the deep SGW (15 to 80 µM; Fig. 4c-d). The MFW $\delta^{13}C$-DOC values (−28.0 ± 0.1‰) were consistent with a terrestrial C3 plant origin (Peterson and Fry, 1987), the dominant vegetation in the overlying tropical forest. The SGW $\delta^{13}C$-DOC values (−26.6 ± 0.4‰) were slightly higher due to contributions from the coastal ocean (Bauer *et al*., 2001). Similar to methane, DOC concentrations in the MBW were much lower when compared to predictions from the conservative mixing model, indicating removal of DOC (Fig. 4c-d). However, for August 2014, the majority of the DOC samples displayed low $\delta^{13}C$ values (Fig. 4d), opposite of the effect expected for oxidation. Consistent with the distribution of DOC, the highest POC concentrations occurred in the anoxic-MFW (3.3 to 14.6 µM). However, POC does not contribute significantly to the total organic carbon pool, with average concentrations only 1.6% of the DOC. The $\delta^{13}C$-POC values in the MFW (−28.5 ± 0.5‰) are consistent with a tropical forest vegetation origin (Peterson and Fry, 1987).

DIC was the largest pool of carbon in the cave waters (Fig. 4e-f). Biological respiration, carbonate dissolution, and chemolithotrophic CO_2 assimilation have the potential to alter DIC concentration and carbon isotopic ratios. High concentrations of DIC in the MBW require the addition of DIC from a ^{13}C-enriched source. The most

likely source for such a large input of DIC is dissolution of carbonate, which occurs within this groundwater mixing zone (Back *et al*., 1986) and has $\delta^{13}C$ values that are approximately 0‰ (Kroopnick, 1980). Sulfate, a potential electron acceptor for OM respiration and/or the anaerobic oxidation of methane, did not vary in concentration relative to the conservative mixing diagram (see Supplemental Material).

Microbial community

To characterize the microbial community structure in the karst subterranean estuary, the open-water cenotes and the coastal ocean, 16S rRNA genes were sequenced and respiratory quinone biomarkers were analyzed from January 2016 water samples (Fig. 5). Phylogenetic affiliations were assigned based on 16S rRNA gene sequences and were grouped into metabolic groups by inferred phenotypes of representative sequences within each operational taxonomic unit. These functional groups were determined to identify microbes capable of mediating biogeochemical pathways inferred from geochemical analyses (Fig. 5a). Because the water samples were collected within the water masses and not at the interfaces between water masses (where it is hypothesized that carbon consumption is most active) the sequence data are a qualitative indicator of the microbial community composition. Nevertheless, the cenote pool, MFW and MBW showed relatively high abundances of sequences from type I (1.2 to 2.3%) and type II (<0.3%) methanotrophic bacteria, sulfur-oxidizing bacteria, and other archaeal and bacterial functional groups involved in methylotrophy as well as chemoautotrophic nitrogen and sulfur cycling processes. The abundance of methanogenic archaea was below 1%, with highest abundance in the SGW, where ammonia-oxidizing microbes were also present. Numerous other microbes capable of utilizing a wide range of organic compounds were identified (‘Others’ in Fig. 5a).

Quinone biomarkers offer DNA-independent detection and quantification of microbial biomass in samples from the natural environmental (Collins and Jones, 1981; Elling *et al*., 2016). In the collected samples, the occurrence and relative distribution of quinones were distinct for the meteoric and saline water regimes (Fig. 5b). The major

quinone types in all samples were ubiquinones (UQs) containing seven to ten isoprenoid units and one double bond per isoprenoid unit (see quinone nomenclature in Methods). Additionally, in the samples from the POOL, the MFW and MBW methylene-ubiquinone ($MQ_{8:7}$) was detected, which structurally differs from regular ubiquinones by the presence of a methylene group in the isoprenoid side chain. In the samples from the POOL and MFW, $UQ_{8:8}$ was the dominant quinone (72% relative abundance), while in the sample from the MBW $UQ_{8:8}$ and $UQ_{9:9}$ contribute 40% and 41% to total quinones, respectively. $UQ_{8:8}$, $UQ_{9:9}$ and $UQ_{10:10}$ were equally distributed in the deep saline groundwater, while in the coastal sea water $UQ_{10:10}$ was the dominant quinone with 62%. Highest quinone concentrations occurred in the POOL with 31 ng l^{-1}. In the cave, the concentrations decreased with increasing salinity across the different water regimes (MFW, MBW, SGW; Fig. 5b). The quinone $MQ_{8:7}$ is diagnostic for type II methanotrophs and $UQ_{8:8}$ has been shown to be the dominant quinone in type I methanotrophs (Collins and Green, 1985), but the latter is also widespread among other aerobic bacteria (Collins and Jones, 1981). The SGW and coastal ocean (SEA) samples, in contrast, mainly contained $UQ_{9:9}$ and $UQ_{10:10}$, which occur in diverse aerobic bacteria.

Bulk stable isotopes

To determine the trophic relationships between potential food sources and consumers, specimens (n = 29) of stygobitic *Typhlatya* spp., a pelagic atyid shrimp with feeding appendages capable of capturing bacterial sized particles (Hobbs *et al*., 1977; Pohlman *et al*., 1997) and insects (n = 4) from the surface jungle were measured for stable carbon and deuterium isotopic content (Fig. 6a). Twelve shrimp were obtained from the MBW of Cenote Bang cave. The remaining specimens (n = 17) were collected from the MBW and SGW of three locations connected (via cave conduits) with the main research site and two caves at greater distance that are not likely linked to Cenote Bang (see Supplemental Material). Shrimp stable carbon isotope values ranged from −22.5 to −49.1‰, and the stable hydrogen isotope values ranged from −95.7 to −223.6‰ (Fig. 6a). These isotope values were between the terrestrial soil/insect values and those

expected for microbial methane (Whiticar, 1999). The measured $\delta^{13}C$-CH_4 values from the cave were typical for microbial methane, and the $\delta^{13}C$-DOC values were similar to those of the soil OM.

Fatty acid biomarkers

Compound-specific stable carbon isotopic analyses of membrane-bound FAs were employed extracted from shrimp specimens (n = 31). We report FA data from two specimens with the lowest and highest stable carbon isotope values, which are assumed to represent a relatively small (3%) and large (55%) contributions of methane carbon to the specimen's biomass, as calculated from a two-source mixing model (DelVecchia *et al*., 2016; Fry, 2007). A range of C_{14}-C_{18} FAs were observed, all of which displayed $\delta^{13}C$ values similar to the specimen's bulk $\delta^{13}C$ (Fig. 6b). FA compounds extracted from the shrimp with relatively high methane contribution to its biomass (Shrimp 1; Fig. 6b) displayed more depleted $\delta^{13}C$ values than FAs from the tissue of Shrimp 2 (Fig. 6b). Both shrimp contained generic, saturated FAs with an even number of carbon atoms ($C_{14:0}$, $C_{16:0}$, and $C_{18:0}$), as well as odd number unsaturated and methylated lipid compounds.

Discussion

The results presented above demonstrate that methane and DOC derived from degraded terrestrial organic matter are the primary carbon and energy sources for an anchialine ecosystem within a karst subterranean estuary (KSE) beneath an undisturbed tropical forest (Fig. 7). Variability in the DO profiles (Fig. 3b) and carbon chemistry (Fig. 4) of the water column suggests external factors influence the spatial and temporal dynamics of the aquifer biogeochemistry. However, the emphasis of this study and the following discussion is to identify unifying characteristics for developing a generic model of ecosystem function for this terrestrially influenced KSE to be applied to other anchialine ecosystems.

The most basic physical characteristic for this coastal aquifer and others (Beddows *et al*., 2007; Humphreys, 1999) is the uniform and extreme density stratification of the 25 m deep water column. The three distinct water masses separated by two sharp haloclines were present in the cave conduits during all sampling campaigns (Fig. 3a). The physicochemical characteristics of the MFW in the cave were distinct from the POOL, which had slightly higher salinity (~1.0 psu) and oxygen (10 to 37 µM) contents. MFW occurs throughout the permeable karst aquifer (Fig. 2e); however, access to that portion of the aquifer was restricted to shallow, domed cave passages that extend vertically-upward to water depths of 5 m or less. Herein, it is argued that the MFW is of critical importance to the carbon cycle and ecosystem function of terrestrially influenced habitats within the anchialine ecosystem.

The MFW water mass is in contact with soil-derived OM within saturated fissures and pores of the shallow anoxic aquifer (Ford and Williams, 2013). Anaerobic decomposition of soil-derived OM from the overlying jungle is the most likely source of the high concentrations of DOC (665 ± 132 µM) and methane (6,466 ± 659 nM) measured in the cave-accessible MFW. The stable carbon isotopic composition of the DOC (−28.0‰) is consistent with an origin from C3 vegetation of the overlying tropical forest (Peterson and Fry, 1987). A significant correlation ($r^2 = 0.87$) between DOC and methane concentration suggests that methane and DOC originate from a similar source (see Supplemental Material); one that likely involves syntrophic interactions between fermentative bacteria and methanogenic archaea. The average MFW $\delta^{13}C\text{-}CH_4$ value (−66.3‰) is consistent with a microbial methane origin by chemoautotrophic CO_2 reduction or acetoclastic methanogenesis (Whiticar, 1999). Limited but detectable abundance of 16S rRNA gene sequences from methanogenic archaea in the MFW (Fig. 5) suggest that methane production takes place elsewhere. This further supports the hypothesis that the saturated zone within the permeable rock matrix (Ford and Williams, 2013; Perry *et al*., 2002), a portion of the KSE that was inaccessible to divers, was the most likely source of DOC in the MFW.

The juxtaposition of OM-charged, near-anoxic MFW against OM-poor, hypoxic-MBW is analogous to redox transitions present near sediment-water interfaces (Boetius and Wenzhofer, 2013), the chemocline of meromictic lakes (Bastviken *et al*., 2008), and oxygen-minimum zones in the ocean (Canfield *et al*., 2010), with the important exception that the relative positioning of the water masses within this KSE is inverted, or 'upside-down', relative to open-water systems. High-OM, low-oxygen regimes in sediments and the water column of lakes and oceans are driven by pulses of sinking particulate detritus produced in surface waters or within the watershed basin. The accumulation and consumption of organic detritus depletes oxygen below the chemocline. For OM oxidation to continue, oxygen or alternate electron acceptors (e.g., sulfate, nitrate, etc.) must be replenished by mixing. By contrast, in the studied tropical KSE, depleted oxygen (Fig. 3b) co-occurred with concentrated methane (Fig. 4a) and DOC (Fig. 4c) above the shallow chemocline. The relatively high concentrations of oxygen in the deepest sampled portion of the aquifer (SGW) is consistent with the transport of DO with sea water moving inland from the coast below the deeper halocline (Beddows *et al*., 2007). Distinct DO profiles preceded by periods of high and low rainfall (Fig. 3b) suggest precipitation is the key external factor regulating electron acceptor availability in the meteoric portion of the aquifer. I hypothesize that rainfall injects oxygenated water into the MBW at discrete entrances by point recharge, and drives DOC-enriched water from the anoxic saturated portion of the aquifer (the MFW) into the caves by diffuse recharge (Ford and Williams, 2013).

Previous studies in caves suggest POC concentrations are limited in karst groundwater (Simon *et al*., 2003; Simon *et al*., 2007). To evaluate POC bioavailability and origin in this KSE, concentrations and $\delta^{13}C$ values of POC were measured for June 2015 and January 2016 (see Supplemental Material) and they were compared to DOC concentrations and $\delta^{13}C$ values in the cave environment (Table 1). Like DOC, POC is most abundant in the MFW (10.9 µM) and derived from the tropical forest vegetation, as indicated by its stable carbon isotopic composition ($\delta^{13}C = -28.5‰$). However, on average, DOC in the MFW is 60 times more abundant than POC. By comparison,

DOC:POC ratios range between 6 and 10 in the surface ocean, rivers and streams (Wetzel, 1984). In the oligotrophic waters of the Atlantic Ocean, where DOC:POC ratios from 300 m water depth (Bauer *et al*., 2001) are comparable to the MFW, DOC is the primary source of carbon available to a microbial loop that supports the pelagic ecosystem (Fenchel, 2008). I conclude, as others have for cave streams (Simon *et al*., 2007), some riverine systems (Meyer, 1994) and oligotrophic oceans (Fenchel, 2008), that DOC is a more important source of carbon and energy than POC for this coastal aquifer ecosystem.

Carbon-based concentration and isotopic mixing models (Fig. 4) provide insight into evaluating if and where different carbon stocks are created or consumed within a mixing system. This approach has been used to investigate carbon dynamics in estuaries (Chanton and Lewis, 1999) and high-salinity marine pore waters (Pohlman *et al*., 2008). This concept was applied to the KSE, and it was calculated using equation (2.4) that, on average, 93% of the methane (Fig. 4a) and 76% of the DOC (Fig. 4c) were removed within the MBW. The methane concentration reduction was 6,300 nM and the DOC reduction was 530 µM, on average, suggesting there is an active sink for methane and bulk DOC. During oxidation of methane and DOC, CO_2 is certainly produced, but the production of ^{13}C-enriched DIC in the MBW resulting from carbonate dissolution (Back *et al*., 1986) overwhelms the isotopic effect from the respired CO_2 (Fig. 4e-f).

Enrichment of ^{13}C in the methane within the MBW is consistent with microbial oxidation being the removal mechanism. During enzymatic oxidation of methane, there is a bias towards utilization of the ^{12}C-isotope, leaving the residual methane ^{13}C-enriched (Whiticar, 1999), as observed here. By contrast, although the concentration based mixing model for DOC indicates removal (Fig. 4c), a large positive carbon isotopic shift was not observed for the December 2014 data (Fig. 4d). This observation does not, however, conflict with the model evidence because isotopic fractionation of DOC during aerobic oxidation (Bauer and Druffel, 1998) is less than what occurs during methane oxidation (Whiticar, 1999). The negative shift in the $\delta^{13}C$ of DOC for the August 2014 sampling event suggests production of DOC from methane carbon (Pohlman *et al*., 2010).

Conservative mixing of sulfate during all sampling events (see Supplemental Material) indicates that sulfate reduction did not considerably contribute to the dissolved organic matter oxidation, but this analysis may not be sufficiently sensitive to detect changes of sulfate relative to carbon pools with orders of magnitude lower concentrations. The presence of DO in the MBW is additional evidence that methane and DOC oxidation were aerobic.

Analyses of microbial community structure (16S rRNA) and respiratory quinones reveal a diverse microbial community with distinct structuring within the groundwater, the open-water cenote and the coastal ocean (Fig. 5). Sequences representing microbes that consume methane, utilize sulfur-and nitrogen-based electron acceptors to oxidize OM, as well as sulfur-oxidizers were relatively abundant in the freshwater portion of the aquifer (MFW) and sinkhole (POOL). In particular, type I methanotroph sequences from the genus *Methlyococcacea* were present in the POOL, as well as the MFW and MBW water masses where geochemical data clearly indicate methane oxidation (Fig. 4).

The presence of respiratory quinones, which are lipid-soluble components of the electron transport chain (Elling *et al*., 2016; Nowicka and Kruk, 2010), provide evidence for metabolically active microbial functional groups in the KSE. The most prevalent quinones are affiliated with aerobic heterotrophic bacteria (Fig. 5b), which is consistent with the metabolic capacity of most microbes observed ('Others' in Fig. 5a) and with DOC being the most abundant form of OM consumed. In the meteoric water masses, the predominant quinone was $UQ_{8:8}$, which only occurs in strictly aerobic and facultatively anaerobic (grown under aerobic conditions) organisms and is the dominant quinone in type I methanotroph cultures (Collins and Green, 1985). This compound peaked in abundance in the MFW and POOL, locations where also the highest 16S rRNA copy numbers of type I methanotrophs were found (Fig. 5). Detectable concentration of the quinone biomarker $MQ_{8:7}$, which has only been found in type II methanotrophs (Collins and Green, 1985), was also present in the portion of the groundwater where methane was oxidized. The dominance of type I methanotrophs over type II methanotrophs is not surprising, because they are generally more prevalent in environments with low oxygen

(Steinle *et al*., 2015), like those observed in this KSE, and are more efficient at converting methane carbon to biomass than are type II methanotrophs (He *et al*., 2015).

Sequences from numerous genera that mediate chemoautotrophic carbon fixation and utilization through oxidation and reduction of sulfur- and nitrogen-based compounds were also present in the open-air cenote and cave (Fig. 5). However, there is presently no evidence that these microbes contribute to the carbon cycle or food web of the studied caves. A sulfate mixing model similar to the carbon mixing models (Fig. 4) did not indicate removal of sulfate in the cave (see Supplemental Material). Furthermore, none of the investigated passages contained detectable hydrogen sulfide. By contrast, deep open-water cenotes found in the Yucatan Peninsula where organic debris accumulates near the deeper halocline are most certainly settings where the carbon and sulfur cycles are intertwined (Socki *et al*., 2002). Microbes from those areas may have been transported into the interior of the Yucatan platform. Alternatively, a cryptic sulfur cycle is active (Canfield *et al*., 2010) or the mixing model lacks the sensitivity required to detect changes in sulfate concentration. Nitrification within the mixing zone of the MBW and SGW has been suggested as another potential chemoautotrophic source of OM in anchialine ecosystems in the study region (Pohlman *et al*., 1997). Near this interface, the coexistence of ammonia oxidizers typically found in either marine (*Nitrosopumilus*) or terrestrial environments (*Nitrososphaera*) were observed (Fig. 5). However, given the relatively low concentrations of nitrate (18.6 µM) accumulated near the MBW-SGW interface (Pohlman *et al*., 1997) relative to the amount of DOC consumed (530 µM), and the low carbon assimilation efficiency of nitrifying bacteria, the likelihood that nitrification contributes meaningful nutritive carbon to the food web remains speculative (Pohlman *et al*., 1997). Nevertheless, the sequence data are consistent with the hypothesis that multiple biogeochemical cycles utilizing all available electron donors and acceptors are active in these oligotrophic and anoxic/hypoxic systems (Pohlman, 2011). Additional studies are required to evaluate their importance for the food web. Data presented here support that DOC (including methane) derived

from decomposition of terrestrial organic matter, is the prevalent source of nutritive carbon that sustains the ecosystem.

Bulk stable carbon and hydrogen isotopic data from *Typhlatya* spp. shrimp adapted to feed on bacterial-sized, suspended matter in the water column (Pohlman *et al*., 1997) are consistent with a mixed dietary-dependence on methane- and DOC-derived carbon (Fig. 6a) via the consumption of microbial biomass. Considering the range of shrimp tissue δ^{13}C-values (−23 to −49‰), and the average MFW δ^{13}C values of methane (−66.3‰) and DOC (−28.0‰) (Table 1) as potential endmembers of the shrimp's dietary carbon source, the contribution of methane carbon for the shrimp ranges from 0 to 55%, with an average contribution of 21%. Studies from a humic lake (Kankaala *et al*., 2006) and an alluvial aquifer (DelVecchia *et al*., 2016) report methane carbon contributions to zooplankton and insects ranging from 5 to 67%. Because the low δD values in the shrimp are distinctive for methane carbon incorporation (Grey, 2016), it was possible to use the shrimp bulk isotope values to estimate the δD signature of the methane source. By extrapolating the carbon and deuterium stable isotope values from the cave shrimp to the average MFW δ^{13}C-CH_4 source value (−66.3‰), it is estimated that the δD-CH_4 signature was about −390‰, which allowed to constrain that the microbial methane was produced by acetoclastic methanogenesis (Whiticar, 1999).

Methane and DOC-derived carbon flow into the anchialine food web is facilitated by trophic-interactions between the shrimp and its microbial food source. To examine the biochemical origins of the ^{13}C-depleted values of the bulk shrimp tissue, the composition and carbon isotopic content of FA biomarkers extracted from shrimp with the largest (55%) and smallest (3%) calculated methane contributions were analyzed (Fig. 6b). The composition and δ^{13}C-values of FAs differed substantially between the two shrimp, which is consistent with assimilation of different food and carbon sources. In addition, in both specimens, individual FAs differed in their stable carbon isotopic composition, which is indicative of different biochemical pathways for FA synthesis (Niemann *et al*., 2013). Even-chained saturated FAs ($C_{14:0}$, $C_{16:0}$, and $C_{18:0}$) had compound-specific δ^{13}C values closely matching the bulk tissue (Fig. 6b), suggesting the

shrimp synthesized these compounds *de novo* from their dietary carbon sources. In contrast, several mono-unsaturated FAs in both shrimp and methylated FAs in shrimp 1, showed substantially more negative δ^{13}C-values than the bulk tissue (Fig. 6b), which provides evidence for a dietary source of these compounds through the direct transfer of FAs from ingested bacteria (Dalsgaard *et al*., 2003; Niemann *et al*., 2013). Given the strong geochemical evidence for aerobic methane oxidation (Fig. 4) in the hypoxic environment, the source of ^{13}C-depletion in the FAs is attributed primarily to methane carbon derived from methanotrophs. Stable isotope probing experiments using arctic lake sediments have shown that several compounds present in the shrimp tissue ($C_{14:0}$, $C_{16:1\omega7}$ and $C_{18:1\omega7}$) are synthesized from methane carbon by methanotrophs that were also present in the cave waters (e.g., *Methylococcaceae* and *Methylocystacea*; He *et al*., 2015). These FAs and the methylated FAs are also found in other organisms, but are not likely to have the ^{13}C-depleted isotope signatures observed here. A symbiotic source (Pakes *et al*., 2014) of the incorporated bacterial biomass might also explain the observed FA profiles. However, *Typhlatya* shrimp appendages capable of direct filter-feeding of bacterial-sized particles (Pohlman *et al*., 1997) suggest the methanotrophic biomass is incorporated from the environment rather than from symbiotic sources. These observations have significant implications for understanding energy transfer within the anchialine food web. Considering that *Typhlatya* spp. are one of the most abundant macrofaunal populations in this ecosystem (Alvarez *et al*., 2015), and they are the primary prey for predators in the subterranean food web (Koenemann *et al*., 2007), it is reasonable to assume they have a significant role in transferring methane- and DOC-derived carbon to higher levels of the food web.

The geochemical, genomic and biomarker evidence from this study supports the hypothesis that a subterranean microbial loop is active in a KSE (Fig. 7). It is demonstrated that DOC and methane produced from soil-derived OM degradation within the shallow, anoxic saturated zone of the karst are transported downwards into hypoxic cave conduits, where methanotrophs and heterotrophs consume these reduced OM forms and co-exist with a host of chemoautotrophs. The presence of fatty acids in somatic

tissues of filter-feeding pelagic-dwelling shrimp that could only originate from microbes is strong evidence that microbial biomass is directly transferred to higher order metazoans. This microbial loop is unique from that of the oligotrophic oceans in that it contains a methane sink, but is likely to be similar to other groundwater systems where evidence for a similar biogeochemistry has been reported (DelVecchia *et al*., 2016; Opsahl and Chanton, 2006; Schutte *et al*., 2016). The generic model of ecosystem function presented here provides baseline information for future studies aiming to quantify the magnitude of this unaccounted for 'upside-down' methane sink and to describe the external factors that alter the internal biogeochemistry of subterranean estuaries within karst coastal aquifers.

CHAPTER III
METHANE OXIDATION DYNAMICS IN A KARST SUBTERRANEAN ESTUARY

Introduction

Density-stratified coastal aquifers within siliciclastic and carbonate platforms are highly structured aquatic environments with sharp physicochemical gradients (Beddows *et al*., 2007; Pohlman *et al*., 1997; Schutte *et al*., 2016). Analogous transitional zones are found in estuaries (Chanton and Lewis, 1999), hydrothermal vents (Corliss *et al*., 1979; Paull *et al*., 1984), deep-sea cold seeps (Levin, 2005), and meromictic lakes (Bastviken *et al*., 2008). These ecotones host hotspots of biogeochemical activity where the interchange of matter between biotic and abiotic components influences elemental cycling and shapes ecosystems (Preheim *et al*., 2016). Similar processes are likely to occur within an ecotone habitat where meteoric fresh water mixes with marine-derived groundwater in subterranean estuaries of karstic coastal aquifers, or karst subterranean estuaries (Pohlman, 2011). Because nutrient transport and elemental cycling along many coastlines are influenced by material exported from subterranean estuaries (Kwon *et al*., 2014; Moore, 2010; Santoro *et al*., 2008), investigating biogeochemical processes associated with density stratification within these habitats may provide insight into an important component of the coastal ocean carbon cycle.

Isolation of energy-yielding organic compounds (electron donors) from electron accepting agents of cellular respiration by density interfaces (pycnoclines) maintained by thermal and salinity gradients impacts organic matter (OM) transformations and carbon flow in aquatic ecosystems. In meromictic lakes and reservoirs where water masses are permanently stratified, 20-60% of the organic carbon produced in surface waters is transported to the anoxic hypolimnion (Bastviken *et al*., 2008). A fraction of this sequestered carbon is transformed into methane (CH_4) by sedimentary or water column methanogenesis (Wetzel, 2001). That methane is either oxidized and returned to the

lake's carbon cycle (Bastviken *et al*., 2004), where it has been shown to contribute carbon and energy to the limnic food web (Bastviken *et al*., 2003; He *et al*., 2015), or it may transfer to the atmosphere (Bastviken *et al*., 2011) where it is a greenhouse gas 25 times more potent than carbon dioxide on a 100-year time scale (IPCC, 2014).

Density stratification also occurs in highly permeable, unconfined coastal aquifers where low and high salinity water masses mix in the subterranean estuary. This hydrogeological setting limits mixing and promotes meromictic conditions where a meteoric lens permanently overrides marine-derived saline groundwater (Beddows *et al*., 2007; van Hengstum *et al*., 2011). Karst platforms account for 25% of coastlines globally and frequently contain dissolutional karst features, such as sinkholes and cave passages (Ford and Williams, 2013). These features permit scientists to observe and sample the stratified groundwater from within the aquifer. The dramatic salinity-dominated pycnocline between the meteoric lens and saline groundwater has been the focus of most hydrogeological (Beddows *et al*., 2007; Coutino *et al*., 2017; Kambesis and Coke, 2013; Perry *et al*., 2002) and biological (Alvarez *et al*., 2015; Humphreys, 1999; Iliffe and Kornicker, 2009) research in this environment. Other studies suggest rates of OM decomposition and associated elemental cycles that include inorganic nitrogen and sulfur species are enhanced at the meteoric-saline halocline of sinkholes and interior caves (Humphreys, 1999; Pohlman, 2011; Socki *et al*., 2002). Additional stratification occurs along salinity gradients within the aforementioned meteoric lens (Humphreys, 1999; Kovacs *et al*., 2017). Because these groundwater features are extremely stratified, high-resolution vertical sampling is required to document changes in water chemistry across the chemocline (Seymour *et al*., 2007).

The Yucatan Peninsula's carbonate platform contains an extensive karst subterranean estuary (KSE) with density stratification in the groundwater (Bauer-Gottwein *et al*., 2011) and the highest known accumulation of drowned cave passages on Earth (Kambesis and Coke, 2013). The environment supports a rich and globally-dispersed anchialine (meaning "near the sea") ecosystem (Iliffe and Kornicker, 2009; Stock *et al*., 1986) consisting primarily of crustaceans (Alvarez *et al*., 2015) that are

specifically adapted to the mostly oligotrophic KSE (Bishop *et al*., 2015; Iliffe and Kornicker, 2009; Stock *et al*., 1986). A recent biogeochemical study carried out in a Yucatan Peninsula cave system ~8 km from the coastline (Fig. 8) suggests the resident anchialine ecosystem is sustained by a microbial loop that assimilates methane and other forms of dissolved organic matter (DOM) and feeds a complex food web (see Chapter II). The water column in these flooded caves is characterized by distinct fresh-, brackish- and saline-water layers, limited particulate OM, and high DOM in the fresh-water portion of the water column. The DOM is created during the anaerobic decomposition of terrestrial vegetation within overlying saturated carbonate rock-matrix, and is presumably consumed by microbes at the interface between the anoxic (<15 µM) fresh and hypoxic (>30 µM) brackish water masses (Fig. 8c-d). The environmental conditions within the oligotrophic (OM-limited) DOM-based cave ecosystems investigated in this study are to be distinguished from sinkholes and other eutrophic groundwater sub-habitats where detrital inputs from nearby surface sources drive the deeper brackish and marine-derived water masses to strict anoxia (e.g., Pohlman, 2011; Socki *et al*., 2002).

In this study, I test the hypothesis that methanotrophy occurs at the anoxic-oxic interface in the meromictic coastal aquifer within the Yucatan Peninsula karstic platform (Mexico). The OctoPiPi water sampling device, developed for this study, was used to obtain pristine cm-scale chemical profiles across pycnoclines within cave passages of the KSE. Concentration and stable carbon isotopic values of methane collected along the full salinity spectrum will be used to construct conservative mixing and kinetic isotope models to differentiate changes in concentrations and carbon isotope ratios imposed by physical mixing between water masses from those caused by microbial production and consumption of methane. Methane plays a prominent role in ecosystem dynamics (Bastviken *et al*., 2003; Deines *et al*., 2009; DelVecchia *et al*., 2016; Devlin *et al*., 2015; Grey, 2016), the global carbon cycle (Bastviken *et al*., 2011; Boetius and Wenzhofer, 2013) and the atmospheric greenhouse gas inventory (IPCC, 2014; Reeburgh, 2007). This study has the potential to define how methane dynamics within karst subterranean estuaries influence anchialine ecosystems and remove methane – a potent greenhouse

gas – from groundwater prior to its expulsion into the coastal ocean, evasion into overlying tropical soils, and, ultimately, the atmosphere.

Methods

Study sites and sampling periods

Field campaigns were conducted in January 2015 and January 2016 to investigate methane oxidation dynamics across density stratified pycnoclines in flooded caves accessed through the Cenote Bang sinkhole (20° 12.62' N 87° 30.064' W) within the Ox Bel Ha cave system south of Tulum, Quintana Roo, Mexico (Fig. 8a-b). This region is located on the Caribbean coast of the Yucatan Peninsula where the karst (solutionally eroded carbonate) topography is characterized by low elevations and an absence of surface streams and rivers due to the high permeability of the karst bedrock, resulting in vertical drainage (e.g., Beddows *et al*., 2007; Perry *et al*., 2002). Here, abundant cave passages are found in the KSE over a substantial area (~1,100 km^2). Cenote Bang provides access to a meromictic (permanently stratified) subterranean aquatic environment with a shallow (<4.5 m), meteoric fresh water (MFW) layer (<0.5 psu), an intermediate (4.5-20 m) meteoric brackish water (MBW) layer (0.5-30.0 psu), and deep (>20 m), saline groundwater (SGW) (30.0-35.0 psu) (Fig. 8c-d). In both years, sampling was conducted during the dry season (December to April/May) for this seasonally dry tropical forest (Curtis *et al*., 1996; Kottek *et al*., 2006). Dissolved oxygen concentrations were relatively lower, especially in the MBW, in 2016 than in 2015. The caves investigated in this study had no visible evidence of direct or indirect human alterations, and therefore are presumed to represent a pristine anchialine ecosystem.

Sample collection and processing

Sampling was carried out by scientifically-trained SCUBA divers following diving and safety protocols established by the American Academy of Underwater Sciences and the National Speleological Society-Cave Diving Section. Water samples were obtained at cm-scale vertical resolution across the MFW-MBW and MBW-SGW

transition zones (haloclines) using the OctoPiPi (OPP) water sampling system developed by the United States Geological Survey (USGS) (Fig. 9). The OPP samplers used in this study consist of a rack of ten 60 ml plastic syringes mounted and evenly distributed along an aluminum frame with a mechanical, spring-powered trigger-system that fills syringes when activated. An OPP with fixed 12 cm syringe spacing (Fig. 9) and another with 2.5 cm syringe spacing (the mini-OPP) were deployed during this study. The OPPs were mounted vertically across interfaces identified visually during deployment and by depth from salinity profiles collected prior to deployment (Fig. 8c). The OPPs were left in place for at least 24 h to allow the water column to re-stratify before being triggered. The top-mount of the OPP was connected to either an inflated dive lift bag or elastic bands carefully attached to the cave ceiling. The bottom-mount was connected to 1/8" braided nylon line deployed by dive reel and attached to at least 5 kg of lead weights. When triggered, the OPP slowly and simultaneously filled the syringes to a volume of 40-60 ml depending on OPP geometry. The 60 ml syringes were fitted with 3-way stopcocks that were closed immediately after OPP triggering to contain the samples. Prior to deployment, the syringe assemblies were rinsed thoroughly with distilled water and completely dried.

Following OPP recovery, the syringes were stored on ice during transport to the field lab, where they were processed within eight hours of collection following protocols described in Chapter II. Briefly, the 60 ml water sample was divided into subsamples for further geochemical analyses of dissolved constituents, including, but not limited to, methane, dissolved inorganic carbon, dissolved organic carbon, inorganic nutrients and ions. For the present study, chloride and sulfate ion concentrations as well as methane concentrations and $\delta^{13}C$ values are reported. Samples for ion analysis were filtered through a 0.45 µm Acrodisc® syringe filter and collected in a 2 ml plastic screw-top vial. 30 ml serum vials for methane water samples were prepared prior to sample collection by adding 0.5 ml 8 M NaOH into the empty vial as a preservative, sealing the container with 1 cm thick butyl septa, and vacating the vial of air with a pump. An unfiltered 20 ml water sample was then transferred from the syringe into the serum vial

by piercing the septum with a 20-gauge syringe needle and regulating water flow with the stopcock. Water samples were stored in the fridge at 7 °C.

Geochemical analysis

Geochemical analyses were performed at the Woods Hole Oceanographic Institution (WHOI) and U.S. Geological Survey (USGS) in Woods Hole MA, USA. After balancing the headspace of the serum vial for methane analysis to 1 atmosphere with helium, headspace methane concentrations were determined using a Shimadzu 14-A gas chromatograph (GC) equipped with a flame ionization detector (FID). The gases were isothermally (50 °C) separated with a Poraplot-Q stainless steel column (8 ft x 1/8" OD) packed with 60/80 mesh and quantified against certified gas standards with a relative standard deviation (RSD) of 2.8% or less. Headspace concentrations were converted to dissolved concentrations using an established method (Magen *et al*., 2014). The stable carbon isotope composition of methane from the headspace of the serum vials was determined using a Thermo-Finnigan DELTA^{Plus} XL isotope ratio mass spectrometer (IRMS) coupled to an Agilent 6890 Gas Chromatograph (GC) via a Finnigan GCCIII combustion interface. Variable volume (1-15.0 ml) gas samples, depending on concentrations, were introduced through a gas sampling valve into a 1 ml min^{-1} He carrier gas stream. Following an established method (Popp *et al*., 1995) with modifications, methane and other condensable gases were trapped on fused silica capillary packed with 80/100 mesh Poraplot-Q immersed in liquid nitrogen. The gases were thermally desorbed from the column at 150 °C and separated on a 30 m, 0.32 mm ID Poraplot-Q column at −40 °C prior to being oxidized to CO_2 and analyzed by IRMS. The $^{13}C/^{12}C$ ratios of methane are expressed in the standard δ-notation using tank CO_2 referenced to the Vienna Pee Dee Belemnite (VPDB) standard. The standard deviation (1 σ) of a 1% CH_4 standard analyzed at least every 8 samples was 0.3‰.

Sulfate and chloride concentrations were determined using a Metrohm 881 Compact Plus ion chromatograph (IC) equipped with a Metrosep A Supp 5-250 anion column. Samples from the MFW, MBW and SGW were diluted by factors of 31, 61 and

101, respectively, to bring the chloride concentrations to within the range of the conductivity detector. Peak areas for sulfate and chloride were quantified against equivalently diluted International Association for the Physical Sciences of the Oceans (IAPSO) standard seawater analyzed at the beginning of the run and after every fifth sample. Chloride concentrations (mM) were converted to mg l^{-1} and multiplied by 0.0018066 to determine salinity (psu). The analytical error for dissolved constituents was ± 3.5% of the IAPSO standard sulfate and chloride values. Mean values of sulfate to chloride ratios from the environment are reported with standard error.

Conservative mixing calculations

Conservative mixing models were used to differentiate the roles of physical mixing and *in situ* biogeochemical reactions on the concentration and isotopic composition of methane through the salinity gradient. This approach has been used to investigate carbon dynamics in estuaries (Chanton and Lewis, 1999) and varying-salinity marine pore waters (Pohlman *et al*., 2008). For details about the conservative mixing models and determination of methane offset from the models, see detailed description in Chapter II. Briefly, the conservative mixing model was calculated using salinity endmembers and the corresponding methane data. Profiles that incorporated the MFW-MBW and MBW-SGW transition zones were used to determine the low salinity endmember from the MFW and the high salinity endmember from the SGW. *In situ* production yields an excess of the constituent relative to the conservative mixing model, while consumption results in depletion. Applying this mixing model for each OPP deployment, it was possible to determine the fraction of methane reduction by methanotrophic processes relative to the fraction of methane reduction expected from mixing.

Kinetic isotope models

Measured $\delta^{13}C$ values and concentrations of methane were incorporated into kinetic isotope models to delineate if changes in the carbon isotope ratios were due to

oxidation or mixing with other methane sources. During methane oxidation, the kinetic isotope effect causes the residual methane to become increasingly enriched with ^{13}C relative the source value (Barker and Fritz, 1981; Whiticar, 1999). Consequently, it is possible to describe coupled shifts in methane concentrations and $\delta^{13}C$ values during oxidation with the "closed system" Rayleigh isotopic fractionation model (Damm *et al*., 2007; Leonte *et al*., 2017) and "open system" isotope models (Kessler *et al*., 2006; Leonte *et al*., 2017). The Rayleigh model assumes the methane oxidation process follows first-order reaction kinetics and occurs in a "closed" water parcel, where microbial methane oxidation is the only process that alters the $\delta^{13}C$ values of the methane. This model assumes no mixing with other methane-rich waters; however, if mixing occurs with waters containing methane concentrations so low that the mixing does not substantially alter the $\delta^{13}C$ of the bulk pool, the closed system assumption of the Raleigh model remains valid. In contrast, "open system" models account for mixing of waters with different methane content. This model assumes that $\delta^{13}C\text{-}CH_4$ values are influenced by contribution from methane-laden water(s), methane oxidation, and removal of methane within an "open" water parcel.

Coupled application of the Rayleigh and open system kinetic isotope models (e.g., Leonte *et al*., 2017) enables one to distinguish loss of methane through the MFW-MBW transition zone to either methane oxidation or dispersion from other sources. Data from the OPP vertical profiles at the MFW-MBW transition zone (where evidence for methane oxidation is available) will be incorporated into these models in a manner similar to that developed by Leonte *et al*. (2017) to evaluate the fate of methane releases from seafloor seeps in the Hudson Canyon of the U.S. Atlantic Margin.

Model equations for the Rayleigh, Eq. (3.1), and open system, Eq. (3.2), are:

$$f_c = 1 - \left(\frac{\delta R+1000}{\delta R_0+1000}\right)^{\left(\frac{\alpha_c}{1-\alpha_c}\right)} \tag{3.1}$$

$$f_o = \frac{\alpha_o}{1-\alpha_o}\left(\frac{\delta R_0+1000}{\delta R+1000} - 1\right) \tag{3.2}$$

where f is the fraction oxidized, α is the isotope fractionation factor, subscripts c and o refer to the closed and open system models, respectively, δR_0 is the source (or initial) $\delta^{13}C\text{-}CH_4$ value at the time of emission from the cave ceiling, δR is the $\delta^{13}C\text{-}CH_4$ value at a later time. The selected δR_0 value (−67.49‰) is the average $\delta^{13}C$ value for methane from a sample with the highest methane concentration (7,793 nM) and a $\delta^{13}C$ value of −67.48‰ and a sample with the lowest $\delta^{13}C$ value (−67.51‰) and a concentration of 7,295 nM.

Following the method described by Leonte *et al*. (2017) and using the stable carbon isotope value of the source endmembers described above (C_0 = 7,544 nM; δR_0 = −67.49‰), the measured methane properties from the OPP profile at the MFW-MBW interface, and linearization of Eq. (3.1) and Eq. (3.2) to determine the fractionation factor (α) (Fig. 10), it was possible to calculate the fraction of methane removed from each OPP sample. The fractionation factors calculated for the Rayleigh isotope model (α = 1.004) and the open system model (α = 1.024) (Fig. 10) were in close agreement with those measured in other systems (Leonte *et al*., 2017; Whiticar, 1999). By plotting the measured $\delta^{13}C\text{-}CH_4$ values against the fraction of methane oxidized from each sample, and comparing that to the open and closed system model results, it was possible to show that the closed system Rayleigh model provides the most accurate fit to the data.

Results

Vertical chemical profiles

High-resolution sampling of the MFW-MBW and MBW-SGW transition zones revealed dramatic methane and sulfate gradients associated with the shift in salinity (i.e., the halocline) at the shallow MFW-MBW transition zone (Fig. 11), but only a sulfate gradient at the MBW-SGW transition zone (Fig. 12). In the MFW, salinity ranged from 0.17 to 0.47 psu (with the exception of the 0.92 psu salinity value in 2015). The MFW was associated with high methane concentrations (ranging from 1,272 to 7,793 nM) that were ^{13}C-depleted (ranging from −58.1‰ to −67.5‰). By contrast, the MBW was characterized by oligohaline conditions (ranging from 1.81 to 1.88 psu) and lower

methane concentrations (ranging from 37 to 132 nM) that were ^{13}C-enriched (ranging from −47.8‰ to −55.5‰) relative to the MFW. The OPP-profile obtained in January 2015 was characterized by steeper chemical gradients and significantly higher source methane concentrations (7,187 ± 185 nM) with more depleted values (−67.1 ± 0.2‰) than the profile obtained in January 2016 which had lower concentrations (3,246 ± 238 nM) of less ^{13}C-depleted (−64.0 ± 1.3‰) source methane.

Sharp shifts in salinity (halocline) across the vertical chemical profile occurred within a 12 cm zone at approximately 4.2 m in 2015 (Fig. 11a) and within a 24 cm zone at approximately 4.6 m in 2016 (Fig. 11b), indicating that intermediate chemical properties can only be observed within a few cm transition zone. The higher resolution (2.5 cm) vertical profile obtained with the mini-OPP at the MFW-MBW transition zone provides a more detailed record of the intermediate chemical properties (Fig. 11c). Increasing salinity across the chemical gradient (from 0.74 to 1.84 psu) was associated with decreasing methane concentrations (from 1,419 to 42 nM) and increasing δ^{13}C-CH_4 values (from −65.2 to −52.0‰).

Across the MBW-SGW transition zone, an extreme shift in salinity and sulfate concentration was observed, but the methane concentrations and δ^{13}C-CH_4 values were relatively constant (Fig. 12a-b). Salinity values varied from oligohaline (as low as 1.79 psu) to mesohaline (as high as 14.38 psu) in the MBW and from 31.11 to 35.95 psu in the SGW. Methane concentrations ranged from 9 to 121 nM with δ^{13}C-CH_4 values −44.6‰ to −57.5‰ throughout the MBW-SGW profiles with no obvious trend that would imply methane consumption or production at the interface. Shifts in salinity across this halocline occurred within a 24 cm transition zone at approximately 19.80 m water depth in January 2015 (Fig. 12a) and within a 36 cm zone at approximately 20.0 m in January 2016 (Fig. 12b). The MFW-MBW transition was zone was also shallower and thinner in January 2015. The mini-OPP profiles provide a higher resolution record between the meteoric lens and the SGW (Fig. 12c), which should allow for a more detailed assessment of biogeochemical activity in the MBW-SGW transition zone.

Salinity varied from oligohaline (3.17 psu) to polyhaline (29.73 psu) across the 25 cm mini-OPP profile.

Conservative mixing model

A comparison of the conservative mixing model results to the measured values demonstrates the reduction in methane concentration and shift in $\delta^{13}C\text{-}CH_4$ values across the MFW-MBW transition zone is affected by a methane removal process that causes isotopic fractionation rather than simple physical mixing of MFW and SGW endmembers (Fig. 13a-b). According to the mass balance calculations, 98.9% (or ~6,560 nM) of the methane was consumed within the MFW-MBW transition zone in January 2015, and 98.8% (or ~3,100 nM) in the January 2016. Despite different transition zone depths and thicknesses for the two sampling events, the percent removal of methane within each was similar. The MBW-SGW transition zone showed no evidence of oxidation.

Kinetic isotope models

The comparison of two kinetic isotope models show that the closed-system Rayleigh model fits the data more accurately than the open system model, indicating that microbial methane oxidation within the transition zone is the primary process affecting the $\delta^{13}C\text{-}CH_4$ values in the (Fig. 14). Based on the Rayleigh model, microbial methane oxidation removed up to ~99.0% (or ~7,700 nM) of the methane source based on the January 2015 OPP profile, up to ~99.1% (or ~4,300 nM) according to the January 2016 OPP profile, which agrees well with the removal calculated by the mass balance approach based on the results of the conservative mixing model.

Discussion

High-resolution cm-scale sampling of undisturbed density interfaces within the flooded cave passages provides unprecedented details about the distribution of biogeochemically reactive species within a stratified coastal karst aquifer. In this case,

methane concentrations and $\delta^{13}C$ values along the salinity gradient from fresh to saline conditions were used to constrain processes related to methane dynamics in the KSE. Significant differences in the activity of methane-related biogeochemical processes were detected between the shallow and deeper haloclines. My analysis, based on mixing models and kinetic isotope models, identifies a hotspot of methane oxidation in the meteoric groundwater.

The measured chloride and sulfate concentrations are consistent with an origin from marine-derived saline groundwater. Stable sulfate to chloride ratios (0.052 ± 0.001) across all records are in agreement with those measured in the nearby coastal sea (Gondwe *et al*., 2010; Perry *et al*., 2002). This is consistent with a marine-origin for these ions within the study region, suggesting that physical mixing of fresh and marine-derived saline waters is the principal process influencing the distribution of chloride and sulfate. The sulfate concentrations measured here (ranging from 0.1 to 28.9 mM) were in agreement with previously reported values (see Chapter II).

Endmember salinity values within the profile were also in agreement with previous measurements based on manual water sampling of each water mass, suggesting that the records captured the full range of salinity in the flooded cave conduits. Average salinity values reported for the different water masses by a previous study (MFW = 0.3 psu, MBW = 1.8 psu, SGW = 32.9 psu; see Chapter II) were consistent with the endmember values measured at the pycnoclines. Salinity associated with the MFW-MBW transition ranged from 0.2-1.9 psu with a sharp shift from fresh to oligohaline conditions along the vertical depth profile. Depending on the sampling period, the salinity shift occurred within 12 to 24 cm, which is interpreted as the vertical spatial extent of the mixing zone (halocline). Salinity across the MBW-SGW transition ranged from 1.8-36.0 psu and was characterized by another sharp shift from oligohaline to saline values within a 24 to 36 cm zone. Combined analysis of the 12 cm resolution OPP and the 2.5 cm resolution mini-OPP profiles obtained at the MBW-SGW halocline in 2016 reveals a continuous transition from oligohaline (0.5-5.0 psu) to mesohaline (5.0-18.0 psu) conditions within 5.5 cm, then mesohaline to polyhaline (18.0-30.0 psu)

salinities within 15 cm, and eventually polyhaline to saline conditions (>30.0 psu) within another 15 cm. Consequently, this dataset demonstrates that high-resolution sampling of the haloclines makes it possible to obtain cm-scale chemical profiles that cover the full salinity spectrum of typical estuarine systems within the density stratified aquifer. This would not be possible by sampling manually along m-scale depth profiles in the water column. Nor would it be possible to obtain sonde based records with such precision because typical sampling rates and sensor responses are not sufficiently rapid.

Consistent with meromictic conditions for the KSE, the shallow and deep haloclines were present during both sampling events (Fig. 8b), but had distinct differences in their structure and position in the water column. In January 2015, the thickness of shallow and deep haloclines that were at least 12 cm less than in 2016, suggesting more stable conditions and less mixing in 2015. Also, the average approximate water depth of the MFW-MBW halocline was ~40 cm deeper and the MBW-SGW transition zone was ~14 cm deeper during 2016 than in 2015, implying that the groundwater level was higher during the second deployment. Temporal and spatial differences in precipitation patterns have direct impact on the dynamic hydrology of karst aquifers which directly affects mixing on recent (Kovacs *et al*., 2017) and paleo timescales (Curtis *et al*., 1996; van Hengstum *et al*., 2010). The total precipitation during a 15-day time period preceding the sampling event was 39 mm in 2015 and 253 mm in 2016 (see Chapter II). High precipitation prior to the 2016 sampling would have increased the hydraulic head of the groundwater, which would have had the effect of enhancing flow velocity and mixing (Beddows *et al*., 2002; Kovacs *et al*., 2017; Menning *et al*., 2015). Consequently, the thicker halocline is likely a result of enhanced mixing between the MFW and MBW resulting from enhanced hydrologic activity due to increased rainfall preceding the 2016 sampling event.

Profiles across the MFW-MBW and MBW-SGW transition zones show differences in methane concentrations and their $\delta^{13}C$ values. The MFW-MBW salinity gradient corresponds with an extreme shift from high to low methane concentrations, with a range between 7,793 nM (MFW) to 72 nM (MBW) in 2015 and between 4,325

nM (MFW) to 37 nM (MBW) in 2016. This reduction is associated with a significant enrichment of $\delta^{13}C\text{-}CH_4$ from −67.5‰ (MFW) to −47.8‰ (MBW) in 2015 and from −67.5‰ (MFW) to −55.3‰ (MBW) in 2016. The pattern of increasing $\delta^{13}C\text{-}CH_4$ values across the MFW-MBW interface is a methane oxidation effect by either anaerobic or aerobic methanotrophs (e.g., Barker and Fritz, 1981; Whiticar, 1999). With the exception of a single sample, sulfate concentrations and sulfate to chloride ratios do not support anaerobic oxidation of methane in the system (Fig. 11), but this analysis may not be sufficiently sensitive to detect changes of sulfate relative to methane, which has orders of magnitude lower concentrations. The presence of dissolved oxygen in the MBW during 2015 (Fig. 8d) indicate aerobic methane oxidation. The extremely low dissolved oxygen concentrations measured in the MBW in 2016 (<10 µM) was sufficient to fuel aerobic methane oxidation (Steinle *et al*., 2017). Methane source concentrations in the MFW were higher in 2015 relative to those in 2016, but showed no significant difference between source $\delta^{13}C$ values (as low as −67.51‰ in 2015 and −67.47‰ in 2016), indicating that methane accumulation was higher in 2015 than in 2016. Increased mixing, as discussed above, might also result in lower methane accumulation in the system.

In contrast to the shallow profiles, no evidence was found for methanotrophy across the deeper MBW-SGW transition zone. As a result, physical mixing between the MBW and SGW is most likely the key factor affecting the distribution of methane-related chemical properties across the deep interface. The MBW-SGW transition zone is associated with no significant trends in methane-related chemical constituents. Across this interface, low methane concentrations ranging from 50 nM to 121 nM in 2015 and 9 nM to 33 nM in 2016 correspond with ^{13}C-depleted methane varying from −50.4‰ to −57.5‰ in 2015, and from −44.6‰ to −50.6‰ in 2016.

Concentration and isotopic mixing models were utilized to delineate the effects of physical mixing from microbial production and consumption within the mixing system (Fig. 13). The concentration-based model (Fig. 13a) indicates that the observed reduction in methane concentrations at the MFW-MBW interface has been affected by

methane removal and not only physical mixing of low and high salinity water masses. The extreme shift in $\delta^{13}C\text{-}CH_4$ values for the isotopic mixing model (Fig. 13b) indicates the reduction of methane across this interface is coupled with isotopic fractionation that occurs during microbial methane oxidation. High-resolution sampling of the entire salinity gradient made it possible to demonstrate that methane oxidation is occurring strictly within the MFW-MBW transition zone, a hotspot of methanotrophy. This evidence suggests methanotrophic bacteria, which are a food source for filter feeding *Typhlatya* spp. shrimp in this habitat (see Chapter II), are concentrated at this interface.

A comparison of the kinetic isotope models demonstrates the measured methane concentrations and isotopic values are more similar to the Rayleigh isotope model than the Open System model (Fig. 14). Other environments, for instance the oceanic water column above methane seeps (Leonte *et al*., 2017), have also been shown to better fit the closed system model. The fractionation factors of methane oxidation calculated for the Rayleigh isotope model ($\alpha = 1.004$) and the open system model ($\alpha = 1.024$) (Fig. 14) are in close agreement with those measured in other systems (Leonte *et al*., 2017; Whiticar, 1999). These observations provide additional, robust evidence that the variability in measured methane isotopic ratios is primarily due to microbial oxidation, with minimal influence by mixing, and that methane originates from a generally uniform source. Methane production most likely takes place in the anoxic saturated soil/rock-matrix overlying the cave passages. Assuming the lowest measured $\delta^{13}C\text{-}CH_4$ value ($R_0 = -67.5‰$) is the source signature and using the isotope fractionation factor determined by the Rayleigh model, it was possible to estimate the corresponding initial source concentration (prior to oxidation) of each measured methane concentration value from the OPP profiles taken at the MFW-MBW interface. These calculations suggest the average source methane concentrations were ~8,700 nM in 2015 and ~5,200 nM in 2016. The difference in calculated initial methane concentrations between the two sampling periods provides further support higher methane accumulation in 2015 than during the second sampling period. Methanotrophy, however, removed similar fraction of methane originating from the MFW in both years. The Rayleigh model and the mass

balance calculations based on conservative mixing model are in agreement that up to 99% of available methane was oxidized in both sampling seasons, suggesting that microbial methane oxidation provides an efficient methane sink pathway in the shallow meteoric lens of this coastal aquifer.

In summary, high-resolution sampling of the density interfaces in a stratified coastal aquifer provided unprecedented chemical profiles along the salinity gradient in a karst subterranean estuary. The shallow halocline was associated with a hotspot of aerobic methane oxidation. Mixing models and the kinetic isotope models provided evidence for efficient methane removal (up to 99%) by microbial methane oxidation in both sampling seasons, contributing to the growing evidence that ecosystems residing in subterranean estuaries can function as a methane sink (Schutte *et al*., 2016). Differences in measured concentrations and $\delta^{13}C$ ratios of methane, and in calculated initial methane source concentrations indicate slightly more efficient methane accumulation in the flooded cave environment during the 2015 sampling period than in 2016. Coupled sulfate and salinity profiles from multiple periods suggest the position and structure of the halocline were likely affected by greater mixing in the January 2016, which was preceded by higher precipitation. Considering that methane provides carbon and energy for the food web in a variety of aquatic settings (Bastviken *et al*., 2003; He *et al*., 2015), including the current study site, Cenote Bang (see Chapter II), these findings contribute to the understanding of how anchialine ecosystems function within inland subterranean estuaries. Future studies will investigate effects of mixing on stratification and related chemical profiles as well as microbiological communities associated with the highly structured gradients in the water column.

CHAPTER IV
HYDROLOGIC CONTROLS OF METHANE DYNAMICS IN A KARST SUBTERRANEAN ESTUARY

Introduction

Subterranean estuaries host methane (CH_4) producing and consuming microbial communities that regulate the export of this greenhouse gas to the coastal ocean (Schutte *et al*., 2016) and provide a nutritive resource for complex food webs in the aquifer (see Chapter II). Within these estuaries, the interface between meteoric water and marine-derived groundwater is the primary biogeochemical reaction zone that alters the composition of submarine groundwater discharge (Moore, 1999) and, consequently, significantly impacts the chemical properties of coastal oceans (Kwon *et al*., 2014; Lee *et al*., 2010; Moore, 2010; Taniguchi *et al*., 2002). Globally, karst (solutionally eroded carbonate) platforms account for ~25% of all coastlines (Ford and Williams, 2013) and ~12% of all submarine groundwater discharge (Gonneea *et al*., 2014). Therefore, biogeochemical processes occurring within karst subterranean estuaries are likely to be a substantial component of coastal carbon budgets.

Carbonate platforms along coastlines contain density stratified water masses that infiltrate dissolutional karst features ranging in size from cm-scale crevices to meter-scale caves (Fig. 15). These conduits alter the hydrology of the region and enhance constituent transport to and from the coast (Beddows *et al*., 2007; Perry *et al*., 2002). The karst subterranean estuary (KSE) environment supports a rich and globally-dispersed anchialine (meaning “near the sea”) ecosystem with a fauna adapted to the subterranean conditions (Bishop *et al*., 2015; Iliffe and Kornicker, 2009; Stock *et al*., 1986). These oligotrophic habitats are characterized by exceptionally low particulate organic matter, suggesting anchialine ecosystems are more reliant on dissolved organic constituents originating from the overlying soil/rock-matrix as food sources (Pohlman, 2011).

In the Yucatan Peninsula (Mexico) (Fig. 15), methanotrophic bacteria are a component of a microbial loop that utilizes methane and other forms of dissolved organic matter (DOM) to fuel the anchialine food web (see Chapter II). In addition to the well-researched sharp density interface between meteoric water and marine-origin saline groundwater, a fresh (<0.5 psu) and virtually anoxic (<15 µM dissolved oxygen) water mass was identified that contained high concentrations of DOM (including methane) originating from decomposition of terrestrial vegetation within the overlying saturated carbonate rock-matrix. This anoxic, DOM-laden meteoric fresh water was underlain by meteoric brackish water containing sufficient oxygen (>30 µM) to aerobically decompose the energy and carbon rich DOM mixing across the pycnocline. These environmental parameters were observed in multiple time periods suggesting meromictic conditions in the habitat (see Chapter II).

Hydrological mechanisms, such as tidal pumping or precipitation-induced mixing (Beddows *et al*., 2007; Coutino *et al*., 2017; Kovacs *et al*., 2017; Martin *et al*., 2012), are likely to be key factors for mixing DOM into the meteoric brackish water where electron-accepting respiratory agents (e.g., oxygen and sulfate) are present in higher concentrations. Conduit flow facilitates organic matter transport within the subterranean estuary to and from the coastal ocean, which affects the quantity and quality of material expelled via submarine groundwater discharge (e.g., Gonneea *et al*., 2014). Conduit flow also conveys electron acceptors (e.g., oxygen and sulfate) to portions of the KSE where they would not otherwise be available. Dissolved oxygen entering the aquifer through point recharge of meteoric water (Ford and Williams, 2013) or tidal-pumping of coastal seawater (Beddows *et al*., 2007; Martin *et al*., 2012) is distributed in the KSE by the steady flow maintained in the conduits. In addition, the intrusion of marine water makes elevated sulfate concentrations available inland, farther from the coast (Socki *et al*., 2002). A better understanding of the processes that import and commingle energy-yielding compounds and the agents of cellular respiration (e.g., oxygen and sulfate) within the karst subterranean estuary will provide a better understanding of the balance between autochtonous (*in situ* produced) and allochtonous (introduced by transport)

bioavailable organic matter within the cave environment, an important question regarding the carbon cycling in anchialine ecosystems (Pohlman, 2011).

Hydrologic transport of organic matter (OM) and electron acceptors within the subterranean estuary is likely to impact the distribution and development of ecological habitats. Sulfate derived from saline groundwater becomes an important electron acceptor in eutrophic sub-habitats (Pohlman, 2011) where naturally or anthropogenically increased OM loading (e.g., through sinkholes) eventually inhibits oxic respiration due to limited oxygen availability. On the other hand, low levels of oxygen (hypoxic to oxic conditions) allow the fauna to inhabit the KSE in oligotrophic sub-habitats, where OM availability is limited (Pohlman, 2011). It is unlikely that oxic/hypoxic conditions could be maintained below an anoxic zone (Fig. 15d) in the saturated groundwater without conduit transport. Therefore, it is reasonable to assume that cave networks are likely to expand the magnitude of aerobic organic matter oxidation, that, in turn, supports an extensive anchialine ecosystem.

In addition to being a nutritive source for some ecosystems, methane accounts for ~20% of greenhouse gas radiative forcing (IPCC, 2014). Therefore, constraining the global sources and sinks for this important greenhouse gas is critical. Methanotrophy (microbial methane oxidation) is an important and efficient biogeochemical mechanism for controlling greenhouse gas fluxes in the environment and limiting methane emissions to the atmosphere. It is estimated that nearly 90% of the ~85 Tg CH_4 yr^{-1} produced globally in marine and freshwater systems is consumed by anaerobic and aerobic methanotrophs before reaching the atmosphere (Reeburgh, 2007). These pathways limit natural global methane contributions to the atmosphere to ~2-10% from natural lakes (Bastviken *et al*., 2004) and to only ~2% from oceans (Reeburgh, 2007). In coastal settings, anaerobic methanotrophy was found to be a critical mechanism controlling the quantity of methane expelled to the coastal ocean from a barrier island's subterranean estuary (Schutte *et al*., 2016). Methane in coastal sea water is often associated with submarine groundwater discharge and has been used as a tracer for groundwater in numerous studies (Cable *et al*., 1996; Kim and Hwang, 2002; Schutte *et al*., 2016).

Relatively high methane concentrations (121 nM, on average) have been reported from the Caribbean Sea near the coast of the Yucatan Peninsula (see Chapter II) where discharging groundwater is a major contributor to coastal seawater quality (Gonneea *et al*., 2014; Young *et al*., 2008). Although, constituent transport by submarine groundwater discharge along the world's coastlines has been increasingly recognized (Kwon *et al*., 2014; Moore, 2010; Moore *et al*., 2008), its role in regional and/or global scale methane budgets is poorly understood.

In the present study, chemical and hydrological records were used from a KSE of the Yucatan Peninsula, Mexico, to understand what controls methane availability within the aquifer. Sensor-based data loggers were used to monitor weather aboveground (e.g., precipitation, barometric pressure and air temperature) and hydrologic parameters (e.g., water level, flow velocity and water temperature) at varying depths in the KSE. OsmoSamplers were co-deployed with the data loggers to obtain time-series measurements of chloride, sulfate, and methane (including the $\delta^{13}C$ of methane) from the methane-rich shallow meteoric waters and the relatively methane-depleted deep meteoric lens of the stratified groundwater. Using these high-resolution temporal records, I tested the hypothesis that methane inputs and consumption within the subterranean estuary are affected by the groundwater hydrology, which is controlled by tidal pumping and precipitation patterns. The findings are synthesized into a landscape model that includes the hydrological-controls of biogeochemical processes and the methane sink potential of the system, contributing to a better understanding of the fundamental ecosystem function of terrestrially influenced subterranean estuaries in coastal karst landscapes.

Study Area

The study site is located in the Caribbean coast of the Yucatan Peninsula, in the state of Quintana Roo (Mexico) (Fig. 15), where the highly permeable limestone platform's topography is characterized by limestone platform is characterized by low-lying, relatively flat topography and lack of surface flowing streams and rivers (Beddows *et al*., 2007; Perry *et al*., 2002). The area is subject to rapid development and

urbanization, primarily due to tourism, which threatens offshore coral reefs, natural surface vegetation at the coast (e.g., mangroves and sea grass) and inland (e.g., dry tropical forest), as well as the groundwater resources and groundwater-dependent habitats (Bauer-Gottwein *et al*., 2011). Seawater intrusion into the KSE is primarily controlled by hydrological processes related to eustatic sea level and meteoric fresh water recharge. In this region, the Holbox Fracture Zone and Xel Ha Zone (Perry *et al*., 2002) contains more than 1,000 km of mapped cave conduits (Kambesis and Coke, 2013) that provide direct access to the inland portion of the subterranean estuary over an area (~1,100 km^2) comparable to large surface estuaries. The research site is located in a region of seasonally dry tropical climate with dry (typically from December to April/May) and wet (from May to November) seasons (Curtis *et al*., 1996; Kottek *et al*., 2006). The cooler dry season is characterized by less than 60 mm monthly rainfall that provides less than 4% of the annual precipitation per month (Kottek *et al*., 2006; Peel *et al*., 2007), delivering a total of approximately 250 mm throughout this season. The remainder of the approximately 1500 mm mean annual precipitation falls during the rainy season, with maximum rainfall occurring during the months of June and September (Curtis *et al*., 1996). Because there is no surface runoff, all precipitation that does not evaporate or get transpired by plants recharges the aquifer (Gondwe *et al*., 2010). Akin to the streams and tributaries that define the watershed for a river basin, upstream conduits that feed large cave passages (accumulating runoff) define the areal extent of the subterranean drainage basin.

The sampling stations within the cave environment were accessed through a flooded sinkhole (locally referred to as Cenote Bang; 20° 12.62' N 87° 30.06' W) located beneath a dry tropical forest 8 km from the coastline in Quintana Roo, near Tulum (see Chapter II). A meteoric fresh water (MFW; ~0.2 psu) lens extends to ~4 m below the groundwater table and largely resides within the rock matrix. A meteoric brackish water layer (MBW; ~1.8 psu) that resides between the MFW and deeper saline groundwater (SGW; >30.0 psu) occupies the largest fraction of the cave passages (Fig. 15d) and therefore conducts the majority of the flowing conduit groundwater. The MFW and

MBW are separated by a sharp (12-24 cm thick) salinity interface (halocline) at about 4 m below the groundwater table. The MBW extends to approximately 20 m water depth where another halocline (24-36 cm thick) separates this water mass from the SGW.

Methods

Environmental parameters

The arrangement of the monitoring devices on the surface and in the cave environment is shown on Fig. 16. A meteorological station located ~9 km from the study site measured precipitation, barometric pressure and air temperature between 01/18/2015 and 01/22/2016. The station was placed on the rooftop at a secure site (Speleotech facility; 20° 12.396' N 87° 28.079' W) about 15 m above ground level and well above the forest canopy in the town of Tulum, Quintana Roo. Precipitation was measured with an ONSET RG-3 rain gauge (calibration accuracy of ± 1.0%, up to 2 cm h^{-1}; 0.2 mm resolution; time accuracy ± 1 min per month) and is presented as daily total precipitation (mm d^{-1}). An ONSET U20 data logger was co-deployed with the rain gauge to monitor barometric pressure (<0.02 kPa resolution and a ± 0.3% FS or 0.62 kPa accuracy as the maximum error) and air temperature (0.1 °C resolution, ± 0.44 °C accuracy) at 15-min time intervals.

Two sets of data loggers were deployed within the flooded cave environment at different depths below the water table, one at 17 m (MBW) and the other at 22 m (SGW) (Fig. 16). Each set of loggers monitored groundwater flow velocity, water level and water temperature. Loggers were placed in the maximum expected flow regime within the MBW and SGW. Current velocity and the direction (bearing) were measured with a TCM-1 (Lowell Instruments LLC) tilt-current meter (TCM; ± 2 cm s^{-1} + 3% of reading accuracy and 0.1 cm s^{-1} resolution; bearing ± 5° accuracy for speed >5 cm s^{-1} with a 0.1° resolution) with a 1-min logging interval (Lowell *et al*., 2015). An ONSET U20 data logger was used to monitor water level (± 0.21 cm resolution with an error less than ± 1.0 cm) at 15-min sampling intervals. Water level data are reported as the departure from the mean value, in meters. Barometric pressure measured at the meteorological

station was used to correct the water level measurements for atmospheric pressure effects.

Chemical record

Continuous water samples for analysis of methane concentration and $\delta^{13}C$, and the concentrations of sulfate and chloride were obtained with "OsmoSamplers" (OS). These water sampling devices include a sample collection coil attached to an osmotic pump and are capable of collecting continuous water chemistry records (Jannasch, 1985). OsmoSamplers have been successfully used to track temporal changes in methane concentrations in a variety of settings, including gas hydrate related hydrocarbon seeps in the seafloor (Lapham *et al*., 2008; Tryon and Brown, 2004; Tryon *et al*., 1999). In this study, each OS has eight 2ML1 semipermeable membranes (Durect Co.) that separate a saturated salt solution from deionized (DI) water. The osmotic potential between the high and low ionic solution compartments draws water from the DI water reservoir across the membranes (Jannasch, 1985). Water lost from the reservoir is replaced by degassed DI water from within a ~300 m coil of 1/16" OD gas-impermeable copper tubing, which is balanced by drawing water from the environment through a 0.1 µm hydrophilic filter at the other end of the tubing coil. Pumping rates determined prior to deployment for the deep and shallow OSs were 0.80 ml d^{-1} and 1.0 ml d^{-1}, respectively.

OsmoSamplers were deployed following protocols developed by Lapham *et al*. (2008) with modifications for scuba diver deployment. The pump and the sample coil were packed in a plastic laundry basket in a compact and streamlined manner allowing the diver to manually transport and deploy the device. The sample inlet of the shallow-OS was placed in the MFW at 3.5 m water depth, above the shallow halocline, near the cave ceiling (MFW-OS on Fig. 16). The inlet port of the deep-OS was placed at 7.5 m, below the shallow halocline, in the meteoric brackish water layer (MBW-OS on Fig. 16). OsmoSamplers were co-deployed in two subsequent time periods to cover both seasons (first deployment was from 1/17 to 6/14/2015; second deployment was from 6/19/2015 to 1/20/2016). Within two hours of recovery, the copper tubing was removed from the

osmotic pump and sealed on both ends with 1/16" capped compression fittings. The coils were stored at ~7 °C in the field, transported to the U.S. and stored on 4 °C until they were subsampled in the laboratory. Subsampling included cutting the coils into 4.5 m sections that were later split into a 4 m long section, containing water for analysis of methane concentration and $\delta^{13}C$, and a 0.5 m long section with water for anion (chloride and sulfate) concentration analysis. Approximately 0.5 ml of water was recovered per meter tubing.

Prior to the analysis of methane concentrations, sample water within each of the 4 m long subsections was expelled into a 10 ml syringe using a benchtop tube roller and a gas tight connection between the tubing and the syringe. The syringe and the connection were flushed with methane-free zero-air or Helium (He) before receiving the sample. As each section was rolled, the pressure increased inside the tubing until the crimped end of tubing burst, thereby allowing the water to accumulate in the syringe. The sample volume was determined by weighing the syringe before and after sample extraction using an analytical balance, assuming the mass of 1 ml of ion-free water is 1 gram. Each sample was mass corrected for its measured salinity. Following sample extraction, 3 ml of He was added to the sample as headspace while maintaining 1 atm pressure inside the syringe. The syringes were shaken for 3 minutes to allow methane from solution to equilibrate with headspace, which was analyzed within four hours of extraction. 34 of the 192 samples extracted were prepared for coupled methane concentration and $\delta^{13}C\text{-}CH_4$ analysis. These subsamples were extracted as described above with the modification that two 5 ml syringes were connected with stop-cocks. The syringe for $\delta^{13}C\text{-}CH_4$ determination received a ~1.5 ml subsample and 2 ml, while syringe for methane concentration analysis received an ~0.5 ml subsample and 3 ml He headspace gas.

The water sample within each 0.5 m long section was directly expelled into 1.5 ml plastic vials for measuring sulfate and chloride concentrations. Near the end of the 300 m long coil attached to the deep osmotic pump, the salinities changed from brackish values (2-3 psu) to fresh (0 psu), indicating the end of the sample record. Pumping rates

were re-calculated based on the measured length of the sample, which was converted to volume based on tubing dimensions, and the time of deployment. This approach was not possible to repeat with the shallow-OS because the tubing overfilled. The deep-OS had an actual pumping rate of 0.76 ml d^{-1}, which compares to the laboratory-measured pumping rate of 0.80 ml d^{-1}. The shallow-OS had a laboratory pumping rate of 1.0 ml d^{-1}. Based on these basic pumping rates and the dimensions of the tubing (see above), each 4.5 m section represents 2.2 days for the shallow-OS and 2.5 days for the deep-OS. Consequently, it was possible to ascribe a time interval to each section of the coil.

Geochemical analyses

Analyses were performed at the Woods Hole Oceanographic Institution (WHOI) and U.S. Geological Survey (USGS) in Woods Hole MA, USA. Methane concentrations were determined by injecting 3 ml headspace directly from the syringe into a Shimadzu 14-A gas chromatograph (GC) equipped with a flame ionization detector (FID). The gases were isothermally (50 °C) separated with a Poraplot-Q stainless steel column (8 ft x 1/8" OD) packed with 60/80 mesh and quantified against certified gas standards with a relative standard deviation of 2.8% or less. Headspace concentrations were converted to dissolved concentrations following established methods (Magen *et al*., 2014).

The $\delta^{13}C$ signature of methane in the headspace of the syringe was determined using a Thermo-Finnigan DELTA^{Plus} XL isotope ratio mass spectrometer (IRMS) coupled to an Agilent 6890 Gas Chromatograph (GC) via a Finnigan GC Combustion III interface. The gas sample was introduced directly from the 2 ml headspace in the syringe through a gas sampling valve into a 1 ml min^{-1} He carrier gas stream. Methane and other condensable gases were trapped on fused silica capillary packed with 80/100 mesh Poraplot-Q immersed in liquid nitrogen following an established protocol (Popp *et al*., 1995) with modifications. The gases were thermally desorbed from the column at 150 °C and separated on a 30 m, 0.32 mm ID Poraplot-Q column at −40 °C prior to being oxidized to CO_2 and analyzed by IRMS. The $^{13}C/^{12}C$ ratios of methane are expressed in the standard δ-notation using tank CO_2 referenced to the Vienna Pee Dee Belemnite

(VPDB) standard. The standard deviation (1 σ) of a 1% CH_4 standard analyzed at least every 8 samples was 0.3‰.

Sulfate and chloride concentrations were determined using a Metrohm 881 Compact Plus ion chromatograph (IC) equipped with a Metrosep A Supp 5-250 anion column. Samples from the MFW and MBW were diluted by factors of 31 and 61 respectively to maintain the chloride peak within the limit of the conductivity detector. Peak areas for sulfate and chloride were quantified against equivalently diluted International Association for the Physical Sciences of the Oceans (IAPSO) standard seawater analyzed at the beginning of the run and after every fifth sample. Chloride concentrations (mM) were converted to mg l^{-1} and multiplied by 0.0018066 to determine salinity (psu). The analytical error for dissolved constituents was ± 3.5% of the IAPSO standard sulfate and chloride values.

Statistical analysis

Correlation analysis was performed to establish fundamental hydrologic mechanisms in the system (e.g., Legates and McCabe, 1999) using monthly mean values of meteorological parameters (i.e., precipitation and air temperature) and hydrological parameters (i.e., water level, flow velocity in MBW, salinity from MFW and MBW). Mean monthly values were used to account for phase lags among the measured parameters (Gondwe *et al*., 2010; Kovacs *et al*., 2017). This approach made it possible to incorporate salinity data from the chemical records, which are subject to uncertainties at shorter time intervals due to uncertainties in the OS pumping rates. Pearson Product-Moment Correlation analysis was performed on the year-long record and the dry and wet season records independently, which made it possible to examine seasonal differences in hydrological processes.

Wavelet analysis of precipitation, water level and water velocity was conducted to calculate the phase lag between hydrologic parameters and to confirm some of the fundamental hydrologic processes revealed by correlation analysis (Grinsted *et al*., 2004). Cross wavelet transforms of two time-series identifies common power in time-

frequency space, allowing for a mechanistic link between processes (Grinsted *et al*., 2004) and has been useful for identifying hydrologic mixing mechanisms and their temporal extent in the unconfined Yucatan aquifer (Coutino *et al*., 2017; Kovacs *et al*., 2017). Coherence between continuous wavelet transforms are more informative than standard lagged correlation analyses because they account for dynamic variations in time-frequency space. For example, the correlation between precipitation and water level may vary in terms of magnitude and phase as a function of the magnitude of the precipitation event.

Results

Meteorological records

Variations in precipitation, barometric pressure and air temperature recorded on the surface were consistent with weather patterns associated with the regional climate. Water level and flow velocity varied on diurnal and semidiurnal scales (see Supplemental Material). Seasonal and sub-seasonal variations, the focus of this study, were observed in the precipitation and air temperature records (Fig. 17). Total annual precipitation measured at the meteorological station was 1,387 mm (dry season 158 mm and wet season 1,228 mm). Based on monthly mean values from this record, for the period of this study, June to November are defined as the wet period and December to May as the dry period (monthly precipitation <60 mm and <4% of annual rainfall in subsequent months) (Kottek *et al*., 2006; Peel *et al*., 2007). Although based on this categorization July was functionally a dry month (with 20 mm total precipitation), for continuity of the record July is included as part of the wet season. Annual mean air temperature was 27.8 °C with January being the coldest month (23.7 °C in 2015 and 24.3 °C in 2016), and July (30.7 °C) and August (30.4 °C) being the two warmest months. Barometric pressure was consistent with regional climate (data not shown).

Hydrologic records

In the meteoric brackish water (MBW), water temperature was relatively constant, with an annual mean of 25.60 ± 0.04 °C. Changes in water level and flow velocity occurred on subtidal and tidal (see Supplemental Material) to seasonal scales (Fig. 17). Water level, presented as departure from annual mean value, was lowest during the months of February and March (Fig. 17) when it was ~14 cm below the annual average. The groundwater table reached highest levels in October and November when it showed a positive departure (>26 cm) from the annual mean. Flow direction in the MBW was always towards the coastline with velocities averaging 9.0 ± 0.0 cm s^{-1} during the year-long deployment period, with lower and more stable velocity in the dry season (7.9 ± 0.0 cm s^{-1}) than in the rainy season (10.20 ± 0.01 cm s^{-1}). Episodic events with high flow velocity (up to 32.6 cm s^{-1}) were only observed in the wet period (Fig. 17).

The saline groundwater (SGW) was characterized by constant, slightly warmer temperatures than the MBW, with an annual mean of 25.77 ± 0.01 °C, and a net flow direction opposite to the coastward flowing MBW. Measured flow velocity in the SGW was, on average, 0.4 ± 0.0 cm s^{-1} during the year-long deployment period. These flow velocity values are below the reported detection limit of the tilt-current meter (Lowell *et al*., 2015), but are consistent with minimal groundwater flow towards inland in the SGW (Beddows *et al*., 2007).

Chemical records

Temporal records of methane concentrations, $\delta^{13}C\text{-}CH_4$ values and salinity from the shallow (MFW) and deeper (MBW) meteoric lens were obtained simultaneously (Fig. 18). The shallow-OsmoSamplers deployed at 3.5 m in the MFW provided a 341-day chemical record (2/12/2015 to 6/14/2015 and 7/13/2015 to 1/19/2016) that includes a 29-day gap caused by overfilling the coils during the second deployment (see Methods for details). Mean salinity during the year-long deployment was 0.26 ± 0.01 psu in the MFW. Here, high methane concentrations (5,209 ± 102 nM) were observed year around

with higher average value in the dry season (5,949 ± 132 nM) than in the wet season (4,361 ± 89 nM) (Table 2). On five occasions during the dry season methane concentrations exceeded 8,000 nM with a single event being greater than 13,500 nM (Fig. 18). By contrast, the highest measured methane concentration in the wet season was 6,073 nM. Methane in the MFW was characterized by depleted $\delta^{13}C$ values during the dry season (−65.2 ± 0.5‰) and the wet season (−65.8 ± 0.7‰) (Table 2).

The deep-OsmoSamplers deployed at 7.5 m water depth in the MBW provided a year-long salinity record (1/19/2015 to 1/19/2016) with a 5-day gap between the end of the first deployment (6/14/2015) and the start of the second deployment (6/19/2015). Moreover, the first deployment resulted in a 151-day methane record (1/19/2015 to 6/14/2015) that primarily included dry months and the beginning of the wet season (Fig. 18). The MBW was characterized by higher salinity (1.94 ± 0.02 psu, on average) than observed in the MFW during the year-long deployment. The MBW chemical record revealed generally low methane concentrations with an average baseline value of 213 ± 31 nM. This mean value does not include the five, extremely positive, methane concentration anomalies (Fig. 18) that were associated with rapid increase followed by a rapid return to baseline concentrations. Four of these methane peaks, reaching values between 1,157 to 2,892 nM, were recorded during the dry season and they coincided with low-intensity rain events. The last methane peak in the record, which was also the highest methane concentration measured in this water regime (6,214 nM), was recorded during the wet season at the very end of the deployment. This event coincided with a sudden decrease in methane concentrations to 3,724 nM (a value below the seasonal average value) in the MFW and a high-intensity rainfall that delivered 154 mm of precipitation on June 13th 2015. The mean stable carbon isotopic value of methane was, on average, −38.1 ± 1.7‰ in the MBW.

Correlation and wavelet analyses

Correlation analysis, performed with monthly mean values of hydrologic parameters (Table 3), illustrate differences in precipitation leading hydrologic processes

between the shallow and deeper strata of the meteoric lens (i.e., the MFW and the MBW). Wavelet analysis between precipitation and water level showed highest coherence at periods of approximately 40-75 h (2-3 d), with a phase lag (of precipitation leading water level) averaging ~18 h following high-intensity rainfall events (see Supplemental Material). Similar analysis between precipitation and flow velocity resulted in highest coherence at periods of approximately 30-100 h (1-4 d), with a phase lag (of precipitation leading water velocity) averaging ~20 h (Fig. 19). The high-precipitation period during October and November leads to high coherence on the ~512 h (21 d) timescale, likely due to increased frequency of precipitation events. Wavelet coherence between water level and water velocity showed elevated coherence on the tidal timescale of ~12.42 h, which demonstrates a lag of ~5 h between water level and velocity (see Supplemental Material). Elevated coherence between water level and velocity was also observed during episodic rainfall events in the wet season when the high-precipitation period (between October and November) led to high coherence at ~48-168 h (2-7 d) timescales, as well as longer-term coherence on the ~512 h (21 d) timescale, again likely due to the frequency of precipitation events.

Discussion

Seasonal methane dynamics

An unprecedented 12-month, 2.5-day resolution record of methane concentrations from the shallow meteoric fresh water (MFW) portion of a flooded cave conduit within the Yucatan Peninsula carbonate platform reveals that methane, hypothesized to be produced during the microbial decomposition of the tropical forest vegetation, is present in high concentrations (5,209 ± 102 nM) throughout the year. A contrast between the high concentrations of ^{13}C-depleted methane (−65.2 ± 0.5‰) in the MFW and lower concentrations (216 ± 34 nM) of relatively ^{13}C-enriched methane (−38.8 ± 1.8‰) during the dry season in the deeper MBW demonstrates methane consumption (Whiticar, 1999) – a process suggested to provide nutritive carbon for the anchialine food web in this region – is a persistent process, and therefore food supply, in

this ecosystem. Variation in methane concentrations within the MFW and MBW reveals temporal dynamics in methane availability and consumption that are likely affected by groundwater mixing and transport. It is hypothesized that these mixing scenarios are linked to the hydrology and meteorology of the platform. A comparison and analysis of methane dynamics within this KSE to coincidental hydrological records of groundwater salinity, flow velocity, and water level, and meteorological records of precipitation and air temperature are used here to develop a landscape-level hydro-biogeochemical model and calculate a first-order estimate of the magnitude of the methane sink for this highly-stratified groundwater system.

Higher source methane concentration in the dry season (5,949 ± 132 nM) in comparison to the wet season (4,361 ± 89 nM) reveal seasonal dynamics for methane accumulation within the cave accessible portion of the shallow meteoric lens. Correlation coefficients show negative relationship between accumulated methane concentrations in the MFW and environmental parameters of precipitation ($r = -0.73$), water level ($r = -0.73$) and flow velocity ($r = -0.60$) suggests the decrease in methane source concentrations during the dry to wet season transition are associated with increased precipitation, which also has the effect of increasing oxygen inputs (Ford and Williams, 2013), increasing the hydraulic head and accelerating the mass transport of water toward the coast (Table 3) (e.g., Beddows *et al*., 2002; Kovacs *et al*., 2017; Menning *et al*., 2015). Therefore, it is concluded that periods of high precipitation driven hydrological events limit methane concentrations in the MFW, while low precipitation periods promote methane accumulation in the shallow meteoric lens.

The methane record from the MBW was characterized by generally low concentrations (213 ± 31 nM) with five positive concentration anomalies (Fig. 18). The greatest methane concentration was recorded during a 2.5-day period and was associated with the highest daily rainfall in the wet season. This event also coincided with the lowest methane concentration (3,724 nM) measured in the shallow meteoric lens during the first deployment period. The other four episodic methane peaks in the MBW correspond with four low-intensity (2-17 mm d^{-1}) precipitation events in the dry season,

suggesting that local rainfall is a plausible explanation for rapid methane input from the methane-charged shallow meteoric lens to the deeper portions of the groundwater. Precipitation events that were not associated with methane peaks in the deeper meteoric lens are likely to be a result of not sufficient intensity to cause mixing between the MFW and MBW. Methane concentrations returned to baseline values in less than 2.5 days after its injection into the deeper meteoric lens (Fig. 18). Removal by groundwater transport and/or biological consumption by methanotrophy are reasonable explanations for the rapid removal. Given the enriched $\delta^{13}C\text{-}CH_4$ values and other evidence for aerobic methane oxidation in the MBW (see Chapter II), the majority of methane transported into this water regime during discrete precipitation events is likely to be eventually consumed before the water discharges into the coastal sea. Evidence that mixing and oxidation of methane within the caves of the KSE is controlled by the coastal aquifer's dynamic hydrology contributes to the increasing lines of evidence that the quantity of methane expelled by submarine groundwater discharge along coastlines (Cable *et al*., 1996; Kim and Hwang, 2002) is regulated within the subterranean estuary (Schutte *et al*., 2016).

Relationships between water chemistry, hydrology and meteorology

Relationships between the meteorology, hydrology and water chemistry are evident from the correlation (Table 3) and wavelet analyses (Fig. 19; see Supplemental Material). Water level leading flow velocity, as well as their positive response to tidal change and precipitation are well-known characteristics of unconfined carbonate aquifers (Beddows *et al*., 2002; Kovacs *et al*., 2017; Menning *et al*., 2015). The expected positive relationship between water level and flow velocity is apparent on tidal and seasonal timescales (Table 3; see Supplemental Material). Both of these hydrologic parameters show a positive response to precipitation (Table 3; Fig. 17) with an 18-20 h phase lag (Fig. 19; see Supplemental Material).

For salinity, opposite responses within the shallow-fresh (MFW) and deeper-brackish (MBW) meteoric lenses were observed following precipitation events and

consequent hydrological processes. In the MFW, salinity correlated negatively (i.e., decreased) with increasing water level and flow velocity. By separating the wet and dry seasons, the strength of these correlations increases and clear negative relationships between precipitation and salinity become apparent for both seasons (Table 3). These results suggest precipitation lowers the salinity in the shallow meteoric water regime by dilution. Air temperature was the only parameter to be positively correlated with MFW salinity. This relationship is consistent with increasing salinity in the shallow meteoric lens due to freshwater loss by evapotranspiration during the warmest months of the year (Gondwe *et al*., 2010).

In contrast to the MFW, salinity in MBW (the deeper portion of the meteoric lens), increased in response to rain-induced hydrological changes (Table 3). Seasonal analysis reveals that the correlations between MBW-salinity and the parameters of water level and flow velocity are much stronger in the wet season (Table 3). This is expected given the stable head and flow velocity conditions in the dry season (Fig. 17). These findings support that lagged increase of flow velocity (in response to regionally increased precipitation) will promote mixing between the MBW and the underlying saline groundwater (the SGW). Mixing in the MBW is a result of greater shear at the halocline between the dynamic meteoric lens, with increased flow, and the more stagnant saline groundwater (Coutino *et al*., 2017; Kovacs *et al*., 2017). These mechanisms likely persisted on Holocene timescales (van Hengstum *et al*., 2010). In contrast, the MFW is mostly confined to the permeable carbonate rock matrix with limited exposure to conduit flow (Fig. 15; Fig. 16), which provides a reasonable explanation for the lack of positive relationship between salinity and water level or flow velocity in the shallow portion of the meteoric lens following increased flow-velocity periods. As a result, the MFW is more susceptible to direct precipitation effects, while the deeper-MBW is more susceptible to mixing with the underlying saline groundwater.

Wavelet coherence between rainfall and water velocity (Fig. 19) indicates the effects of precipitation-induced flow velocity lasts from 1-4 days during small rainfall events and up to 21 days during high-frequency and -intensity precipitation events. In

light of the positive correlation between MBW salinity and flow velocity, it becomes apparent that flow-driven mixing in the meteoric lens has a significant and lasting effect depending on the magnitude of the rainfall. These mixing scenarios will likely influence organic matter transport in the environment. Moreover, positive changes in salinity within the MBW, accessible portion of the meteoric lens (Fig. 15), will likely impact human populations, who have been historically dependent on this groundwater resource within the region, in their ability to utilize the water source (Curtis *et al*., 1996; Van Hengstum *et al*., 2010).

Mixing mechanisms affecting salinity and organic matter transport

Hydrologically driven transport and mixing influence salinity, OM distribution and chemical gradients in the unconfined coastal aquifer. Here, I discuss the major mixing mechanisms affecting the transport of chemical constituents, including methane, across varying spatial and temporal scales (Table 4). Tidal fluctuation and evapotranspiration are potential drivers of regional, small-scale mixing that will commingle constituents in the density stratified groundwater. Tidal oscillation in water level leading flow velocity (with a phase lag of ~5 h) is present at the study site, which is 8 km from the coastline (Fig. 19; see Supplemental Material). Such a tidal effect has been suggested as one driver of small-scale mixing mechanisms (Kovacs *et al*., 2017) and is likely to increase in magnitude with proximity to the coast. Intense evapotranspiration, typical during the late dry and early wet season (Gondwe *et al*., 2010), alters the chemical gradient by increasing salinity in the shallow meteoric lens. The positive change in salinity also lowers the buoyancy of the uppermost water layer resulting in a physical effect that potentially promotes mixing. The relative importance of small-scale mixing processes is likely to be even greater for dissolved constituent distribution and chemical exchange at interfaces, including haloclines in the water column of the cave conduit and transitional zones between the permeable limestone and the cave environment. Therefore, it is concluded that tide- and evapotranspiration-induced small-scale mixing mechanisms are likely the dominant physical processes that

facilitate the activity of biogeochemical hotspots (see Chapter III) at the sharp interface between MFW and MBW by mixing methane and other dissolved organics from the MFW with oxygen from the MBW during periods of stable stratification.

Recharge-induced mixing effects vary in their intensity depending on the volume of rain during individual precipitation events and their frequency. As argued above, episodic methane transport from shallow to deeper meteoric waters is likely facilitated by rainfall events, which is consistent with a vertical mixing-effect and resulting downward OM-transport in the meteoric lens (Fig. 18). This observation is further supported by the direct salinity-lowering effects of rainfall in the shallow-MFW (Table 3). In contrast, precipitation leading changes in salinity within the deeper-MBW show differences between the seasons. Low precipitation during the dry season is likely not sufficient in intensity to affect the salinity of the deeper water mass. High-intensity rainfall events, on the other hand, significantly increase the salinity in the MBW during the rainy period (e.g., high-frequency, multiple-day rainfall and/or storms) (Table 3), which, as discussed above, suggests great mixing between the MBW and SGW during high-intensity rain events (Coutino *et al*., 2017; Kovacs *et al*., 2017).

Landscape-level hydro-biogeochemical model

Variation in hydrology, methane dynamics and mixing processes during the year-long sampling period identify seasonal and sub-seasonal trends in hydro-biogeochemical processes that control organic matter transport and methane consumption within the subterranean estuary (Table 4; Fig. 20). Dry season is characterized by low-intensity precipitation. Following the wet season, water level and velocity subside. Gradually increasing salinity in the MFW suggests evapotranspiration is greater than freshwater recharge into the MFW, despite the relatively low evapotranspiration rates during this time of the year (Gondwe *et al*., 2010).

Precipitation low in frequency and intensity limits oxygen inputs from recharging meteoric water and subsequently promotes the stratification between anoxic and hypoxic water masses. Small-scale mixing processes driven by tides, evaporation and occasional

precipitation prevails during the dry season, which intensifies stratification of the water column and limits material exchange between water masses. These conditions are favorable for methane accumulation in the MFW. Rates of methanotrophy and other DOM-assimilating biogeochemical process that provide carbon and energy for the food web are expected to be minimal and limited to diffusive exchange across the MFW-MBW interface during this hydrologically quiescent period.

At the onset of the rainy season, precipitation of increasing frequency and intensity will raise the water level and groundwater flow velocity (Table 3), which enhances mixing between the anoxic methane- and DOM-laden MFW and the hypoxic MBW. These precipitation-driven mixing events will dominate the transport mechanisms during the rainy period. Lower salinity in shallow-MFW and elevated salinity in the deep-MBW are a measured response to increased recharge and flow-induced mixing. Decreasing salinity in the shallow meteoric lens suggests that freshwater recharge from high-intensity precipitation events overwhelms the salinity-increasing evapotranspiration-effects on chemical gradients. By contrast, increasing salinity in the deeper-MBW is a result of greater flow-induced mixing with salinity coming from mixing between the MBW and SGW (Coutino *et al*., 2017; Kovacs *et al*., 2017). Pulsed injections of air-equilibrated meteoric water (Ford and Williams, 2013) and vigorous mixing scenarios are more prevalent during the wet season, suggesting greater mixing between the shallow (MFW) and deep (MBW) meteoric lens. These hydrological events periodically mix oxygen with methane and other dissolved organic compounds that originated in the saturated rock-matrix and supports aerobic oxidation of methane.

Magnitude of the methane sink within the subterranean estuary

Simultaneous records of salinity, source and residual methane concentrations are used for a mixing model to determine the quantity of methane consumed in the system. These calculations are integrated with a hydrological model to provide a first-order estimate of methane consumption rates in the inland subterranean estuary. This

integrated model is applied for a study period within the dry season (2/12/2015 to 5/31/2015) that contained simultaneous records of methane concentration and salinity from both the MFW and MBW.

The rate of methane consumption within the drainage basin of the subterranean estuary investigated is expressed as,

$$MCR_{area} = \frac{MCR_{int}}{A_{SDB}} \tag{4.1}$$

where MCR_{area} is the methane consumption rate on an areal basis (mg CH_4 m^{-2} yr^{-1}), MCR_{int} is the integrated methane consumption rate (mg CH_4 yr^{-1}), and A_{SBD} is the effective area (m^2) of the subterranean drainage basin.

Estimation of the area of the subterranean drainage (A_{SDB}) required to supply the measured volume of water flowing through the main passage of the cave during the studied time period is calculated as,

$$A_{SDB} = \frac{Q_{MBW}}{NIR} \tag{4.2}$$

where Q_{MBW} is the mean volumetric flow (m^3 s^{-1}) in the MBW during the study period, and NIR is the net infiltration rate (m s^{-1}) calculated as the difference between contributions from precipitation and losses by evapotranspiration and surface runoff. Since surface runoff in Quintana Roo, the location of the study site, is negligible (Beddows *et al*., 2007; Gondwe *et al*., 2010; Perry *et al*., 2002), NIR is expressed simply as the difference between average precipitation and evapotranspiration rates. Lacking evapotranspiration measurements, minimum and maximum estimate of NIR calculated as 17 and 23% of the precipitation in the region based on long-term measurements (Gondwe *et al*., 2010) were used. By applying the 17 and 23% to the average precipitation for the study period, which was determined from the precipitation record to be 3.75 mm d^{-1} or 4.34 x 10^{-8} m s^{-1}, the NIR is calculated to be between 7.38 x 10^{-9} m s^{-1} and 9.98 x 10^{-9} m s^{-1} at the study site.

The Q_{MBW}, or mean volumetric conduit flow through the MBW ($m^3\ s^{-1}$), is calculated as

(4.3) $$Q_{MBW} = u \times A_{MBW}$$

where u is the average current velocity ($m\ s^{-1}$) within the MBW, and A_{MBW} is the average cross-sectional area (m^2) of the portion of the cave conduit that contains the MBW.

Average current velocity (u) is estimated from a point measurement of flow velocity in the MBW. The tilt-current meter deployed at ~17 m water depth measured flow velocity in the high-flow portion of the MBW regime (near the mid-point of the cross-section), not accounting for expected disparity in water velocity distribution across the passage. However, velocity distribution within a cave conduit varies between sub-regimes of maximum and minimum velocity. Sub-regimes with the lowest flow are often close to zero velocity and they can make up a substantial portion of the conduit cross-section (Beddows, 2004). To account for the minimal flow sub-regimes within MBW, the actual water velocity measurements during the study period (0.068 $m\ s^{-1}$, on average) are averaged with the expected minimal flow regimes (0 $m\ s^{-1}$) to get a conservative estimate of the mean water velocity (u = 0.034 $m\ s^{-1}$) across the passage.

To determine A_{MBW}, or the average cross-sectional area of the MBW (m^2), the following equation is used:

(4.4) $$A_{MBW} = A_{conduit} \times f_{MBW}$$

where $A_{conduit}$ is the full cross-sectional area of the passage (33.1 m^2) calculated based on estimated passage dimensions and f_{MBW} is the fraction of the MBW in the passage (0.9) based on the known position of haloclines within the conduit (see Chapter III; see Supplemental Material), which results in A_{MBW} = 30 m^2. Only the flowing-MBW fraction of the conduit's cross-sectional area is used for the calculation, because zero flow velocity, and therefore zero transport and consumption, is assumed for the top MFW and the bottom SGW. This assumption is based on the geomorphically protected

nature of the MFW (Fig. 15-16) and the velocity measurements in the saline groundwater.

Calculations based on Eq. (4.3) and Eq. (4.4) result in an estimated mean volumetric flow (Q_{MBW}) in the MBW of 1.02 $m^3\ s^{-1}$, which is in close agreement with discharge rates from single passages measured in the region (Beddows, 2004). Nevertheless, I recognize the calculations above represent a crude estimation of the volumetric flow in the MBW regime. Measuring actual evapotranspiration rates on the surface, or recording temporal halocline dynamics and mapping the full extent of the flow velocity distribution in the cross-sectional conduit, for example with the use of acoustic current doppler profiler (Ganju *et al.*, 2012), will help future investigations to provide more accurate volumetric flow calculations and use them for the concept introduced here. Using Eq. (4.4), Q_{MBW} (1.02 $m^3\ s^{-1}$) and the range of NIR values (7.38 x 10^{-9} m s^{-1} to 9.98 x 10^{-9} m s^{-1}), it is calculated that the effective area of the subterranean drainage basin (A_{SDB}) is between 1.02 x 10^8 and 1.38 x 10^8 m^2 (or 102 to 138 km^2).

To determine the integrated methane consumption rate (MCR_{int}), the quantity of methane consumed within the subterranean drainage basin (mg CH_4 yr^{-1}) during the study period, the following equation is used:

$$MCR_{int} = C_{ox} \times Q_{MBW} \tag{4.5}$$

where Q_{MBW} (1.02 $m^3\ s^{-1}$ converted to 3.23 x 10^{-8} $m^3\ yr^{-1}$) is the volumetric flow (see above) and C_{ox} is the amount of methane consumed by methane oxidation (mg m^{-3}) in the system determined by conservative mixing calculations, a method that has been successfully applied in a variety of environments (Chanton and Lewis, 1999; Pohlman *et al.*, 2008). C_{ox} is calculated as

$$C_{ox} = C_{mix} - C_{MBW} \tag{4.6}$$

where C denotes concentration of methane converted from nM to mg m^{-3}. C_{mix} is the expected methane concentration in MBW if there was only physical mixing between

water masses and C_{MBW} is the methane concentration actually measured. C_{mix} is calculated as,

$$C_{mix} = f_{MFW}\, C_{MFW} + (1 - f_{MFW})\, C_{SGW} \quad (4.7)$$

where C_{MFW} and C_{SGW} are the endmember methane concentrations from the lowest (MFW) and highest (SGW) salinity regimes, respectively. The fraction of the fresh endmember (f_{MFW}) present in the mixture is calculated from chloride concentrations as

$$f_{MFW} = \frac{[Cl^-]_{SGW} - [Cl^-]_{mix}}{[Cl^-]_{SGW} - [Cl^-]_{MFW}} \quad (4.8)$$

where $[Cl^-]$ denotes chloride concentration within the respective water mass (subscripts MFW, MBW, or SGW). In this study, $[Cl^-]$ content is reported in salinity, therefore, $[Cl^-]$ in Eq. (4.8) is substituted with salinity to determine f_{MFW}.

For the above calculations, methane concentration and salinity time-series records obtained from MFW and MBW are averaged for the study period within the representative water mass for each chemical property, resulting in values of 6,073 ± 255 nM for C_{MFW}, 277 ± 85 nM for C_{MBW}, 0.27 ± 0.01 psu for MFW-salinity, and 1.89 ± 0.01 psu for MBW-salinity. For the SGW, reported values of average salinity (SGW-salinity = 32.84 ± 0.94 psu) and methane concentration (C_{SGW} = 110 ± 17 nM) are used (see Chapter II). Using Eq. (4.6), it is calculated that the C_{ox}, or the amount of methane consumed within each m^3 of mixed water is 5,540,000 nmol (or 89 mg m^{-3}), which is 91% of the original methane content. Inserting C_{ox} (89 mg m^{-3}) into Eq. (4.5) indicates the 2.56 x 10^9 mg CH_4 yr^{-1} was consumed within the Cenote Bang drainage basin during this dry season study. Inserting MCR_{int} and the minimum and maximum A_{SDB} values into Eq. (4.1), it is calculated that the rate of methane consumption within the drainage basin of the subterranean estuary, or MCR_{area}, is between 21 and 28 mg CH_4 m^{-2} yr^{-1}.

The estimated methane consumption rate of 21 to 28 mg m^{-2} yr^{-1} during the dry season (Fig. 20) for the catchment area of this subterranean estuary is about 1-2% of the rates estimated for a barrier island subterranean estuary (1,446 mg m^{-2} yr^{-1}) (Schutte *et al*., 2016), 2-3% of rates described from pristine forest soils (1,050 mg m^{-2} yr^{-1}) (Price *et*

al., 2004), and about 3-5% of the oxidation rate determined for shelf seas with active methane seepage (584 mg m^{-2} yr^{-1}) (Thornton *et al*., 2016). The methane consumption rate calculated in this study is expected to be higher with the integration of wet season methane dynamics and, thus, my assumption is that the current assessment is a conservative estimate for oxidation rates in karst subterranean estuaries. The relative importance of these dynamic coastal aquifers in methane budgets should be more carefully evaluated during future studies, especially considering that the recent rise in atmospheric methane concentrations has been attributed to an increase in tropical biogenic methane emissions (Nisbet *et al*., 2016).

Summary

Evidence presented above indicates year-around input and consumption of methane in cave conduits flooded by the karst subterranean estuary. Methane is consumed at an estimated rate of 21-28 mg m^{-2} yr^{-1} for the surface area of subterranean estuary drainage basin (Fig. 20). Methane transport and methanotrophic activity in the coastal aquifer is impacted by small- and large-scale mixing pathways that are driven by hydrological mechanisms linked to meteorological and tidal changes in the unconfined coastal aquifer. Key drivers of small-scale mixing processes include tidal oscillation, evapotranspiration, and low-intensity rainfall. Large-scale mixing, on the other hand, is driven by precipitation leading hydrological processes, such as recharge- and flow-induced mixing in the conduits. The year-long record reveals sub-seasonal and seasonal patterns in the relative role of these mixing pathways and subsequent hydro-biogeochemical processes. These findings made it possible to build a landscape model, with a temporal component, by integrating the time-series records with a previously described generic model of ecosystem function (see Chapter II). These observations are significant from an ecological point of view because they support that a microbial loop, supplying methane as carbon and energy for higher levels of the food web, is continuously active in this carbonate coastal aquifer. Moreover, these findings expand our knowledge on the constraints that control the balance between the production,

consumption and transport of methane before it is emitted from the karst subterranean estuary by submarine groundwater discharge into the coastal sea.

CHAPTER V
SUMMARY AND OUTLOOK

Recognition that coastal ocean chemistry is altered by submarine groundwater discharge (e.g., Kwon *et al*., 2014; Moore, 2010) has raised awareness of the need to understand internal carbon cycling within subterranean estuaries, a key biogeochemical transition zone altering the chemical composition of discharging coastal groundwater (e.g., Gonneea *et al*., 2014; Moore, 1999). Along the margins of coastal carbonate platforms, karst subterranean estuaries (KSEs) extend kilometers inland (e.g., Beddows *et al*., 2007; Gonneea *et al*., 2014), creating an extensive system of diverse habitats and sub-habitats across physicochemical gradients developed due to differences in organic matter and oxygen availability, and the mixing of meteoric fresh water and saline groundwater. This environment harbors a poorly understood, but globally dispersed, anchialine ecosystem with diverse endemic cave-adapted fauna (Bishop *et al*., 2015; Iliffe and Kornicker, 2009; Stock *et al*., 1986). One of the key goals of my dissertation research was to expand the basic understanding of anchialine ecosystem function (Pohlman *et al*., 1997) by testing the viability of a hypothesized conceptual model for an oligotrophic sub-habitat within the anchialine ecosystem (Pohlman, 2011). By accessing the subsurface environment through flooded cave passages, I developed and applied state-of-the-art research tools to describe the spatial and temporal controls that govern the basic ecosystem function in this environment, with an emphasis on the role of methane and dissolved organic matter (DOM) as components of the carbon cycle. I measured the distribution, concentration and isotopic composition of biotic and abiotic components of an anchialine ecosystem to identify the energetic sources and biogeochemical processes that mediate organic matter flow and sustain life in an oligotrophic sub-habitat within a karst subterranean estuary of the Yucatan Peninsula, Mexico.

As demonstrated in Chapter II, a primary finding of my research is that a microbial loop shuttles methane and DOM to higher trophic levels of the anchialine food

web. Methane and DOM production and consumption within the coastal groundwater corresponded with a microbial community capable of methanotrophy, heterotrophy and chemoautotrophy, based on characterization by 16S rRNA amplicon sequencing and respiratory quinone composition. Fatty acid and bulk stable carbon isotope values of cave-adapted shrimp suggested that carbon from methanotrophic bacteria comprises, on average, 21% (ranging from 0-55%) of their diet. These findings reveal a heretofore unrecognized "upside-down" methane sink and contribute to our understanding of the carbon cycle and ecosystem function of an oligotrophic sub-habitat within an inland karst subterranean estuary.

The sampling protocol in Chapter II did not provide sufficient vertical resolution of the water column chemistry to identify spatial details of the biogeochemical processes occurring across sharp density interfaces separating the water masses. In Chapter III, undisturbed cm-scale vertical profiles of methane concentrations and isotopic composition were obtained with the 'OctoPiPi' (OPP) water sampler (developed as part of my dissertation project) across density interfaces in the water column of a flooded cave system. A 12-24 cm transition zone separated high concentration (1,272 to 7,793 nM) and ^{13}C-depleted methane (−58.1‰ to −67.5‰) in anoxic fresh water layer near the ceiling of the cave from hypoxic, brackish water containing lower methane concentrations (37 to 132 nM) with relatively ^{13}C-enriched δ^{13}C values (−47.8‰ to −55.5‰). Similar biogeochemical activity was not observed at the well-known pycnocline between the meteoric lens and the saline groundwater. The results were incorporated into conservative mixing and kinetic isotope models that identified a hotspot for microbial methane oxidation within the stratified groundwater. These data provide novel insight into the spatial dynamics of methane oxidation within a coastal karst subterranean estuary.

In Chapter IV, hydro-biogeochemical controls of methane dynamics were evaluated in the karst subterranean estuary study site to quantify the magnitude of methane consumption in the region. From wet and dry seasons, high temporal resolution (2.5-day timescale) records of dissolved methane concentrations and its stable carbon

isotopic content were obtained from osmotically-driven pumps (OsmoSamplers) deployed in the meteoric layers of the stratified water column. Within the meteoric fresh water, methane was more abundant (5,949 ± 132 nM) and depleted in ^{13}C (−65.2 ± 0.5‰) during the dry season than during the wet season (4,361 ± 89 nM; −65.8 ± 0.7‰). Analysis of coincident environmental data (water level, current velocity, groundwater temperature, air temperature, and precipitation) suggested these differences were related to precipitation-induced hydrologic changes within the tropical karst subterranean estuary. The integrated methane consumption rate for the catchment area during the dry season was calculated to be between 21 and 28 mg CH_4 m^{-2} yr^{-1}. This first-order estimate confirms that KSEs are a sink for methane formed in overlying terrestrial soils, but the magnitude of the sink is small relative to other systems where methane consumption has been quantified (e.g., 584 and 1,446 mg CH_4 m^{-2} yr^{-1}; Price *et al*., 2004; Schutte *et al*., 2016; Thornton *et al*., 2016). Further research is required to fully assess the magnitude of the sink on larger spatial and temporal scales.

Findings of my research are significant from an ecological point of view because they support that a microbial loop, supplying methane as carbon and energy for higher levels of the food web, is continuously active in this KSE. This observation is akin to the microbial loop that recycles DOM into the food web in the oligotrophic ocean (Azam *et al*., 1983; Fenchel, 2008) and in lakes (Weisse *et al*., 1990). Proof that the transport and microbial consumption of methane within the KSE is controlled by dynamic hydrology contributes to the increasing lines of evidence that the quantity of methane expelled by submarine groundwater discharge along coastlines (Cable *et al*., 1996; Kim and Hwang, 2002) is regulated within the subterranean estuary (Schutte *et al*., 2016). Given that methane is a powerful greenhouse gas and DOM is one of the largest carbon reservoirs on Earth, this study directly contributes to our understanding of their sources, sinks and interactions with microbial communities in coastal regions, all of which are fundamental to our knowledge of global oceanic biogeochemical cycles**.** At the societal level, information regarding constituent transport and the response of salinity to meteorological events have direct implications to better understand factors affecting

water quality in a region where rapid developments in recent years (Metcalfe *et al*., 2011) threaten the groundwater resources that human populations have been historically dependent on (Curtis *et al*., 1996; Van Hengstum *et al*., 2010).

Important questions regarding the characteristics of bioavailable DOM beyond methane and bulk DOC, as well as the mass flux of these materials in KSEs remain unresolved. Among the potential DOM constituents, volatile organic compounds, including naturally occurring acids and alcohols, are especially interesting because their dynamics are linked to important biogeochemical processes (e.g., methanol is linked to methane production and consumption). Moreover, these compounds are rich sources of energy and carbon for microbes, yet, we know very little about their regulation and transport in any environment. Therefore, one of my key goals is to evaluate the fate and ecological significance of volatile organic compounds in anchialine ecosystems within KSEs and quantify their contribution to DOM into the coastal ocean. In addition, future studies should investigate linkages between microbes and processes (e.g., using stable isotope probing and fluorescent *in situ* hybridization), focus on a more comprehensive identification of microbial assemblages, improve the models for the quantification of the magnitude of the "upside-down" methane sink, investigate regional and sub-regional controls on the observed biogeochemical processes and differences between ecosystem models from different geographical regions, and explore the effects of diverse trophic interactions within the food web on carbon flow.

REFERENCES

Alvarez, F., Iliffe, T.M., Benitez, S., Brankovits, D. and Villalobos, J.L. (2015) New records of anchialine fauna from the Yucatan Peninsula, Mexico. Check List 11, 1505.

Azam, F., Fenchel, T., Field, J.G., Gray, J.S., Meyerreil, L.A. and Thingstad, F. (1983) The ecological role of water-column microbes in the sea. Marine Ecology Progress Series 10, 257-263.

Back, W., Hanshaw, B.B., Herman, J.S. and Van Driel, J.N. (1986) Differential dissolution of a Pleistocene reef in the ground-water mixing zone of coastal Yucatan, Mexico. Geology 14, 137-140.

Barker, J.F. and Fritz, P. (1981) Carbon isotope fractionation during microbial methane oxidation. Nature 293, 289-291.

Bastviken, D., Cole, J., Pace, M. and Tranvik, L. (2004) Methane emissions from lakes: Dependence of lake characteristics, two regional assessments, and a global estimate. Global Biogeochemical Cycles 18, 4009.

Bastviken, D., Cole, J.J., Pace, M.L. and Van de Bogert, M.C. (2008) Fates of methane from different lake habitats: Connecting whole-lake budgets and CH_4 emissions. Journal of Geophysical Research: Biogeosciences 113, 2024.

Bastviken, D., Ejlertsson, J., Sundh, I. and Tranvik, L. (2003) Methane as a source of carbon and energy for lake pelagic food webs. Ecology 84, 969-981.

Bastviken, D., Tranvik, L.J., Downing, J.A., Crill, P.M. and Enrich-Prast, A. (2011) Freshwater methane emissions offset the continental carbon sink. Science 331, 50-50.

Bauer-Gottwein, P., Gondwe, B.R., Charvet, G., Marín, L.E., Rebolledo-Vieyra, M. and Merediz-Alonso, G. (2011) the Yucatán Peninsula karst aquifer, Mexico. Hydrogeology Journal 19, 507-524.

Bauer, J.E. and Druffel, E.R.M. (1998) Ocean margins as a significant source of organic matter to the deep open ocean. Nature 392, 482-485.

Bauer, J.E., Druffel, E.R.M., Wolgast, D.M. and Griffin, S. (2001) Sources and cycling of dissolved and particulate organic radiocarbon in the northwest Atlantic continental margin. Global Biogeochemical Cycles 15, 615-636.

Beddows, P., Smart, P., Whitaker, F. and Smith, S. (2002) Density stratified groundwater circulation on the Caribbean Coast of the Yucatan Peninsula, Mexico. Karst Frontiers. Karst Waters Institute Special Publication 7, 129-134.

Beddows, P.A. (2004) Groundwater hydrology of a coastal conduit carbonate aquifer: Caribbean coast of the Yucatán Peninsula, México. University of Bristol, Bristol.

Beddows, P.A., Smart, P.L., Whitaker, F.F. and Smith, S.L. (2007) Decoupled fresh-saline groundwater circulation of a coastal carbonate aquifer: Spatial patterns of temperature and specific electrical conductivity. Journal of Hydrology 346, 18-32.

Bishop, R.E., Humphreys, W.F., Cukrov, N., Zic, V., Boxshall, G.A., Cukrov, M., Iliffe, T.M., Krsinic, F., Moore, W.S., Pohlman, J.W. and Sket, B. (2015) 'Anchialine' redefined as a subterranenan estuary in crevicular or cavernous geological setting. Journal of Crustacean Biology 35, 511-514.

Blees, J., Niemann, H., Wenk, C.B., Zopfi, J., Schubert, C.J., Kirf, M.K., Veronesi, M.L., Hitz, C. and Lehmann, M.F. (2014) Micro-aerobic bacterial methane oxidation in the chemocline and anoxic water column of deep south-Alpine Lake Lugano (Switzerland). Limnology and Oceanography 59, 311-324.

Bligh, E.G. and Dyer, W.J. (1959) A rapid method of total lipid extraction and purification. Canadian Journal of Biochemistry and Physiology 37, 911-917.

Boetius, A. and Wenzhofer, F. (2013) Seafloor oxygen consumption fuelled by methane from cold seeps. Nature Geoscience 6, 725-734.

Cable, J.E., Bugna, G.C., Burnett, W.C. and Chanton, J.P. (1996) Application of ^{222}Rn and CH_4 for assessment of groundwater discharge to the coastal ocean. Limnology and Oceanography 41, 1347-1353.

Callahan, B.J., McMurdie, P.J., Rosen, M.J., Han, A.W., Johnson, A.J.A. and Holmes, S.P. (2016) DADA2: High-resolution sample inference from Illumina amplicon data. Nature Methods 13, 581-583.

Canfield, D.E., Stewart, F.J., Thamdrup, B., De Brabandere, L., Dalsgaard, T., Delong, E.F., Revsbech, N.P. and Ulloa, O. (2010) A cryptic sulfur cycle in oxygen-minimum-zone waters off the Chilean coast. Science 330, 1375-1378.

Chanton, J.P. and Lewis, F.G. (1999) Plankton and dissolved inorganic carbon isotopic composition in a river-dominated estuary: Apalachicola Bay, Florida. Estuaries 22, 575-583.

Collins, J.R., Edwards, B.R., Fredricks, H.F. and Van Mooy, B.A. (2016) LOBSTAHS: an adduct-based lipidomics strategy for discovery and identification of oxidative stress biomarkers. Analytical Chemistry 88, 7154-7162.

Collins, M. and Jones, D. (1981) Distribution of isoprenoid quinone structural types in bacteria and their taxonomic implication. Microbiological Reviews 45, 316-354.

Collins, M.D. and Green, P.N. (1985) Isolation and characterization of a novel coenzyme Q from some methane-oxidizing bacteria. Biochemical and Biophysical Research Communications 133, 1125-1131.

Corliss, J.B., Baross, J.A. and Hoffman, S.E. (1981) An hypothesis concerning the relationship between submarine hot springs and the origin of life on Earth. Oceanologica Acta SP, 59-69.

Corliss, J.B., Dymond, J., Gordon, L.I., Edmond, J.M., Herzen, R.P.V., Ballard, R.D., Green, K., Williams, D., Bainbridge, A., Crane, K. and Vanandel, T.H. (1979) Submarine thermal springs on the Galapagos Rift. Science 203, 1073-1083.

Coutino, A., Stastna, M., Kovacs, S. and Reinhardt, E. (2017) Hurricanes Ingrid and Manuel (2013) and their impact on the salinity of the Meteoric Water Mass, Quintana Roo, Mexico. Journal of Hydrology 551, 715-729.

Curtis, J.H., Hodell, D.A. and Brenner, M. (1996) Climate variability on the Yucatan Peninsula (Mexico) during the past 3500 years, and implications for Maya cultural evolution. Quaternary Research 46, 37-47.

Dalsgaard, J., John, M.S., Kattner, G., Müller-Navarra, D. and Hagen, W. (2003) Fatty acid trophic markers in the pelagic marine environment. Advances in marine biology 46, 225-340.

Damm, E., Schauer, U., Rudels, B. and Haas, C. (2007) Excess of bottom-released methane in an Arctic shelf sea polynya in winter. Continental Shelf Research 27, 1692-1701.

Deines, P., Wooller, M.J. and Grey, J. (2009) Unravelling complexities in benthic food webs using a dual stable isotope (hydrogen and carbon) approach. Freshwater Biology 54, 2243-2251.

DelVecchia, A.G., Stanford, J.A. and Xu, X. (2016) Ancient and methane-derived carbon subsidizes contemporary food webs. Nature Communications 7, 13163.

Devlin, S.P., Saarenheimo, J., Syväranta, J. and Jones, R.I. (2015) Top consumer abundance influences lake methane efflux. Nature Communications 6, 8787.

Elling, F.J., Becker, K.W., Könneke, M., Schröder, J.M., Kellermann, M.Y., Thomm, M. and Hinrichs, K.U. (2016) Respiratory quinones in Archaea: phylogenetic distribution and application as biomarkers in the marine environment. Environmental Microbiology 18, 692-707.

Fenchel, T. (2008) The microbial loop–25 years later. Journal of Experimental Marine Biology and Ecology 366, 99-103.

Ford, D. and Williams, P.D. (2013) Karst Hydrogeology and Geomorphology. John Wiley & Sons, West Sussex

Fry, B. (2007) Stable Isotope Ecology. Springer Science & Business Media, New York.

Ganju, N.K., Hayn, M., Chen, S.-N., Howarth, R.W., Dickhudt, P.J., Aretxabaleta, A.L. and Marino, R. (2012) Tidal and groundwater fluxes to a shallow, microtidal estuary: constraining inputs through field observations and hydrodynamic modeling. Estuaries and Coasts 35, 1285-1298.

Gondwe, B.R., Lerer, S., Stisen, S., Marín, L., Rebolledo-Vieyra, M., Merediz-Alonso, G. and Bauer-Gottwein, P. (2010) Hydrogeology of the south-eastern Yucatan Peninsula: new insights from water level measurements, geochemistry, geophysics and remote sensing. Journal of Hydrology 389, 1-17.

Gonneea, M.E., Charette, M.A., Liu, Q., Herrera-Silveira, J.A. and Morales-Ojeda, S.M. (2014) Trace element geochemistry of groundwater in a karst subterranean estuary (Yucatan Peninsula, Mexico). Geochimica et Cosmochimica Acta 132, 31-49.

Gonzalez, B.C., Singpiel, A. and Schlagner, P. (2013) *Godzillius fuchsi*, a new species of Remipedia (Godzilliidae) from Abaco Island, Bahamas. Journal of Crustacean Biology 33, 275-285.

Greenberg, R., Marra, P.P., Wooller, M.J. and Dufty Jr, A. (2007) Stable-isotope (C, N, H) analyses help locate the winter range of the coastal plain Swamp Sparrow (*Melospiza georgiana nigrescens*). The Auk 124, 1137-1148.

Grey, J. (2016) The incredible lightness of being methane-fuelled: stable isotopes reveal alternative energy pathways in aquatic ecosystems and beyond. Frontiers in Ecology and Evolution 4, 8.

Grinsted, A., Moore, J.C. and Jevrejeva, S. (2004) Application of the cross wavelet transform and wavelet coherence to geophysical time series. Nonlinear Processes in Geophysics 11, 561-566.

He, R., Wooller, M.J., Pohlman, J.W., Tiedje, J.M. and Leigh, M.B. (2015) Methane-derived carbon flow through microbial communities in arctic lake sediments. Environmental Microbiology 17, 3233-3250.

Hobbs, H.H., Hobbs, H. and Daniel, M.A. (1977) A Review of the Troglobitic Decapod Crustaceans of the Americas. Smithsonian Institution Press, Washington.

Hummel, J., hruthi Segu, S., Li, Y., Irgang, S., Jueppner, J. and Giavalisco, P. (2011) Ultra performance liquid chromatography and high resolution mass spectrometry for the analysis of plant lipids. Computational Approaches in Aid of Advancing Understanding in Plant Physiology 2, 73.

Humphreys, W. (1999) Physico-chemical profile and energy fixation in Bundera Sinkhole, an anchialine remiped habitat in north-western Australia. Journal of the Royal Society of Western Australia 82, 89-98.

Iliffe, T.M. and Kornicker, L.S. (2009) Worldwide diving discoveries of living fossil animals from the depths of anchialine and marine caves. Smithsonian Contributions to Marine Sciences 38, 269-280.

IPCC (2014) Climate Change 2014–Impacts, Adaptation and Vulnerability: Regional Aspects. Cambridge University Press, New York.

Jannasch, H. (1985) Review lecture: The chemosynthetic support of life and the microbial diversity at deep-sea hydrothermal vents. Proceedings of the Royal Society of London B: Biological Sciences 225, 277-297.

Kambesis, P.N. and Coke, J.G. (2013) Overview of the controls on eogenetic cave and karst development in Quintana Roo, Mexico, Coastal Karst Landforms. Springer, pp. 347-373.

Kankaala, P., Taipale, S., Grey, J., Sonninen, E., Arvola, L. and Jones, R.I. (2006) Experimental $\delta^{13}C$ evidence for a contribution of methane to pelagic food webs in lakes. Limnology and Oceanography 51, 2821-2827.

Kessler, J., Reeburgh, W. and Tyler, S. (2006) Controls on methane concentration and stable isotope ($\delta^{2}H$-CH_4 and $\delta^{13}C$-CH_4) distributions in the water columns of the Black Sea and Cariaco Basin. Global Biogeochemical Cycles 20, 4004.

Kim, G. and Hwang, D.W. (2002) Tidal pumping of groundwater into the coastal ocean revealed from submarine ^{222}Rn and CH_4 monitoring. Geophysical Research Letters 29, 14.

Koenemann, S., Schram, F.R., Iliffe, T.M., Hinderstein, L.M. and Bloechl, A. (2007) Behavior of Remipedia in the laboratory, with supporting field observations. Journal of Crustacean Biology 27, 534-542.

Kornicker, L.S. and Yager, J. (2002) Description of *Spelaeoecia saturno*, a new species from an anchialine cave in Cuba, (Crustacea: Ostracoda: Myodocopa: Halocyprididae). Proceedings of the Biological Society of Washington 115, 153-170.

Kottek, M., Grieser, J., Beck, C., Rudolf, B. and Rubel, F. (2006) World map of the Köppen-Geiger climate classification updated. Meteorologische Zeitschrift 15, 259-263.

Kovacs, S.E., Reinhardt, E.G., Stastna, M., Coutino, A., Werner, C., Collins, S.V., Devos, F. and Le Maillot, C. (2017) Hurricane Ingrid and Tropical Storm Hanna's effects on the salinity of the coastal aquifer, Quintana Roo, Mexico. Journal of Hydrology 551, 703-714.

Kroopnick, P. (1980) The Distribution of C-13 in the Atlantic-Ocean. Earth and Planetary Science Letters 49, 469-484.

Kwon, E.Y., Kim, G., Primeau, F., Moore, W.S., Cho, H.M., DeVries, T., Sarmiento, J.L., Charette, M.A. and Cho, Y.K. (2014) Global estimate of submarine groundwater discharge based on an observationally constrained radium isotope model. Geophysical Research Letters 41, 8438-8444.

Lalonde, K., Middlestead, P. and Gélinas, Y. (2014) Automation of $^{13}C/^{12}C$ ratio measurement for freshwater and seawater DOC using high temperature combustion. Limnology and Oceanography: Methods 12, 816-829.

Lapham, L.L., Chanton, J.P., Martens, C.S., Higley, P.D., Jannasch, H.W. and Woolsey, J.R. (2008) Measuring temporal variability in pore-fluid chemistry to assess gas hydrate stability: Development of a continuous pore-fluid array. Environmental Science & Technology 42, 7368-7373.

Lee, Y.W., Kim, G., Lim, W.A. and Hwang, D.W. (2010) A relationship between submarine groundwater-borne nutrients traced by Ra isotopes and the intensity of dinoflagellate red-tides occurring in the southern sea of Korea. Limnology and Oceanography 55, 1-10.

Legates, D.R. and McCabe, G.J. (1999) Evaluating the use of "goodness-of-fit" measures in hydrologic and hydroclimatic model validation. Water Resources Research 35, 233-241.

Leonte, M., Kessler, J.D., Kellermann, M.Y., Arrington, E.C., Valentine, D.L. and Sylva, S.P. (2017) Rapid rates of aerobic methane oxidation at the feather edge of

gas hydrate stability in the waters of Hudson Canyon, US Atlantic Margin. Geochimica et Cosmochimica Acta 204, 375-387.

Levin, L.A. (2005) Ecology of cold seep sediments: interactions of fauna with flow, chemistry and microbes. Oceanography and Marine Biology: An Annual Review 43, 1-46.

Lowell, N.S., Walsh, D.R. and Pohlman, J.W. (2015) A comparison of tilt current meters and an acoustic doppler current meter in vineyard sound, Massachusetts. Current, Waves and Turbulence Measurement 11, 1-7.

Magen, C., Lapham, L.L., Pohlman, J.W., Marshall, K., Bosman, S., Casso, M. and Chanton, J.P. (2014) A simple headspace equilibration method for measuring dissolved methane. Limnology and Oceanogaphy: Methods 12, 637-650.

Martin, J.B., Gulley, J. and Spellman, P. (2012) Tidal pumping of water between Bahamian blue holes, aquifers, and the ocean. Journal of Hydrology 416, 28-38.

Menning, D.M., Wynn, J.G. and Garey, J.R. (2015) Karst estuaries are governed by interactions between inland hydrological conditions and sea level. Journal of Hydrology 527, 718-733.

Metcalfe, C.D., Beddows, P.A., Bouchot, G.G., Metcalfe, T.L., Li, H.X. and Van Lavieren, H. (2011) Contaminants in the coastal karst aquifer system along the Caribbean coast of the Yucatan Peninsula, Mexico. Environmental Pollution 159, 991-997.

Meyer, J. (1994) The microbial loop in flowing waters. Microbial Ecology 28, 195-199.

Moore, W.S. (1999) The subterranean estuary: a reaction zone of ground water and sea water. Marine Chemistry 65, 111-125.

Moore, W.S. (2010) The effect of submarine groundwater discharge on the ocean. Annual Review of Marine Science 2, 59-88.

Moore, W.S., Sarmiento, J.L. and Key, R.M. (2008) Submarine groundwater discharge revealed by 228Ra distribution in the upper Atlantic Ocean. Nature Geoscience 1, 309-311.

Nichols, P.D., Guckert, J.B. and White, D.C. (1986) Determination of monosaturated fatty acid double-bond position and geometry for microbial monocultures and complex consortia by capillary GC-MS of their dimethyl disulphide adducts. Journal of Microbiological Methods 5, 49-55.

Niemann, H., Linke, P., Knittel, K., MacPherson, E., Boetius, A., Bruckmann, W., Larvik, G., Wallmann, K., Schacht, U., Omoregie, E., Hilton, D., Brown, K. and Rehder, G. (2013) Methane-carbon flow into the benthic food web at cold seeps – a case study from the Costa Rica Subduction Zone. Plos One 8, 10.

Nisbet, E., Dlugokencky, E., Manning, M., Lowry, D., Fisher, R., France, J., Michel, S., Miller, J., White, J. and Vaughn, B. (2016) Rising atmospheric methane: 2007–2014 growth and isotopic shift. Global Biogeochemical Cycles 30, 1356-1370.

Nowicka, B. and Kruk, J. (2010) Occurrence, biosynthesis and function of isoprenoid quinones. Biochimica et Biophysica Acta (BBA)-Bioenergetics 1797, 1587-1605.

Opsahl, S.P. and Chanton, J.P. (2006) Isotopic evidence for methane-based chemosynthesis in the Upper Floridan aquifer food web. Oecologia 150, 89-96.

Pakes, M.J., Weis, A.K. and Mejía-Ortiz, L. (2014) Arthropods host intracellular chemosynthetic symbionts, too: cave study reveals an unusual form of symbiosis. Journal of Crustacean Biology 34, 334-341.

Paull, C.K., Hecker, B., Commeau, R., Freemanlynde, R.P., Neumann, C., Corso, W.P., Golubic, S., Hook, J.E., Sikes, E. and Curray, J. (1984) Biological communities at the Florida escarpment resemble hydrothermal vent taxa. Science 226, 965-967.

Peel, M.C., Finlayson, B.L. and McMahon, T.A. (2007) Updated world map of the Köppen-Geiger climate classification. Hydrology and earth system sciences discussions 4, 439-473.

Perry, E., Velazquez-Oliman, G. and Marin, L. (2002) The hydrogeochemistry of the karst aquifer system of the northern Yucatan Peninsula, Mexico. International Geology Review 44, 191-221.

Peterson, B.J. and Fry, B. (1987) Stable isotopes in ecosystem studies. Annual Review of Ecology and Systematics, 293-320.

Pohlman, J.W. (2011) The biogeochemistry of anchialine caves: progress and possibilities. Hydrobiologia 677, 33-51.

Pohlman, J.W., Bauer, J.E., Waite, W.F., Osburn, C.L. and Chapman, N.R. (2010) Methane hydrate-bearing seeps as a source of aged dissolved organic carbon to the oceans. Nature Geoscience 4, 37-41.

Pohlman, J.W., Iliffe, T.M. and Cifuentes, L.A. (1997) A stable isotope study of organic cycling and the ecology of an anchialine cave ecosystem. Marine Ecology Progress Series 155, 17-27.

Pohlman, J.W., Ruppel, C., Hutchinson, D.R., Downer, R. and Coffin, R.B. (2008) Assessing sulfate reduction and methane cycling in a high salinity pore water system in the northern Gulf of Mexico. Marine and Petroleum Geology 25, 942-951.

Popendorf, K.J., Fredricks, H.F. and Van Mooy, B.A. (2013) Molecular ion-independent quantification of polar glycerolipid classes in marine plankton using triple quadrupole MS. Lipids 48, 185-195.

Popp, B.N., Sansone, F.J., Rust, T.M. and Merritt, D.A. (1995) Determination of concentration and carbon isotopic composition of dissolved methane in sediments and nearshore waters. Analytical Chemistry 67, 405-411.

Preheim, S.P., Olesen, S.W., Spencer, S.J., Materna, A., Varadharajan, C., Blackburn, M., Friedman, J., Rodríguez, J., Hemond, H. and Alm, E.J. (2016) Surveys, simulation and single-cell assays relate function and phylogeny in a lake ecosystem. Nature Microbiology 1, 16130.

Price, S.J., Sherlock, R.R., Kelliher, F.M., McSeveny, T.M., Tate, K.R. and Condron, L.M. (2004) Pristine New Zealand forest soil is a strong methane sink. Global Change Biology 10, 16-26.

Reeburgh, W.S. (2007) Oceanic methane biogeochemistry. Chemical Reviews 107, 486-513.

Rubio, F., Rolán, E., Worsaae, K., Martínez, A. and Gonzalez, B.C. (2015) Description of the first anchialine gastropod from a Yucatán cenote, *Teinostoma brankovitsi* n. sp.(Caenogastropoda: Tornidae), including an emended generic diagnosis. Journal of Molluscan Studies 82, 169-177.

Santoro, A.E., Francis, C.A., de Sieyes, N.R. and Boehm, A.B. (2008) Shifts in the relative abundance of ammonia-oxidizing bacteria and archaea across physicochemical gradients in a subterranean estuary. Environmental Microbiology 10, 1068-1079.

Sarbu, S.M., Kane, T.C. and Kinkle, B.K. (1996) A chemoautotrophically based cave ecosystem. Science 272, 1953-1955.

Schutte, C.A., Wilson, A.M., Evans, T., Moore, W.S. and Joye, S.B. (2016) Methanotrophy controls groundwater methane export from a barrier island. Geochimica et Cosmochimica Acta 179, 242-256.

Seymour, J., Humphreys, W. and Mitchell, J. (2007) Stratification of the microbial community inhabiting an anchialine sinkhole. Aquatic Microbial Ecology 50, 11-24.

Simon, K., Benfield, E. and Macko, S. (2003) Food web structure and the role of epilithic biofilms in cave streams. Ecology 84, 2395-2406.

Simon, K.S., Pipan, T. and Culver, D.C. (2007) A conceptual model of the flow and distribution of organic carbon in caves. Journal of Cave and Karst Studies 69, 279-284.

Socki, R.A., Perry, E.C. and Romanek, C.S. (2002) Stable isotope systematics of two cenotes from the northern Yucatan Peninsula, Mexico. Limnology and Oceanography 47, 1808-1818.

Steinle, L., Graves, C.A., Treude, T., Ferré, B., Biastoch, A., Bussmann, I., Berndt, C., Krastel, S., James, R.H. and Behrens, E. (2015) Water column methanotrophy controlled by a rapid oceanographic switch. Nature Geoscience 8, 378-382.

Steinle, L., Maltby, J., Treude, T., Kock, A., Bange, H.W., Engbersen, N., Zopfi, J., Lehmann, M.F. and Niemann, H. (2017) Effects of low oxygen concentrations on aerobic methane oxidation in seasonally hypoxic coastal waters. Biogeosciences 14, 1631-1645.

Stock, J.H., Iliffe, T.M. and Williams, D. (1986) The concept anchialine reconsidered. Stygologia 2, 90-92.

Summons, R.E., Jahnke, L.L. and Roksandic, Z. (1994) Carbon isotopic fractionation in lipids from methanotrophic bacteria: relevance for interpretation of the geochemical record of biomarkers. Geochimica et Cosmochimica Acta 58, 2853-2863.

Taniguchi, M., Burnett, W.C., Cable, J.E. and Turner, J.V. (2002) Investigation of submarine groundwater discharge. Hydrological Processes 16, 2115-2129.

Thornton, B.F., Geibel, M.C., Crill, P.M., Humborg, C. and Mörth, C.M. (2016) Methane fluxes from the sea to the atmosphere across the Siberian shelf seas. Geophysical Research Letters 43, 5869-5877.

Tryon, M.D. and Brown, K.M. (2004) Fluid and chemical cycling at Bush Hill: Implications for gas-and hydrate-rich environments. Geochemistry, Geophysics, Geosystems 5, 12004.

Tryon, M.D., Brown, K.M., Torres, M.E., Tréhu, A.M., McManus, J. and Collier, R.W. (1999) Measurements of transience and downward fluid flow near episodic methane gas vents, Hydrate Ridge, Cascadia. Geology 27, 1075-1078.

van Hengstum, P.J., Reinhardt, E.G., Beddows, P.A. and Gabriel, J.J. (2010) Linkages between Holocene paleoclimate and paleohydrogeology preserved in a Yucatan underwater cave. Quaternary Science Reviews 29, 2788-2798.

van Hengstum, P.J., Scott, D.B., Grocke, D.R. and Charette, M.A. (2011) Sea level controls sedimentation and environments in coastal caves and sinkholes. Marine Geology 286, 35-50.

Wang, Q., Garrity, G.M., Tiedje, J.M. and Cole, J.R. (2007) Naive Bayesian classifier for rapid assignment of rRNA sequences into the new bacterial taxonomy. Applied and Environmental Microbiology 73, 5261-5267.

Weisse, T., Müller, H., Pinto-Coelho, R.M., Schweizer, A., Springmann, D. and Baldringer, G. (1990) Response of the microbial loop to the phytoplankton spring bloom in a large prealpine lake. Limnology and Oceanography 35, 781-794.

Wetzel, R.G. (1984) Detrital dissolved and particulate organic-carbon functions in aquatic ecosystems. Bulletin of Marine Science 35, 503-509.

Wetzel, R.G. (2001) Limnology: Lake and River Ecosystems. Academic Press, San Diego.

Whiticar, M.J. (1999) Carbon and hydrogen isotope systematics of bacterial formation and oxidation of methane. Chemical Geology 161, 291-314.

Young, M.B., Gonneea, M.E., Fong, D.A., Moore, W.S., Herrera-Silveira, J. and Paytan, A. (2008) Characterizing sources of groundwater to a tropical coastal lagoon in a karstic area using radium isotopes and water chemistry. Marine Chemistry 109, 377-394.

APPENDIX A

FIGURES

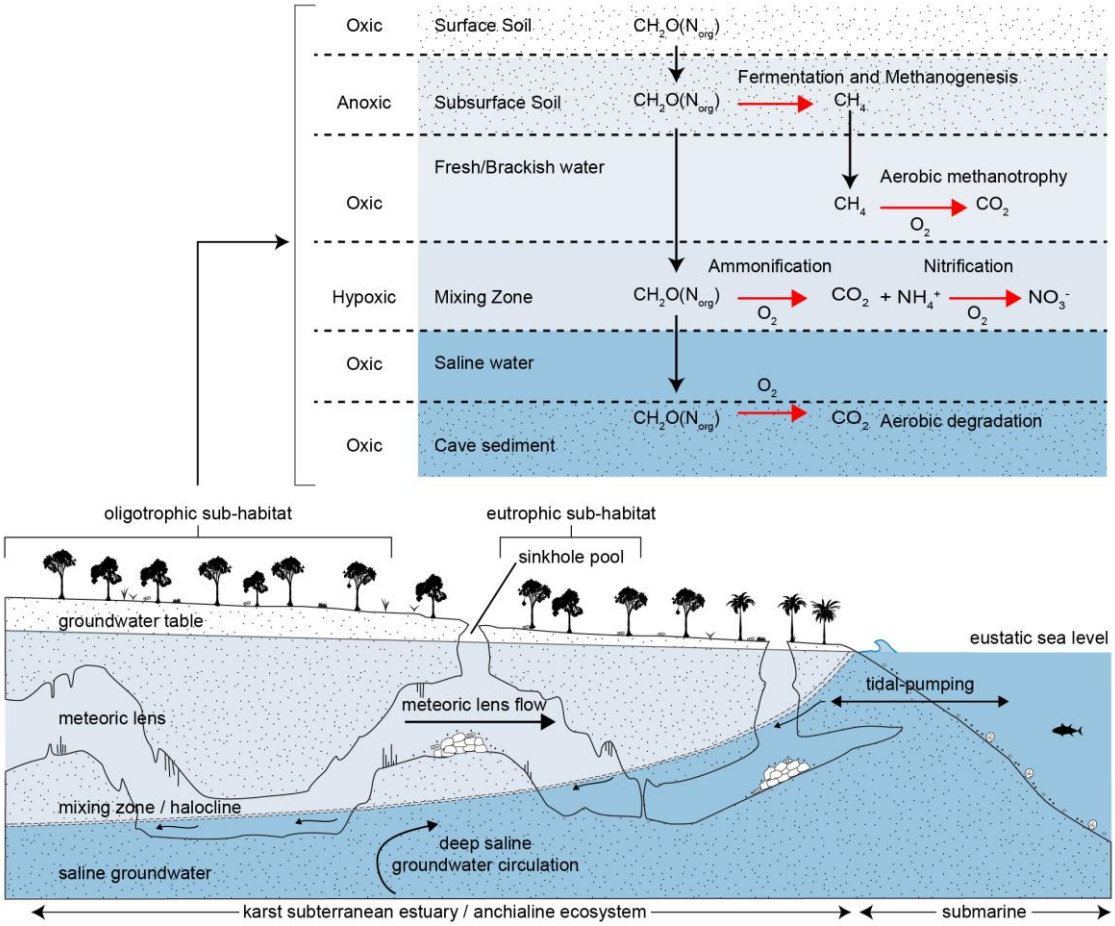

Figure 1: Conceptual model of a karst subterranean estuary, a typical environment for anchialine ecosystems. Karst subterranean estuary (bottom), adapted from van Hengstum *et al*. (2011). Hypothetical conceptual model of an oligotrophic sub-habitat (top) within the anchialine ecosystem, adapted from Pohlman (2011).

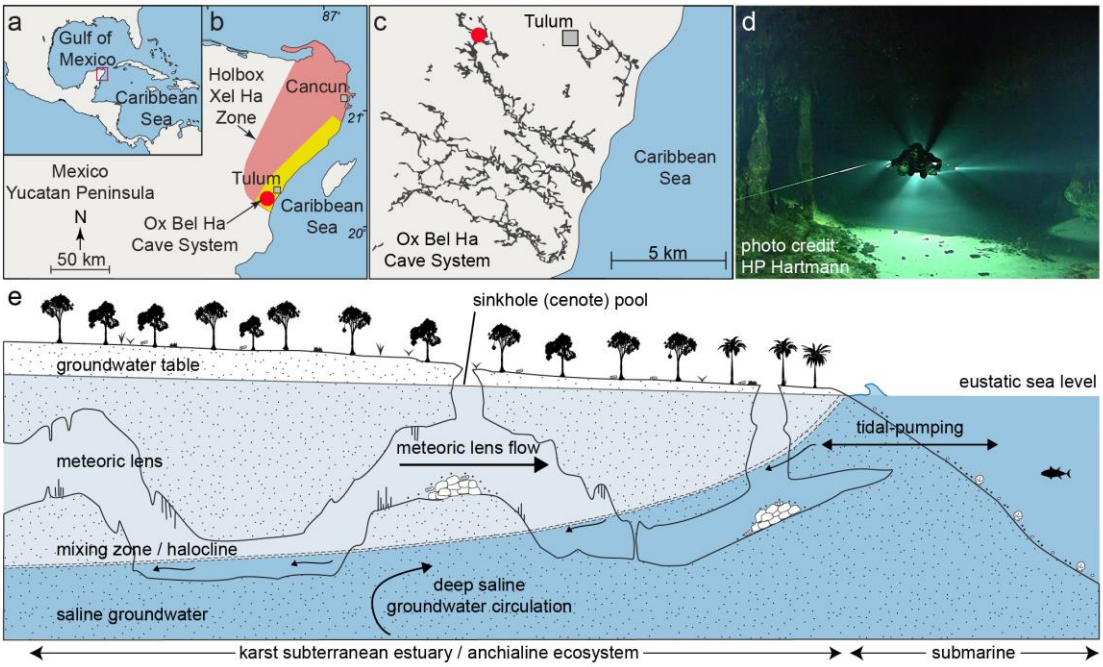

Figure 2: Study site and model for a karst subterranean estuary. (a) The Yucatan Peninsula. (b) In the Yucatan Peninsula (Mexico), coastal cave systems extend 12 km inland (yellow area) covering an area of ~1,100 km^2 within the Holbox Fracture Zone and Xel Ha Zone (red area) – adapted from Perry *et al*. (2002). (b) Mapped cave conduits of Ox Bel Ha Cave System (>240 km total length) – adapted from Kambesis & Coke (2013). Cenote Bang, the primary study site, is indicated by the red circle. (c) Cave diver within cave system Cenote Bang. (d) Conceptual model of a tropical karst subterranean estuary, a density stratified coastal aquifer – adapted from van Hengstum *et al*. (2011).

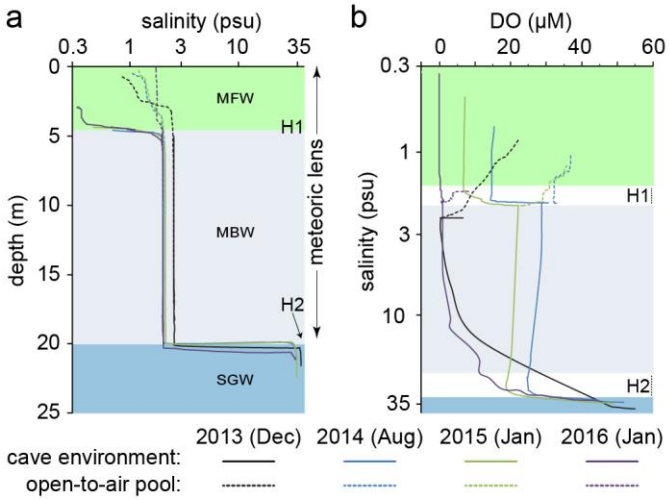

Figure 3: Physicochemical profiles from the density-stratified groundwater. (a) Salinity-depth profiles. (b) Dissolved oxygen-salinity profiles. Salinity is shown on a log-scale in both panels. Continuous lines are cave profiles, and dashed lines are open-to-air cenote pool (POOL) profiles. H1 (halocline 1) separates meteoric fresh water (MFW) from the meteoric brackish water (MBW), and H2 (halocline 2) separates the MBW from the saline groundwater (SGW).

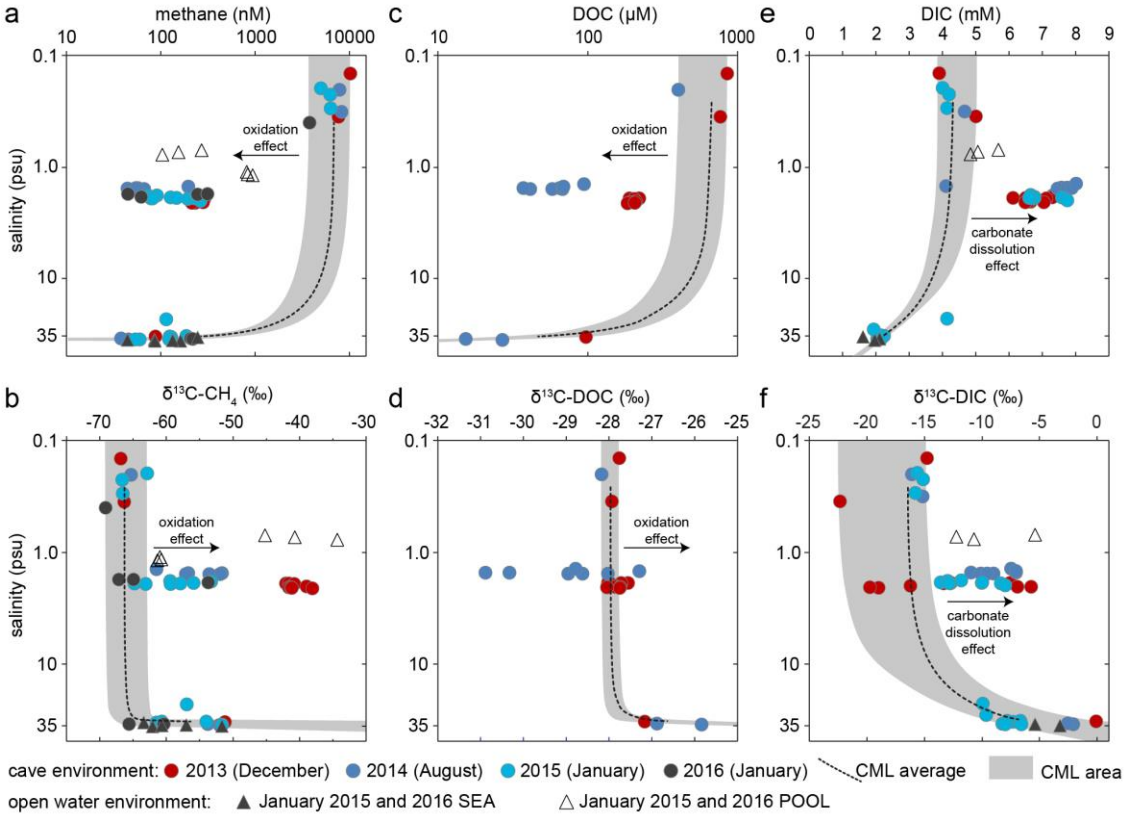

Figure 4: Salinity-property plots from the karst subterranean estuary. (a) methane concentrations (on log-scale). (b) Dissolved organic carbon (DOC) concentrations (on log-scale). (c) Dissolved inorganic carbon (DIC) concentrations. (d) methane stable carbon isotopic ($\delta^{13}C$) values. (e) DOC stable carbon isotopic ($\delta^{13}C$) values. (f) DIC stable carbon isotopic ($\delta^{13}C$) values. Salinity is shown on a log-scale in all panels. The average and total area of conservative mixing lines (CMLs) represent the trend predicted by the mixing model if there was only physical mixing between the meteoric fresh water and saline groundwater endmembers. Production yields an excess of the constituent relative to the CML average and area, while consumption results in depletion. Symbol of individual data points contain the uncertainty (std. dev.) of the measured values.

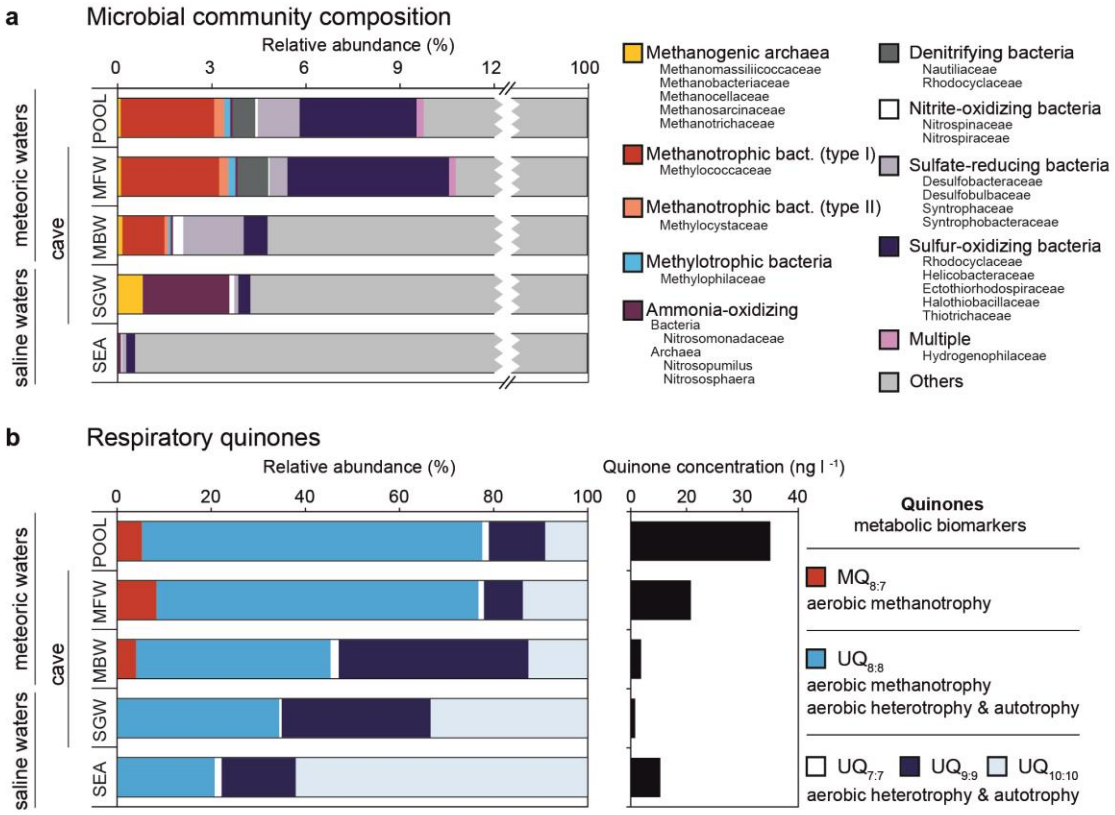

Figure 5: Microbial community diversity within the subterranean and surface water regimes. (a) 16S rRNA amplicon sequence community analysis. Functional groupings are based on the presence of sequences shared by microbes that mediate the associated function. 'Multiple' indicates there was no specific function associated with the closest match type strain. The majority of sequences were from bacteria and archaea capable of utilizing a variety of complex organic compounds. For a comprehensive phylogenetic listing and relative abundance of sequence reads see Supplemental Material. (b) Respiratory quinones relative abundance, concentrations and metabolic affiliations. Quinone nomenclature ($UQ_{m:n}$), after Elling *et al*. (2016), where Q indicates headgroup type, m number of isoprenoid units in the side chain and n number of double bonds. POOL = cenote pool; MFW = meteoric fresh water; MBW = meteoric brackish water; SGW = saline groundwater; SEA = coastal sea.

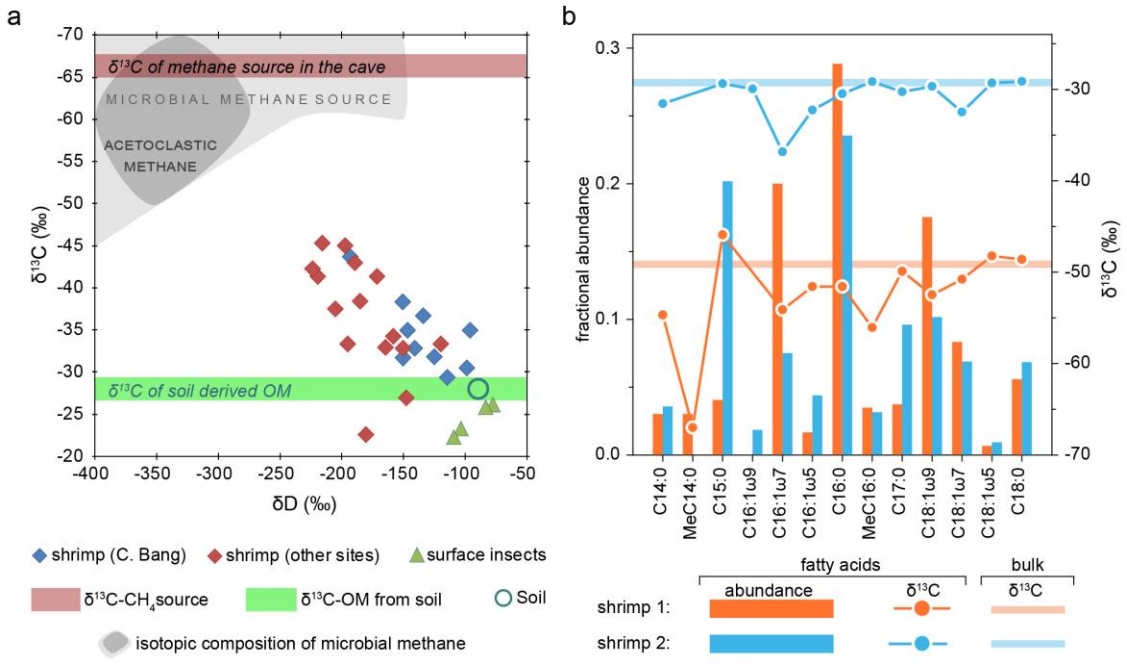

Figure 6: Stable isotopic content of food sources and consumers. (a) Carbon and deuterium stable isotope ratios ($^{13}C/^{12}C$, $^{2}H/^{1}H$) from stygobitic shrimp (diamonds) and surface insects (triangles) plotted relative to CH_4 and soil-derived organic matter (OM) endmembers. Proximity to source indicates relative trophic dependency. The $\delta^{13}C$ value of methane from the MFW (−66.3 ± 0.7‰, red shaded area) is consistent with a microbial source (grey shaded area; Whiticar, 1999). The $\delta^{13}C$ of the soil-derived OM (−28.0 ± 0.2‰, green shaded area) includes values for forest soil, cave POC and cave DOC. (b) Fatty acids from stygobitic shrimp specimens. Methane-derived carbon contribution is higher (55%) for shrimp 1 (orange) and lower (3%) for shrimp 2 (blue) based on bulk $\delta^{13}C$ values (−49.1 and −29.3‰, respectively). The combination of extremely ^{13}C-depleted $\delta^{13}C$ values and bacterial origins for odd-numbered monounsaturated and methylated FAs indicates a bacterial food source that is likely to include aerobic methanotrophs. Symbols of individual data points contain the uncertainty (std. dev.) of the measured isotopic values.

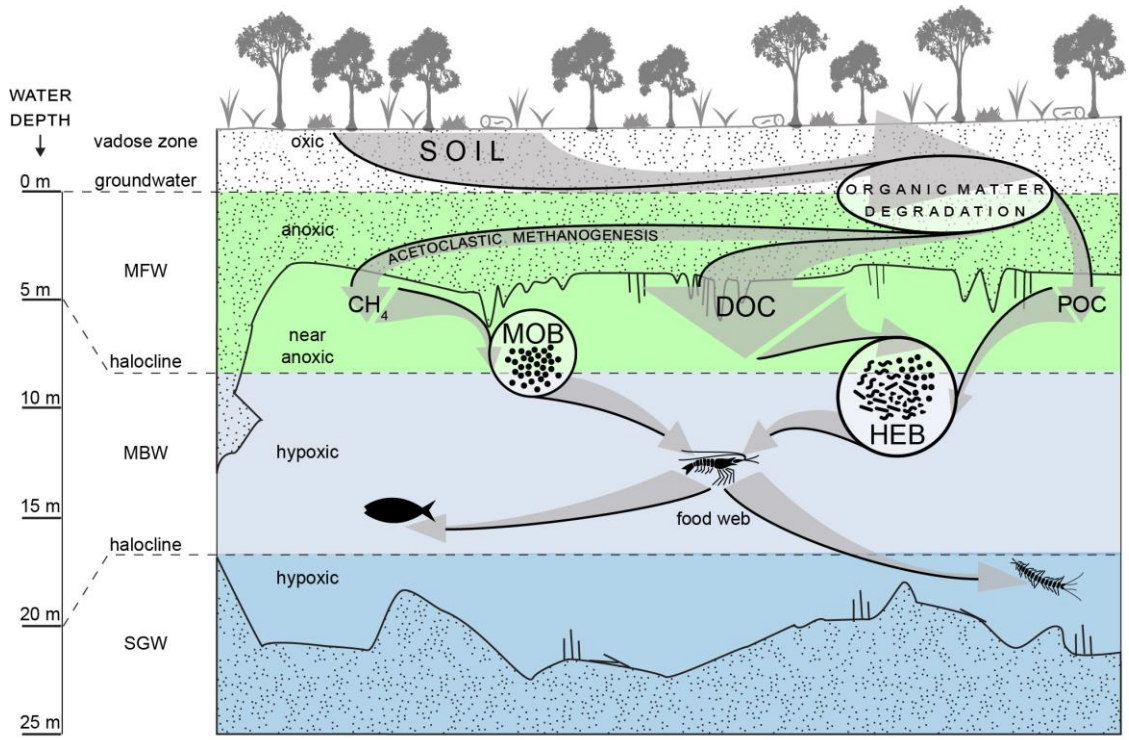

Figure 7: Conceptual model for a terrestrially-influenced tropical karst subterranean estuary microbial loop. Dissolved organic carbon (DOC) and methane (CH_4) produced from soil-derived organic matter degradation within the shallow and anoxic saturated zone of the carbonate rock-matrix are transported into hypoxic cave conduits, where methane oxidizing bacteria (MOB) and heterotrophic bacteria (HEB) consume these reduced forms of organic carbon. Bacterial biomass is assimilated by filter-feeding crustaceans that are, in turn, preyed upon by higher trophic consumers of the anchialine food web.

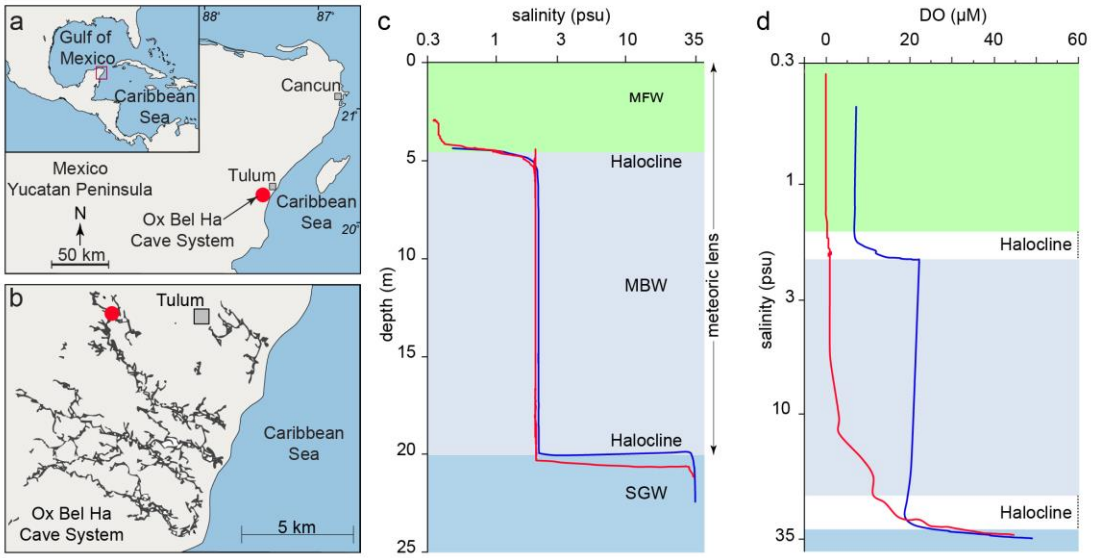

Figure 8: Field site and general structure of the density stratified water column. (a) Sampling site is located in the Yucatan Peninsula, Mexico. (b) Map of Ox Bel Ha Cave System showing the explored cave passages that provide direct access to the subterranean estuary. Red mark shows the sampling location 8 km inland from the coast. (c) Increasing salinity along a depth profile at the sampling site as sampled in January 2015 (blue line) and January 2016 (red line). A shallow halocline within the meteoric water layer separates meteoric fresh water (MFW) from meteoric brackish water (MBW). A deep halocline isolates the MBW from saline groundwater (SGW). (d) Salinity versus dissolved oxygen (DO) at the sampling site. Conditions were anoxic (<15 µM) to hypoxic (15 to 30 µM) in the MBW, where DO was higher in 2015 (blue line) than in 2016 (red line). MFW was anoxic and SGW was hypoxic (>40 µM) in both years.

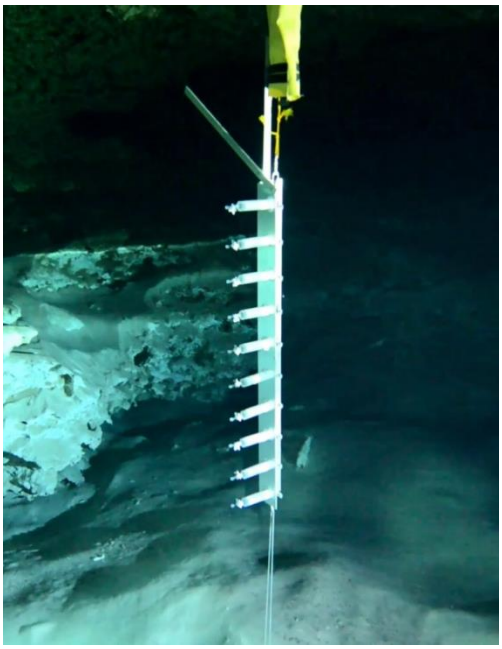

Figure 9: The OctoPiPi (OPP) deployed for sample collection in the cave environment. The OPP contains ten 60 ml syringes that are distributed 12 cm from each other. The smaller mini-OPP, which contained ten 60 ml syringes distributed 2.5 cm from each other, required the same deployment procedure.

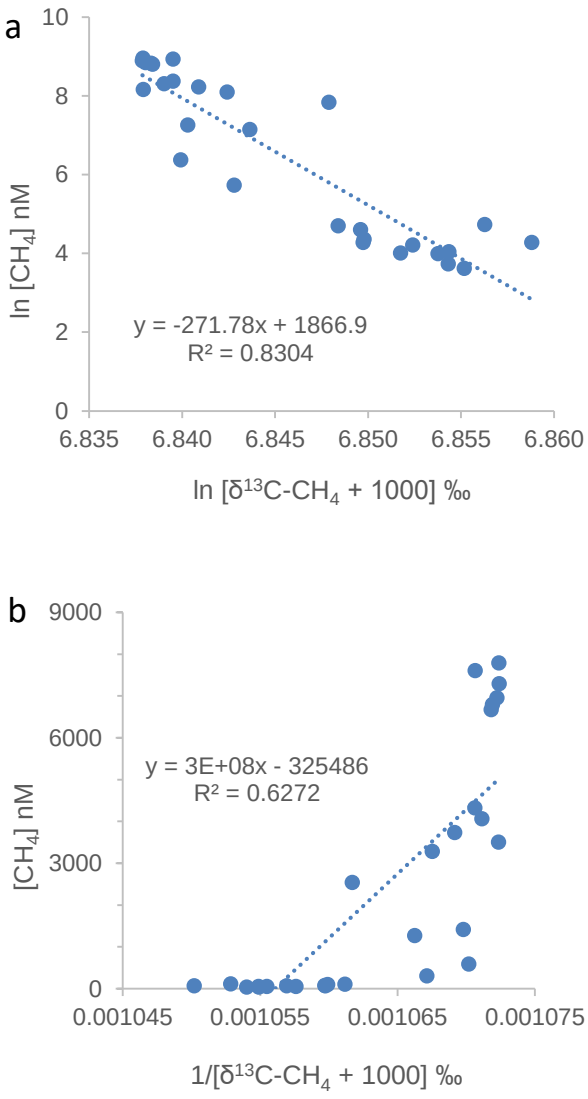

Figure 10: Methane concentration values plotted with $\delta^{13}C\text{-}CH_4$ ratios for the two different models. The linear regressions were used to calculate the fractionation factor (α) for the Rayleigh and open system kinetic isotope models. Plot (a) shows the regression for the Rayleigh model that resulted in $\alpha_c = 1.004$ using $slope_c = \alpha_c / (1 - \alpha_c)$ and plot (b) shows the regression for the open system model that resulted in $\alpha_o = 1.025$ using $slope_o = -(\alpha_o (\delta R_0 + 1000) C_o) / (1 - \alpha_o)$ (Leonte *et al.*, 2017). Source endmembers are C_0 = 7,544 nM and R_0 = −67.5‰ as described in methods.

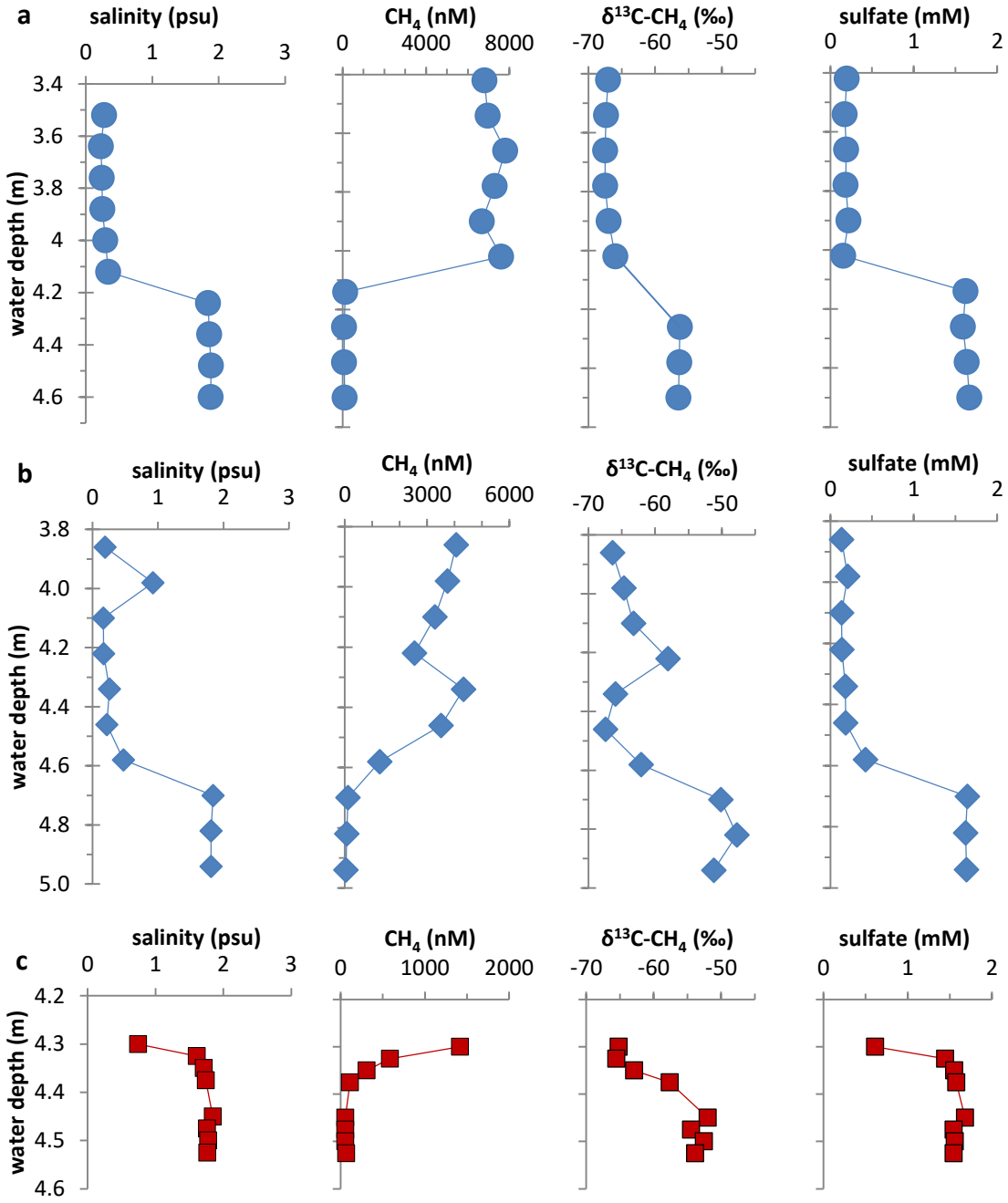

Figure 11: High-resolution spatial records of chemical constituents along depth profiles across the shallow halocline (MFW-MBW transition zone). Samples were collected (a) in January 2015 with the OctoPiPi (OPP) (circle), (b) in January 2016 with the OPP (diamond), and (c) in January 2016 with the mini-OPP (square). Symbol of individual data points contain the analytical uncertainty (std. dev.) of the measured values.

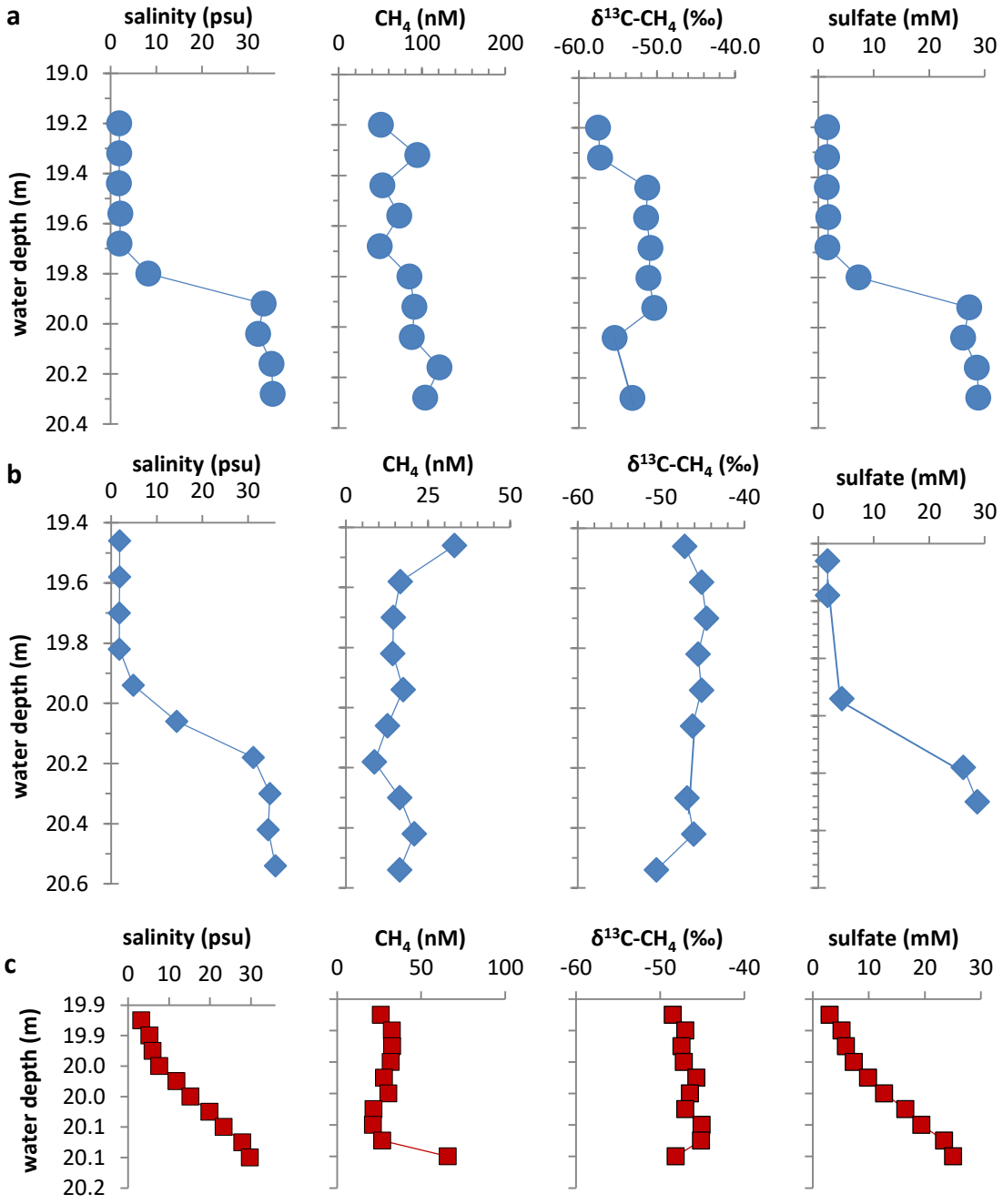

Figure 12: High-resolution spatial records of chemical constituents along depth profiles across the deep halocline (MBW-SGW transition zone). Samples were collected (a) in January 2015 with the OctoPiPi (OPP) (circle), (b) in January 2016 with the OPP (diamond), and (c) in January 2016 with the mini-OPP (square). Symbol of individual data points contain the analytical uncertainty (std. dev.) of the measured values.

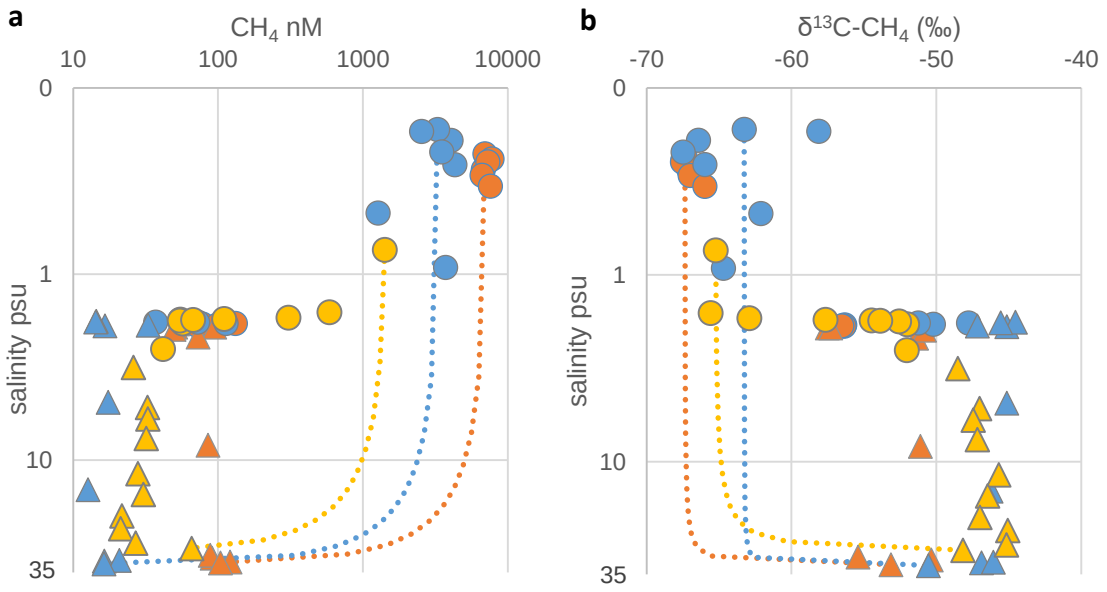

Figure 13: Salinity-property plots and the conservative mixing calculations. (a) Salinity-methane concentrations plotted on log-scale. (b) Salinity-$\delta^{13}C$-CH_4 values, where salinity is shown on a log-scale. Colors indicate different deployments: OPP deployment in January 2015 (orange); OPP deployment in January 2016 (blue); Mini-OPP deployment in January 2016 (yellow). Circles mark samples obtained at the shallow halocline (MFW-MBW transition zone). Triangles represent samples collected at the deep halocline (MBW-SGW transition zone). Dotted lines are conservative mixing model result for the respective period. The model result is the distribution expected for physical mixing only (no reactions) between the fresh and saline groundwater endmembers. Production yields an excess of the constituent relative to the conservative mixing model, while consumption results in depletion. Symbol of individual data points contain the analytical uncertainty (std. dev.) of the measured values.

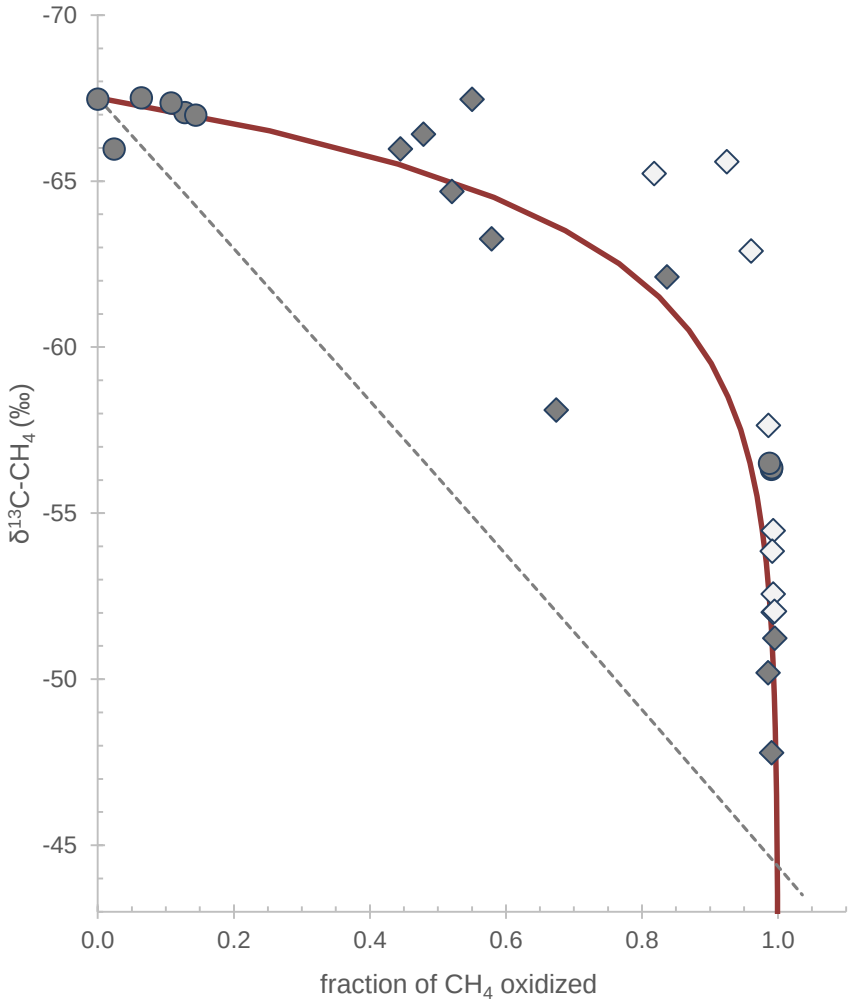

Figure 14: Plot comparing the measured data with calculations based on the Rayleigh and open system kinetic isotope models. The observed data series is a plot of measured $\delta^{13}C\text{-}CH_4$ against $f = 1 - C/C_0$ where C is the methane concentration of each sample collected across the MFW-MBW halocline and C_0 = 7,544 nM, is the assumed initial dissolved methane concentration based on the two highest measured values in the system (circles OPP 2015, gray diamonds OPP 2016, and white diamonds mini-OPP 2016). The fraction of methane oxidized was calculated separately for the Rayleigh model (solid line) and open system isotope model (dotted line) as described in detail by Leonte *et al*. (2017). The Rayleigh system kinetic isotope model results provide a better fit to the observed data than the open system kinetic isotope model.

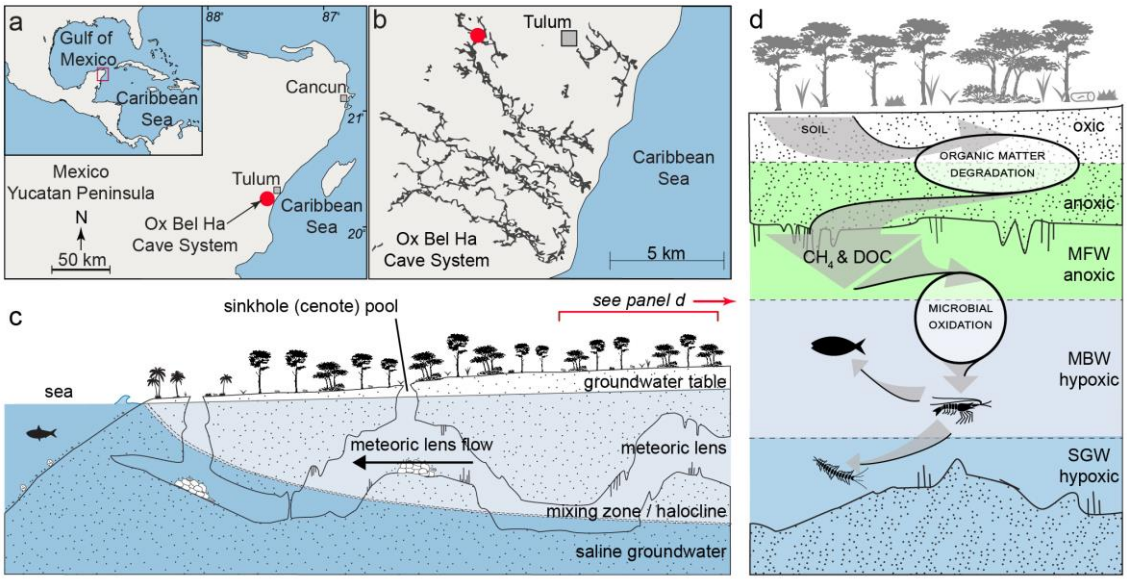

Figure 15: Field site and major biogeochemical processes in the subterranean estuary. (a) Field site is located in the Yucatan Peninsula, Mexico. (b) Map of Ox Bel Ha Cave System showing the explored cave passages that provide direct access to the subterranean estuary. Red mark shows the sampling location 8 km inland. (c) Conceptual model of a karst subterranean estuary. (d) Carbon and energy transfer. Methane (CH_4) and dissolved organic carbon (DOC) is oxidized in the aquifer by a microbial loop that provides carbon and energy for the food web. MFW is meteoric fresh water, MBW is meteoric brackish water, SGW is saline groundwater. Arrows are not scaled to magnitude of fluxes. Previous studies were not able to constrain the mechanisms that convey methane to the cave conduit from the overlying saturated rock-matrix.

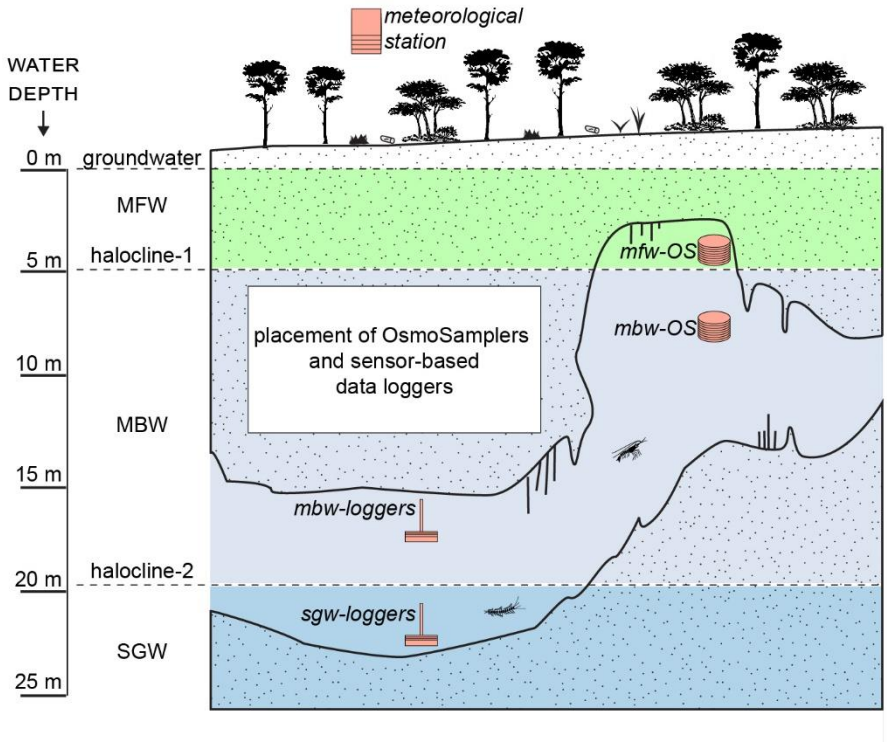

Figure 16: Placement of OsmoSamplers and sensor-based data loggers on the surface and within the flooded cave conduits at the study location. The meteorological station was installed on a roof of a house ~9 km away from the study site and it measured precipitation, barometric pressure and air temperature. The mfw-OS represents the shallow-OsmoSampler that was deployed in the meteoric fresh water (MFW) at ~3.5 m depth below the groundwater table, above halocline-1. The mbw-OS marks the deep-OsmoSampler that was deployed below halocline-1 in the meteoric brackish water (MBW) at ~7.5 m water depth. The mbw-logger station and the sgw-logger station were deployed at ~17 m and ~21 m, respectively, below the groundwater table. Each station measured water level, flow velocity and water temperature.

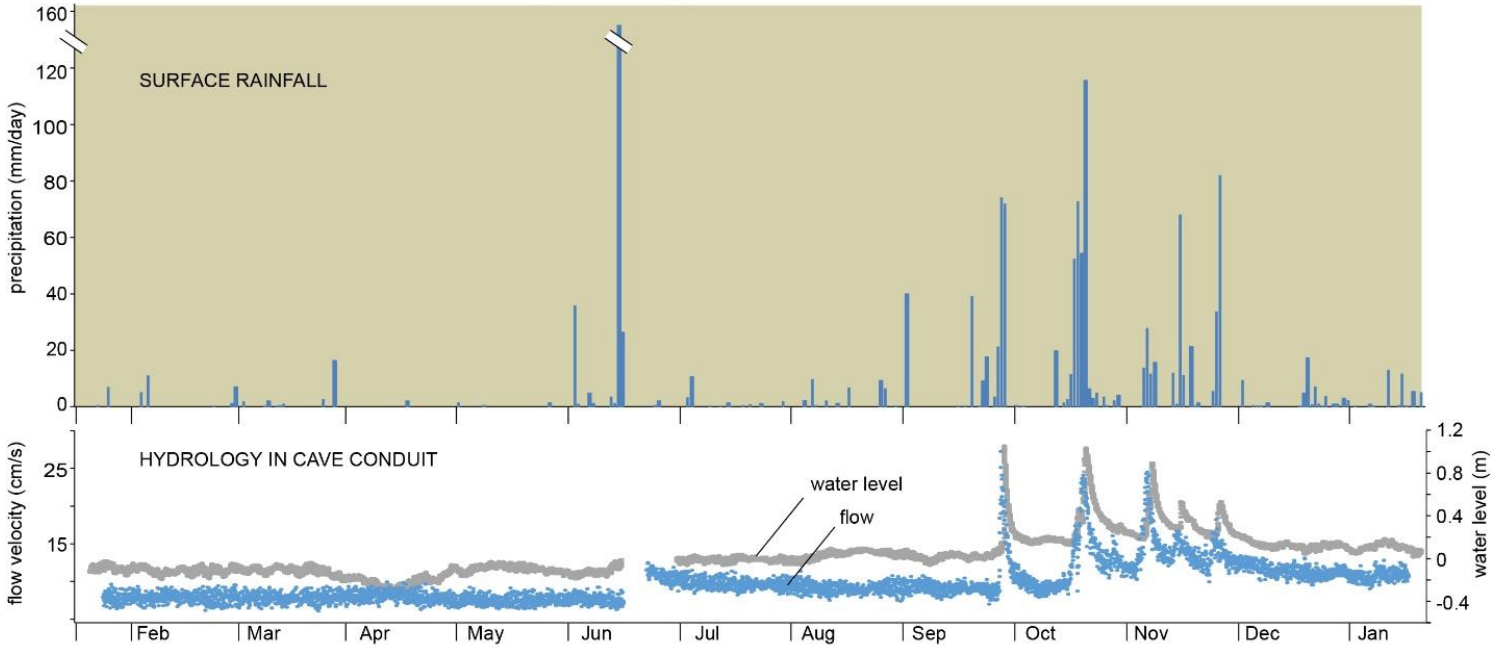

Figure 17: Meteorological and hydrological records. Precipitation record (upper) is shown together with the hydrological record (lower) obtained from the meteoric brackish water (MBW) and it includes flow velocity and water level.

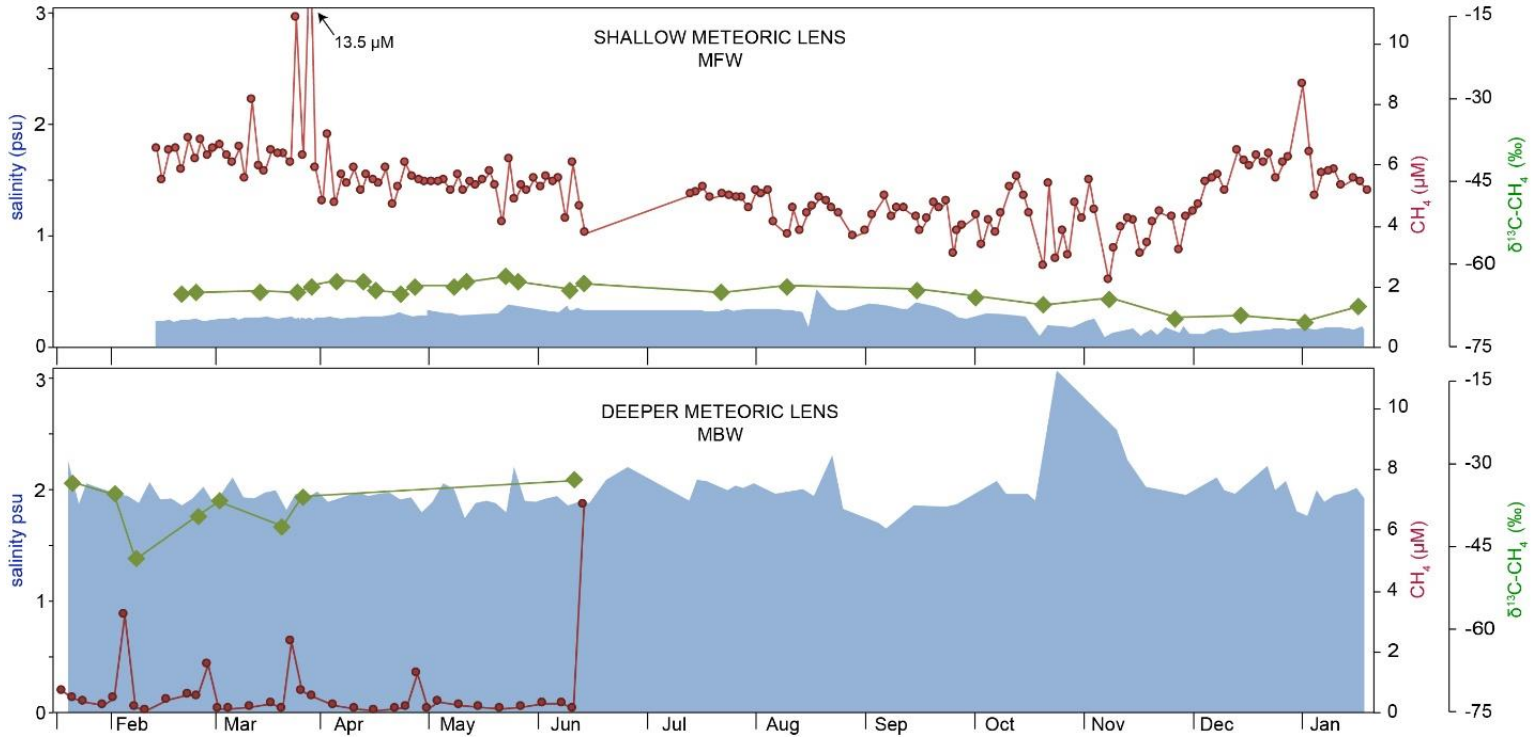

Figure 18: Simultaneous chemical records obtained from the shallow and deeper meteoric lens. Methane concentrations (red circles), $\delta^{13}C\text{-}CH_4$ (green diamond) and salinity (blue area) were measured at each monitoring station.

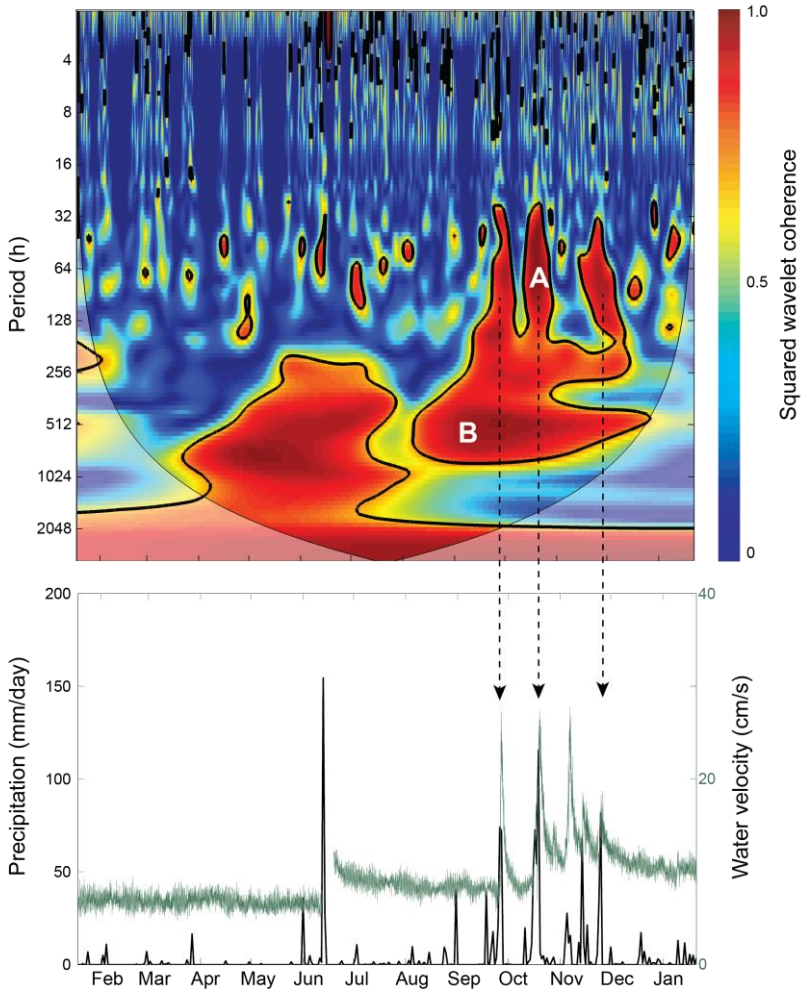

Figure 19: Wavelet coherence between precipitation and water velocity (upper), and time-series of precipitation and water velocity (lower). Again, elevated coherence occurs during episodic precipitation events (arrows), with peak coherence varying with each event. For example, the Oct 22 rainfall (A) had the highest coherence with water velocity at periods of approximately 30-100 h, with a phase lag averaging about 20 h (precipitation leading water velocity). This indicates that the highest coherence in power between the two time-series is on the order of 1-4 d, with a lag of approximately 1 d. The high-precipitation period between Oct-Dec leads to high coherence on the ~512 h (21 d) timescale (B), likely due to the frequency of precipitation events.

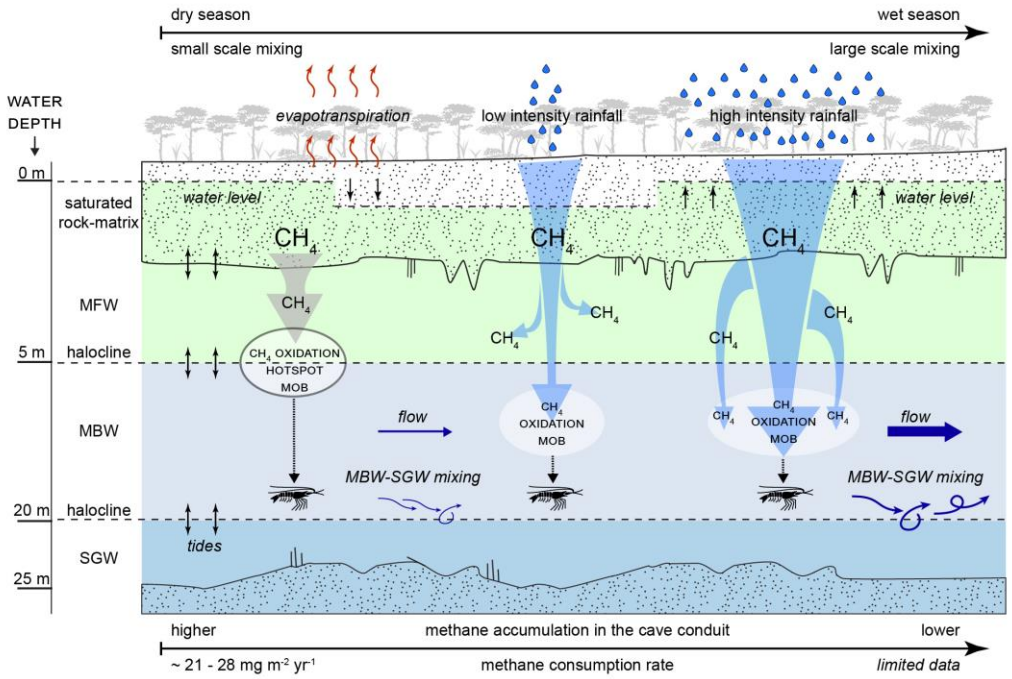

Figure 20: Conceptual landscape model showing dominant hydrological processes that impact methane dynamics in the cave system. The dry season is characterized by small-scale mixing mechanisms with occasional low-intensity precipitation events. Periodic tidal oscillation commingling constituents at the interfaces is an important mechanism that impels high methane concentrations from the saturated soil and rock-matrix into the cave conduit's MFW and that maintains a methane-oxidation-hotspot between the MFW and MBW. Occasional low-intensity rainfall is also capable of conveying methane into the cave environment and forcing methane-charged waters from the anoxic-MFW into the hypoxic-MBW. Methane oxidizing bacteria (MOB) are consumed by the cave-adapted shrimp (see Chapter II). The wet season is characterized by large-scale mixing scenarios due to regionally increased precipitation and a reduction in methane source concentrations in the MFW, which is consistent with conditions that weaken methanogenic pathways and/or promote methanotrophic processes. High-frequency and high-intensity rainfall drives source methane to deeper portions of the meteoric lens where methane that bypasses the methanotrophic "filter" is transported to the coastal ocean.

APPENDIX B

TABLES

Table 1: Aqueous Biogeochemistry. Values of water column constituents, presented as average ± std. error (n), from the different regimes of the groundwater system and the adjacent coastal sea. Values were calculated from all measurements within a water mass across all sampling events.

	meteoric fresh water **MFW**	meteoric brackish water **MBW**	saline groundwater **SGW**	sinkhole (cenote) **POOL**	coastal water **SEA**
Salinity (psu)	0.26 ± 0.03 (8)	1.81 ± 0.04 (29)	32.87 ± 0.94 (13)	0.94 ± 0.09 (6)	35.45 ± 0.39 (6)
$[SO_4^{2-}]$ mM	0.3 ± 0.1 (7)	1.6 ± 0. (27)	26.4 ± 1.0 (11)	0.8 ± 0.1 (6)	28.4 ± 0.6 (4)
$[CH_4]$ nM	6466 ± 659 (8)	157 ± 16 (28)	110 ± 17 (12)	495 ± 148 (6)	121 ± 28 (6)
$\delta^{13}C\text{-}CH_4$ ‰	−66.3 ± 0.7 (7)	−52.7 ± 1.9 (25)	−56.3 ± 1.5 (11)	−50.6 ± 4.9 (6)	−59.0 ± 2.1 (5)
[DOC] µM	661 ± 132 (3)	131 ± 16 (16)	41 ± 20 (3)	-	-
$\delta^{13}C$-DOC ‰	−28.0 ± 0.1 (3)	−28.3 ± 0.2 (16)	−26.6 ± 0.4 (3)	-	-
[DIC] mM	4.4 ± 0.2 (6)	7.1 ± 0.2 (24)	2.4 ± 0.2 (10)	5.3 ± 0.2 (3)	2.0 ± 0.1 (3)
$\delta^{13}C$-DIC ‰	−16.4 ± 1.0 (7)	−11.1 ± 0.7 (25)	−6.3 ± 1.0 (11)	−9.4 ± 2.1 (3)	−4.3 (2)
POC µM	10.9 ± 3.8 (3)	5.0 ± 2.3 (3)	3.0 ± 0.9 (3)	32.3 ± 14.9 (3)	5.8 (1)
$\delta^{13}C$-POC ‰	−28.5 ± 0.5 (3)	−27.6 ± 0.7 (3)	−27.1 ± 1.0 (3)	−28.0 ± 0.3 (3)	−20.1 (1)

Table 2: Summary of the chemical records from the shallow meteoric fresh water (MFW) and the deeper meteoric brackish water (MBW). Monthly periods of the dry season (Dec to May) and wet season (Jun to Nov) were determined based on precipitation patterns.

		CH_4 nM	Max. CH_4 nM	Min. CH_4 nM	$\delta^{13}C$-CH_4 ‰	Salinity psu
Shallow-MFW	Dry season	5,949 ± 132 (86)	13,551	4,093	−65.2 ± 0.5 (17)	0.24 ± 0.01 (77)
	Wet season	4,361 ± 89 (75)	6,073	2,165	−65.8 ± 0.7 (9)	0.28 ± 0.01 (57)
	Full record	**5,209 ± 102 (161)**	**13,551**	**2,165**	**−65.4 ± 0.4 (26)**	**0.26 ± 0.01 (134)**
		CH_4 nM baseline*	Max. CH_4 nM	Min. CH_4 nM	$\delta^{13}C$-CH_4 ‰	Salinity psu
Deeper-MBW	Dry season	216 ± 34 (28)	2,892	27	−38.8 ± 1.8 (7)	1.92 ± 0.01 (65)
	Wet season	179 ± 57 (3)	6,214	32	−33.2 (1)	1.98 ± 0.05 (26)
	Full record	**213 ± 31 (31)**	**6,214**	**27**	**−38.1 ± 1.7 (8)**	**1.94 ± 0.02 (91)**

Table 3: Results of correlation analysis of key meteorological and hydrological parameters. Pearson product-moment correlation coefficients are shown above for the (a) full record and for the dry (b) and (c) wet seasons. Monthly mean values of the following parameters were used for the analysis: air temperature (AIR TEMP.), precipitation (PRECIPIT.), water level (WATER L.), flow velocity (FLOW V.), salinity of meteoric brackish water (MBW SAL.) and salinity of meteoric fresh water (MFW SAL.).

(a) **Full Record**	*AIR TEMP.*	*PRECIPIT.*	*WATER L.*	*FLOW V.*	*MBW SAL.*	*MFW SAL.*
AIR TEMP.	1					
PRECIPIT.	0.19	1				
WATER L.	0.00	0.73	1			
FLOW V.	0.01	0.72	0.95	1		
MBW SAL.	−0.10	0.45	0.64	0.63	1	
MFW SAL.	0.74	−0.15	−0.57	−0.65	−0.51	1

(b) **Dry season**	*AIR TEMP.*	*PRECIPIT.*	*WATER L.*	*FLOW V.*	*MBW SAL.*	*MFW SAL.*
AIR TEMP.	1					
PRECIPIT.	−0.50	1				
WATER L.	−0.34	0.90	1			
FLOW V.	−0.24	0.91	0.94	1		
MBW SAL.	−0.41	0.30	0.38	0.34	1	
MFW SAL.	0.66	−0.97	−0.88	−0.95	−0.68	1

(c) **Wet season**	*AIR TEMP.*	*PRECIPIT.*	*WATER L.*	*FLOW V.*	*MBW SAL.*	*MFW SAL.*
AIR TEMP.	1					
PRECIPIT.	−0.90	1				
WATER L.	−0.74	0.65	1			
FLOW V.	−0.84	0.67	0.93	1		
MBW SAL.	−0.64	0.34	0.69	0.71	1	
MFW SAL.	0.88	−0.67	−0.91	−0.98	−0.82	1

Table 4: Summary of key drivers of hydrological processes that control the mixing and transport of chemical constituents in the groundwater. These mechanisms impact the distribution of major ions and organic matter reservoirs, including methane, in the karst subterranean estuary.

driver	mechanism	intensity of mixing	mixing effects	spatial / temporal extent
Evapotranspiration (ET)	ET-induced mixing	Small-scale	Downward mixing of MFW	Regional / sub-seasonal to seasonal
Tidal fluctuation	Tidal mixing & tidal pumping	Small- to intermediate-scale	Exchange at the interfaces. Horizontal transport.	Regional / tidal periods
Low-intensity precipitation	Recharge-induced mixing from rainfall low in intensity and/or frequency	Small- to intermediate-scale	Downward mixing of MFW	Local / hours to days
High-intensity precipitation	Recharge-induced mixing from rainfall high in intensity and/or frequency	Large-scale	Vertical exchange between MFW, MBW and SGW	Local to regional / hours to days
Conduit flow	Flow-induced mixing (as a result of recharge from high-intensity precipitation)	Large-scale	Vertical exchange between MBW and SGW	Regional / sub-seasonal to seasonal

APPENDIX C

SUPPLEMENTAL MATERIAL

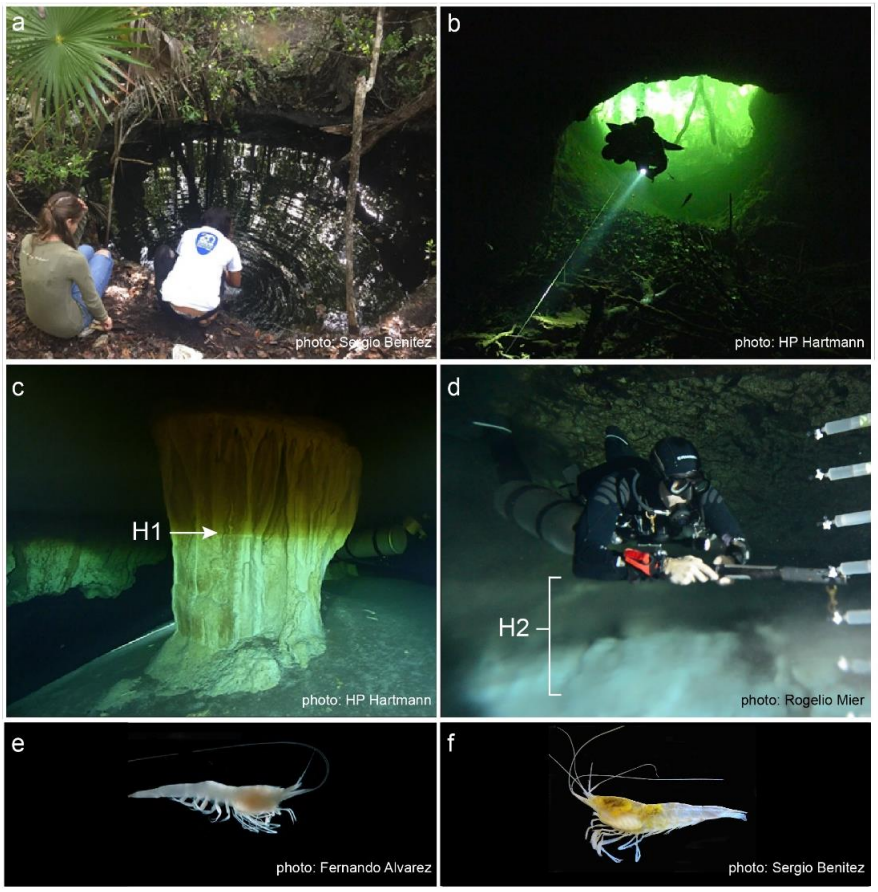

Supplementary Figure: (a) Entrance pool of Cenote Bang (20° 12.62' N 87° 30.06’ W). (b) Subsurface vantage of Cenote Bang entrance pool, the primary locations where particulate organic detritus enters the system without being filtered by the karst. (c) Shallow halocline (H1) ~4 m depth below the groundwater table is visibly distinguished by darker coloration of the shallower water mass. (d) Deeper halocline (H2) located at ~20 m depth below the groundwater table. (e) *Typhlatya mitchelli* and (f) *Typhlatya pearsei*, the two species of stygobitic atyid shrimp present at the primary research site.

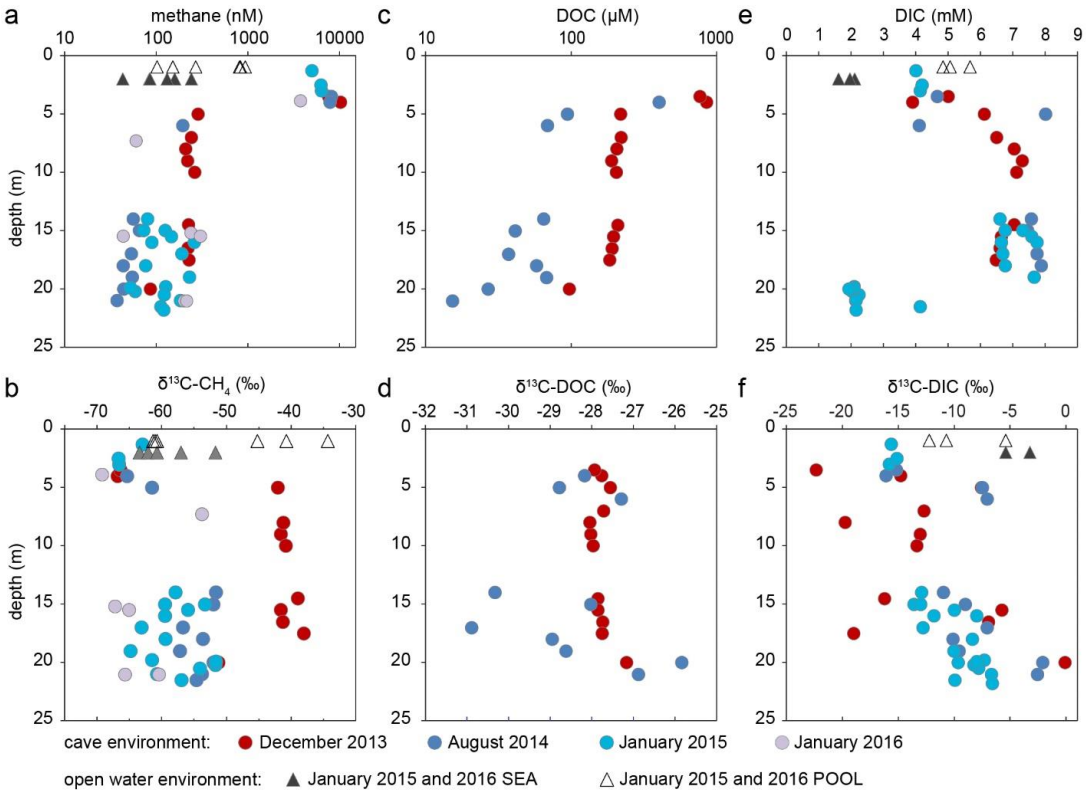

Supplementary Figure: Depth-property plots (concentration and carbon isotopic composition) for dissolved organic and inorganic carbon compounds. Symbols of individual data points contain the uncertainty (std. dev.) of the measured values.

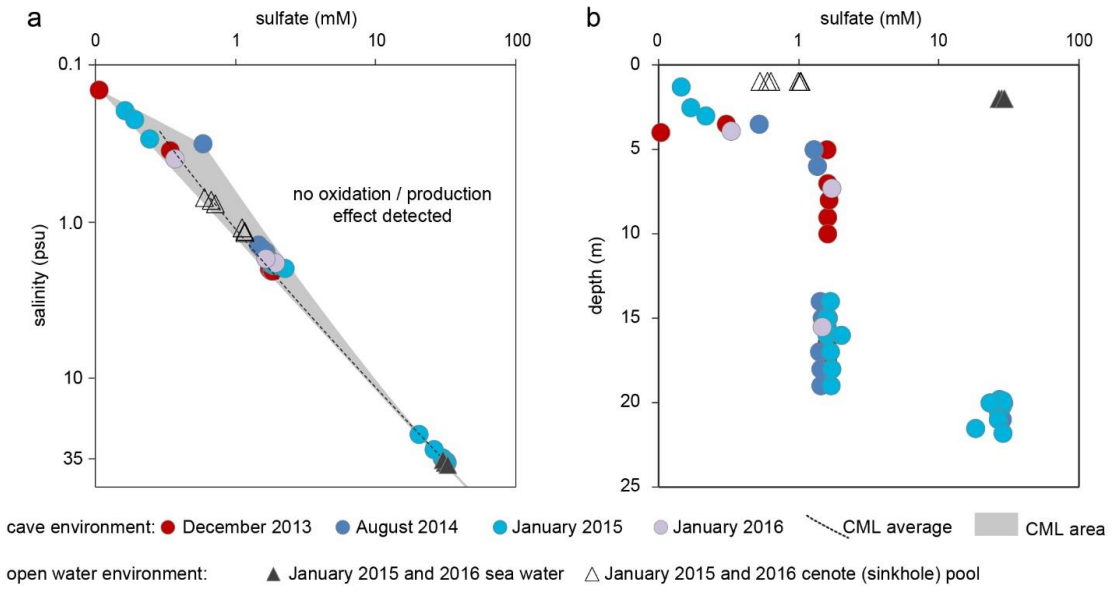

Supplementary Figure: Sulfate concentration at the study site. (a) Salinity versus sulfate. The conservative mixing calculations show no evidence of sulfate oxidation or production within the cave system. (b) Depth profile of sulfate concentrations. The average and total area of conservative mixing lines (CMLs) represent the trend predicted by the mixing model if there was only physical mixing between the meteoric fresh water and saline groundwater endmembers. Production yields an excess of the constituent relative to the CML average and area, while consumption results in depletion. Symbols of individual data points contain the uncertainty (std. dev.) of the measured values.

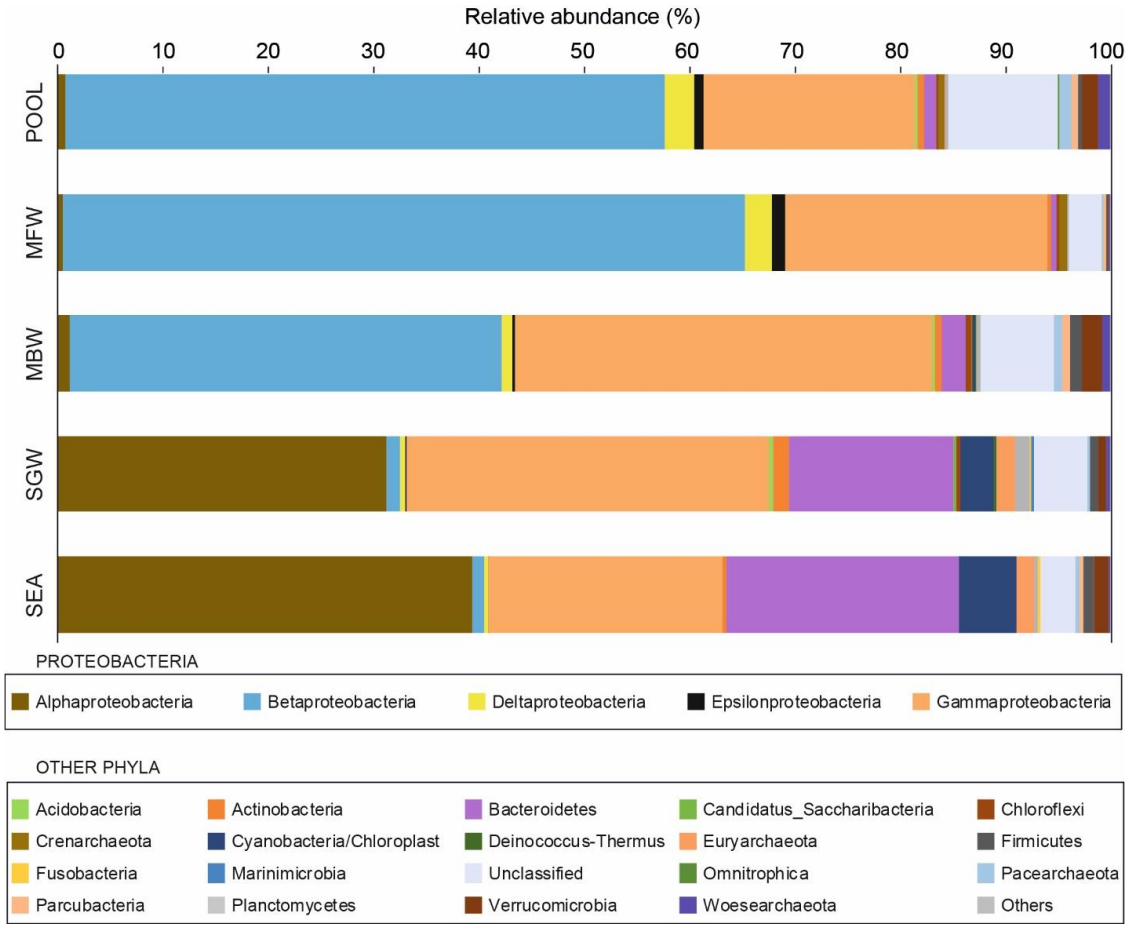

Supplementary Figure: Phylogenetic composition of the microbial community showing the relative abundance of phyla at the five water regimes. Proteobacteria is divided into classes Alpha-, Beta-, Gamma-, Delta- and Epsilonproteobacteria. The graph includes taxa that are grouped under ‘Others’ in Chapter II.

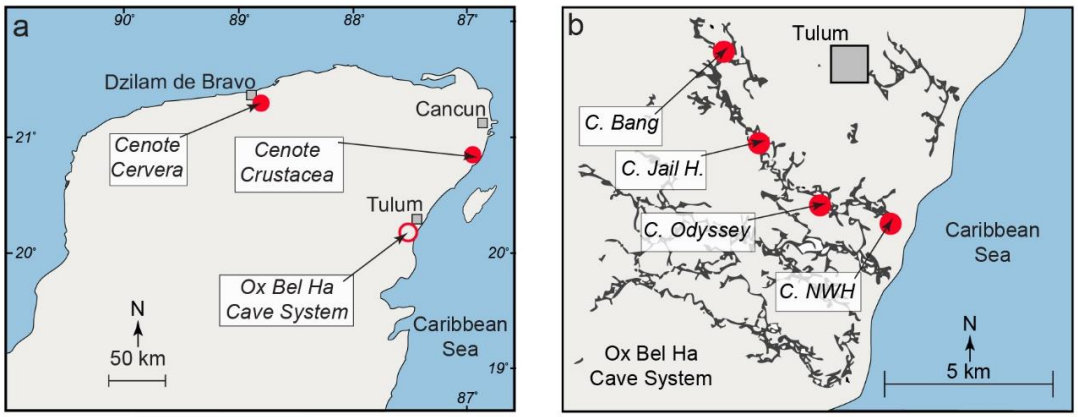

Supplementary Figure: Map of the (a) Yucatan Peninsula and the (b) Ox Bel Ha Cave System showing the sampling locations where *Typhlatya* spp. were collected for this study.

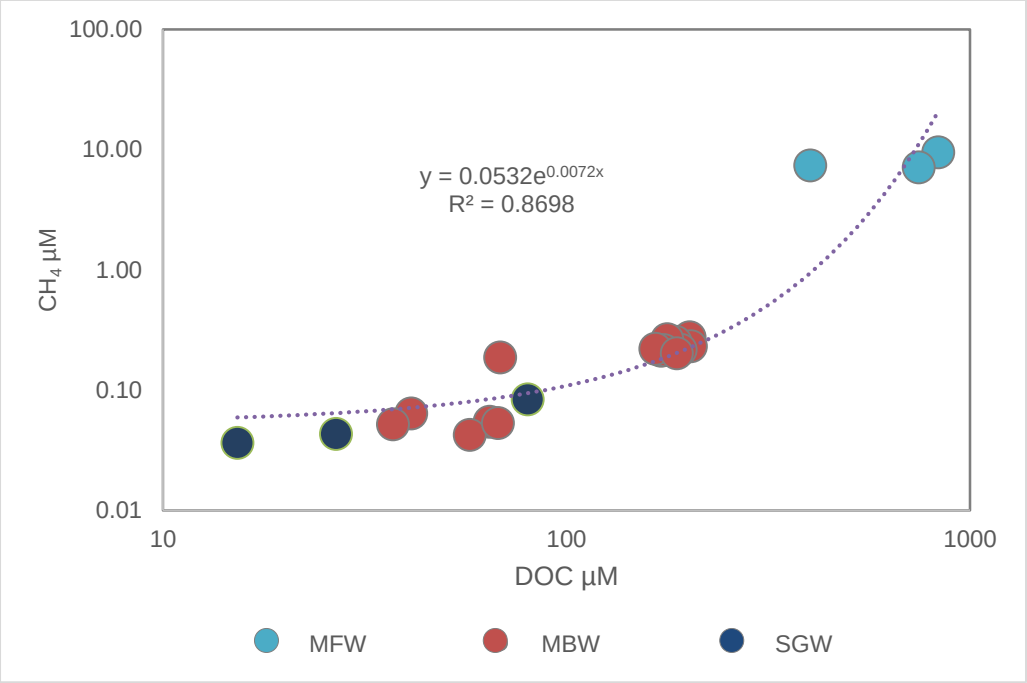

Supplementary Figure: Exponential relationship (dotted line) between methane and DOC concentrations in the water column of the flooded cave passages. Different colors refer to the water regimes (meteoric fresh water = MFW, meteoric brackish water = MBW, and saline groundwater = SGW).

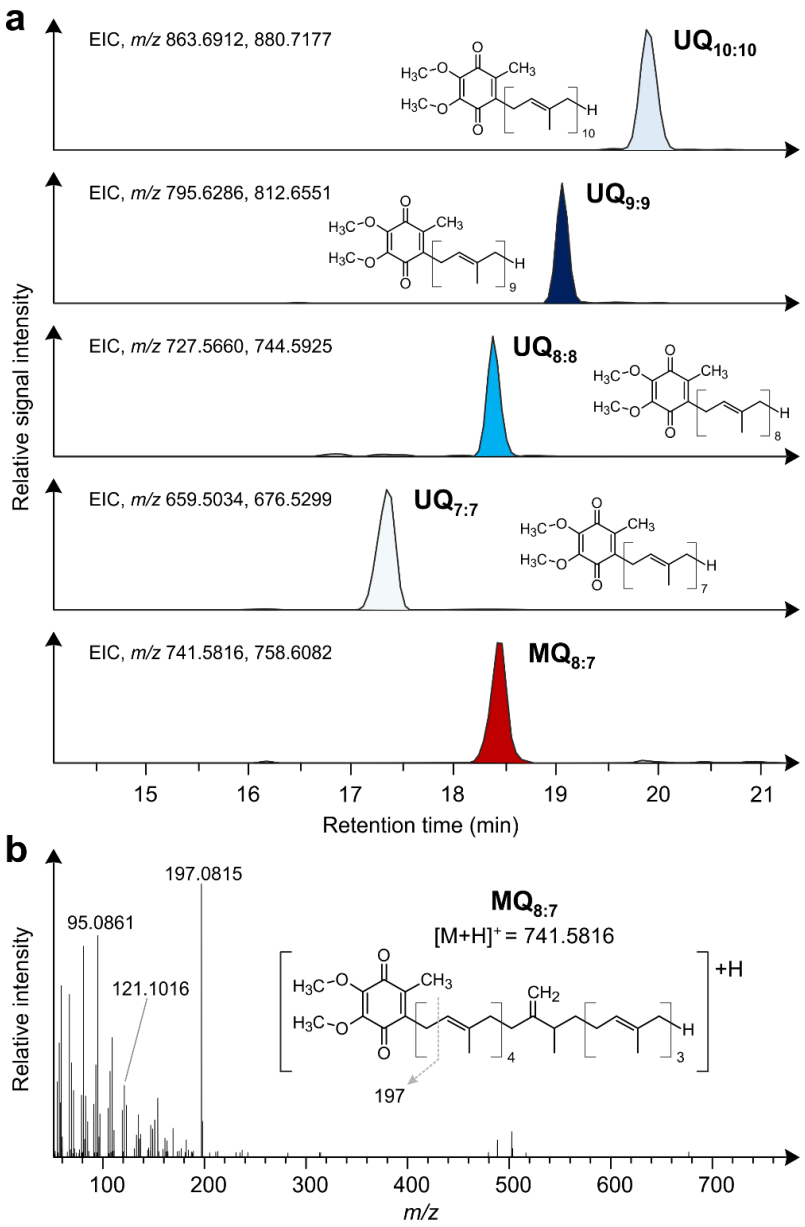

Supplementary Figure: Identification of quinones in sample ‘P07 LIP’. (a) Extracted ion chromatograms (EICs) of all identified quinones including molecular structures of ubiquinones (UQ). (b) Product ion (MS^2) spectra for methylene-ubiquinone ($MQ_{8:7}$, $[M+H]^+$ ion at *m/z* 741.6).

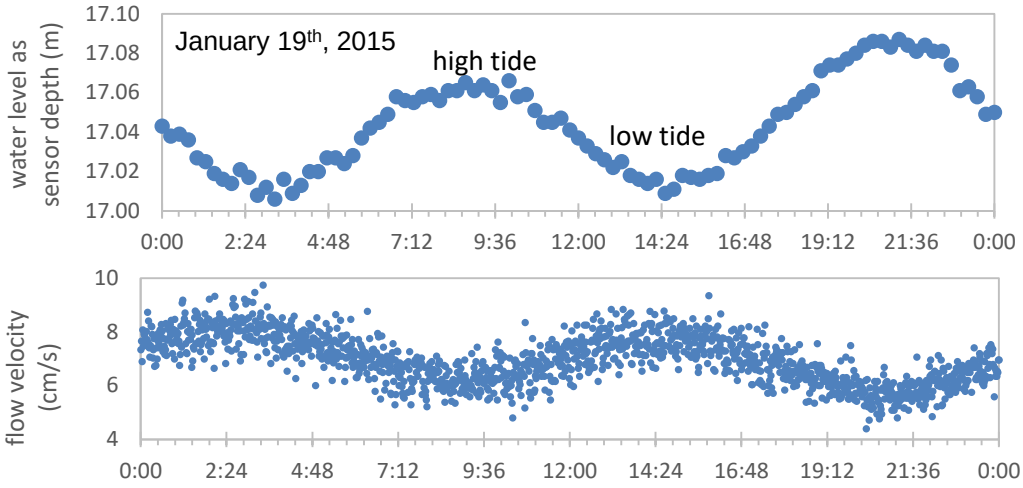

Supplementary Figure: Tidal fluctuation as measured in the meteoric brackish water (MBW) at the study site approximately 8 km from the coastline.

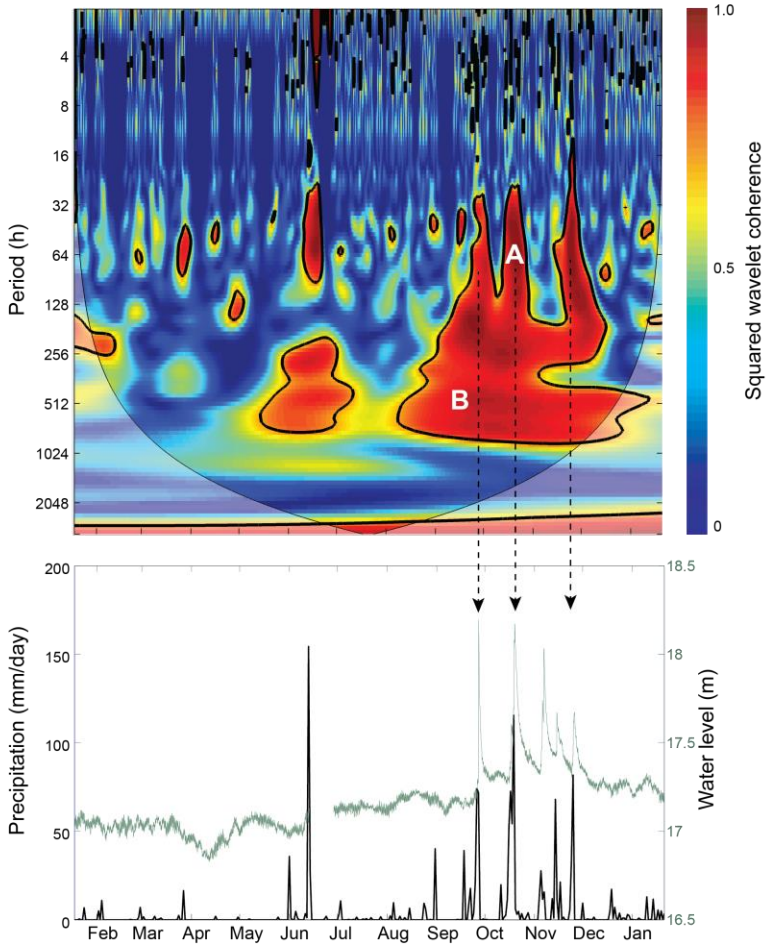

Supplementary Figure: Wavelet coherence between precipitation and water level (upper), and time-series of precipitation and water level (lower). Elevated coherence occurs during episodic precipitation events (arrows), with peak coherence varying with each event. For example, the Oct 22 rainfall event (A) had the highest coherence with water level at periods of approximately 40-75 h, with a phase lag averaging about 18 h (precipitation leading water level). This indicates that the highest coherence in power between the two time-series is on the order of 2-3 d, with a lag of <1 d. The high-precipitation period between Oct-Dec leads to high coherence on the ~512 h (21 d) timescale (B), likely due to the frequency of precipitation events.

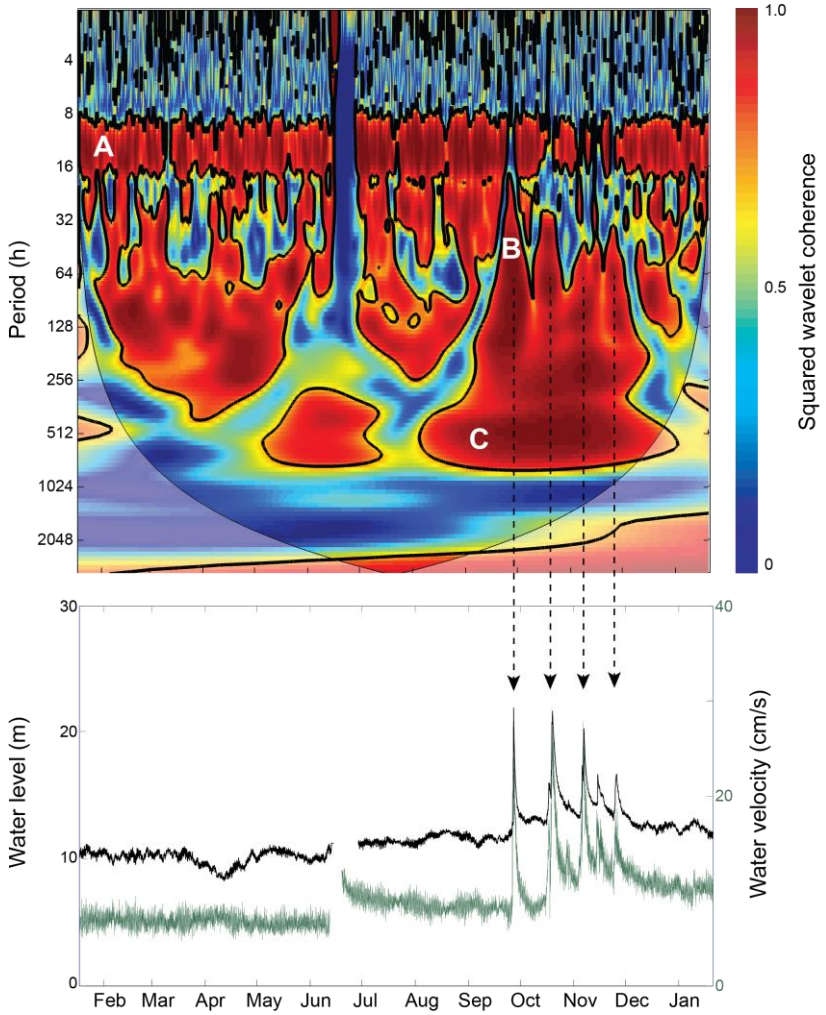

Supplementary Figure: Wavelet coherence between water level and water velocity (upper), and time-series of water level and water velocity (lower). Elevated coherence expectedly occurs on the tidal timescale of ~12.42 h (A), with elevated coherence also during episodic events (arrows). The high-precipitation period between Oct-Dec leads to high coherence at subtidal timescales ~48-168 h (2-7 d; B), as well as longer-term coherence on the ~512 h (21 d) timescale (C), likely due to the frequency of precipitation events. Coherence on the tidal timescale demonstrates a lag of approximately 5 h between water level and velocity.

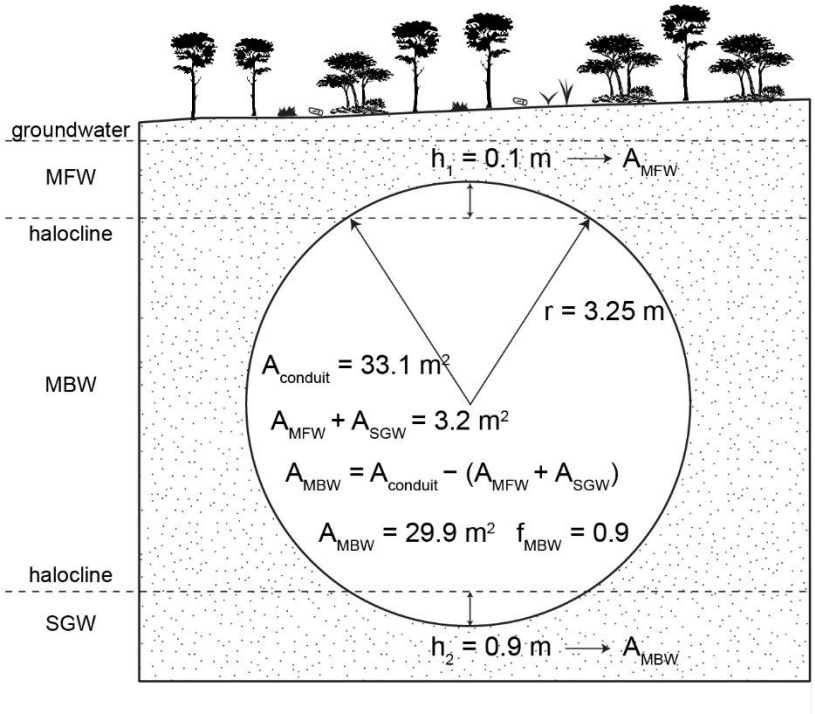

Supplementary Figure: Calculation of the cross-sectional area of the MBW (A_{MBW}) based on averaged passage characteristics. $A_{conduit}$ is the full cross-sectional area of the passage. A_{MFW} and A_{SGW} are the average area within the cross-sectional passage that are filled out by the MFW and SGW, respectively. These components were calculated based on the known position of the haloclines in the system. The radius (r) was calculated based on average conduit dimensions.

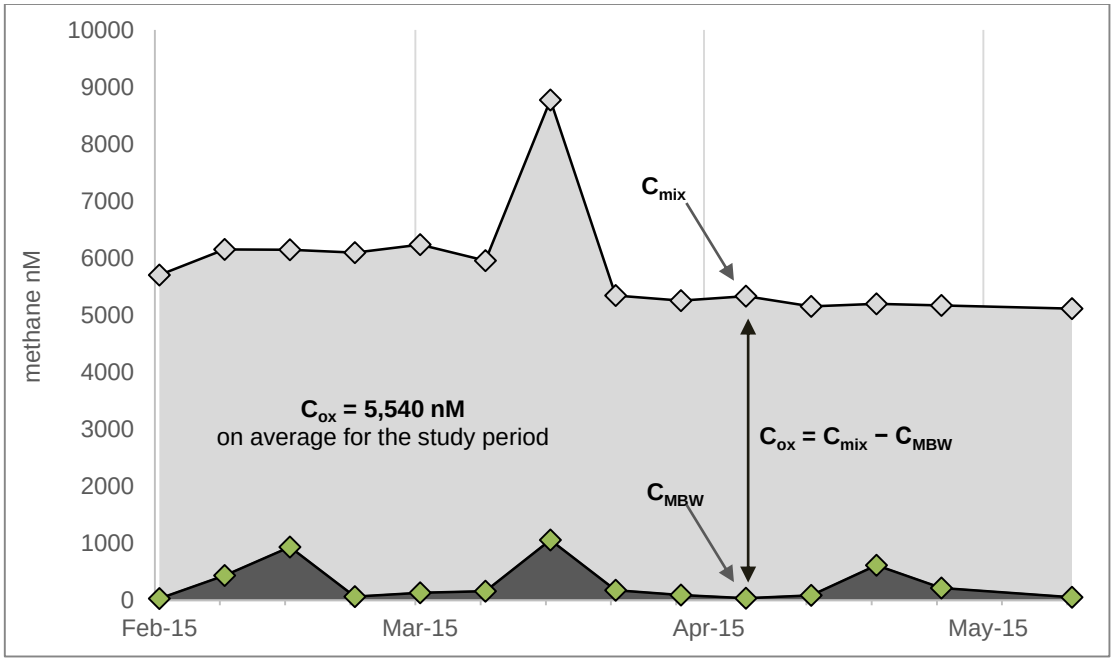

Supplementary Figure: Calculation of the amount of methane oxidized for the study period in a weekly resolution. C_{mix} is the expected methane concentration in the MBW if there was only physical mixing between water masses, based on the conservative mixing model. C_{MBW} is the methane concentration actually measured in MBW. C_{ox} is the amount of methane removed by oxidation, which is calculated to be 5,540 nmol l^{-1} (or 89 mg m^{-3}) indicating that, on average, 91% of source methane concentration is oxidized. The study period is 2/12/2015 to 5/31/2015.

Supplementary Table: Total precipitation prior to YSI sonde deployment at the four sampling events based on data obtained from the closest available weather station (Cozumel International Airport). Weather database retrieved from https://www.wunderground.com/history/airport/MMCZ on January 7th, 2017.

sampling event	YSI sonde deployment	total precipitation (mm) 15 days prior	total precipitation (mm) 30 days prior
2013 December	December 5, 2013	457	906
2014 August	August 16, 2014	52	194
2015 January	January 13, 2015	39	133
2016 January	January 23, 2016	253	443

Supplementary Table: Summary of dissolved constituents for each sampling event. Values of constituents, presented as average ± std. error (n), from the different regimes of the groundwater system and the adjacent coastal sea. Water masses are MFW = meteoric fresh water; MBW = meteoric brackish water; SGW = saline groundwater; POOL = sinkhole pool; SEA = coastal sea water.

2013, December					
	MFW	**MBW**	**SGW**	**POOL**	**SEA**
Salinity psu	0.25 (2)	1.98 ± 0.03 (9)	33.00 (1)	-	-
$[SO_4^{2-}]$ mM	0.20 (2)	1.59 ± 0.01 (9)	26.84 (1)	-	-
$[CH_4]$ nM	8323 (2)	233 ± 9 (9)	84 (1)	-	-
$\delta^{13}C\text{-}CH_4$ ‰	−66.6 (2)	−40.7 ± 0.5 (8)	−51.2 (1)	-	-
[DOC] µM	791 (2)	185 ± 4 (9)	80 (1)	-	-
$\delta^{13}C$-DOC ‰	−27.9 (2)	−27.8 ± 0.1 (9)	−27.2 (1)	-	-
[DIC] mM	4.5 (2)	6.9 ± 0.1 (9)	2.2 (1)	-	-
$\delta^{13}C$-DIC ‰	−18.6 (2)	−12.7 ± 1.7 (9)	−0.1 (1)	-	-
2014, August					
	MFW	**MBW**	**SGW**	**POOL**	**SEA**
Salinity psu	0.26 (2)	1.52 ± 0.02 (7)	34.73 (2)	-	-
$[SO_4^{2-}]$ mM	0.52 (1)	1.40 ± 0.02 (7)	28.53 (2)	-	-
$[CH_4]$ nM	7513 (2)	76 ± 23 (6)	40 (2)	-	-
$\delta^{13}C\text{-}CH_4$ ‰	−65.4 (1)	−55.5 ± 1.5 (6)	−52.9 (2)	-	-
[DOC] µM	402 (1)	62 ± 7 (7)	21 (2)	-	-
$\delta^{13}C$-DOC‰	−28.2 (1)	−29.0 ± 0.5 (7)	−26.4 (2)	-	-
[DIC] mM	4.8 (1)	7.2 ± 0.6 (6)	2.2 (1)	-	-
$\delta^{13}C$-DIC ‰	−15.6 (2)	−8.8 ± 0.6 (7)	−2.3 (2)	-	-
2015, January					
	MFW	**MBW**	**SGW**	**POOL**	**SEA**
Salinity psu	0.24 ± 0.03 (3)	1.88 ± 0.02 (9)	31.99 ± 1.46 (8)	0.73 ± 0.02 (3)	35.12 ± 0.78 (3)
$[SO_4^{2-}]$ mM	0.18 ± 0.02 (3)	1.68 ± 0.04 (9)	25.84 ± 1.26 (8)	0.59 ± 0.03 (3)	28.13 ± 0.68 (3)
$[CH_4]$ nM	5501 ± 411 (3)	137 ± 23 (9)	108 ± 16 (7)	168 ± 47 (3)	157 ± 44 (3)
$\delta^{13}C\text{-}CH_4$ ‰	−65.4 ± 1.2 (3)	−59.2 ± 1.3 (8)	−56.1 ± 1.8 (6)	−40.1 ± 3.3 (3)	−60.8 ± 1.9 (3)
[DOC] µM	-	-	-	-	-
$\delta^{13}C$-DOC‰	-	-	-	-	-
[DIC] mM	4.2 ± 0.1 (3)	7.2 ± 0.2 (9)	2.4 ± 0.3 (8)	5.3 ± 0.2 (3)	2.0 ± 0.1 (3)
$\delta^{13}C$-DIC ‰	−15.5 ± 0.2 (3)	−11.2 ± 0.7 (9)	−8.0 ± 0.4 (8)	−9.4 ± 2.1 (3)	−4.3 (2)

2016, January					
	MFW	**MBW**	**SGW**	**POOL**	**SEA**
Salinity psu	0.40 (1)	1.76 ± 0.03 (4)	34.49 (2)	1.14 ± 0.02 (3)	35.78 ± 0.21 (3)
$[SO_4^{2-}]$ mM	0.33 (1)	1.59 (2)	-	1.02 ± 0.01 (3)	29.28 (1)
$[CH_4]$ nM	3551 (1)	158 ± 63 (4)	203 (2)	821 ± 35 (3)	85 ± 25 (3)
$\delta^{13}C\text{-}CH_4$ ‰	−69.2 (1)	−62.0 ± 4.2 (3)	−63.0 (2)	−61.0 ± 0.2 (3)	−56.2 (2)
[DOC] µM	-	-	-	-	-
$\delta^{13}C$-DOC‰	-		-	-	-
[DIC] mM	-	-	-	-	-
$\delta^{13}C$-DIC ‰	-	-	-	-	-

Supplementary Table: Summary of particulate organic carbon (POC) sampling events. Values, presented as measured value (n) or average (n), from the different regimes of the groundwater system and the adjacent coastal sea.

2015, June					
	MFW	**MBW**	**SGW**	**POOL**	**SEA**
POC µM	3.3 (1)	0.7 (1)	1.2 (1)	19.0 (2)	5.8 (1)
δ^{13}C-POC‰	−29.4 (1)	−26.21 (1)	−25.04 (1)	−28.28 (2)	−20.12 (1)

2016, January					
	MFW	**MBW**	**SGW**	**POOL**	**SEA**
POC µM	14.6 (2)	7.2 (2)	4.0 (2)	58.7 (1)	-
δ^{13}C-POC‰	−28.0 (2)	−28.3 (2)	−28.2 (2)	−27.4 (1)	-

Supplementary Table: Full suite of fatty acid (FA) compounds extracted from the tissue of two *Typhlatya* shrimp specimens shown in Chapter II.

Bulk $\delta^{13}C$ of shrimp specimen = −29.3‰		
FA compound	**Relative abundance**	**$\delta^{13}C$ of FA compound**
$C_{14:0}$	3.6%	−31.56‰
10Me$C_{14:0}$	-	-
***i*$C_{15:0}$**	10.0%	−29.07‰
***ai*$C_{15:0}$**	4.0%	−29.29‰
$C_{15:0}$	2.0%	−29.57‰
14Me-$C_{15:0}$	4.2%	−29.58‰
$C_{16:1\omega9}$	1.9%	−29.95‰
$C_{16:1\omega7c}$	7.5%	−36.84‰
$C_{16:1\omega5c\&t}$	4.4%	−32.26‰
$C_{16:0}$	23.6%	−30.49‰
10Me-$C_{16:0}$	3.2%	−29.16‰
9Me$C_{16:0}$	-	-
8Me$C_{16:0}$	-	-
***i*$C_{17:0}$**	3.5%	−29.71‰
$_{ai}$C17:0	3.1%	−29.02‰
***cy*$C_{17:0\omega5,6}$**	1.3%	−32.05‰
$C_{17:0}$	1.7%	−30.30‰
$C_{18:2}$	1.3%	−33.17‰
$C_{18:1\omega9}$	10.2%	−29.68‰
$C_{18:1\omega7c}$	6.9%	−32.48‰
$C_{18:1\omega5}$	0.9%	−29.30‰
$C_{18:0}$	6.9%	−29.13‰

Bulk $\delta^{13}C$ of shrimp specimen = −49.1‰		
FA compound	**Relative abundance**	**$\delta^{13}C$ of FA compound**
$C_{14:0}$	3.0%	−54.69‰
10Me$C_{14:0}$	3.0%	−67.01‰
i$C_{15:0}$	1.0%	−42.00‰
ai$C_{15:0}$	1.2%	−45.56‰
$C_{15:0}$	0.9%	−47.06‰
14Me-$C_{15:0}$	0.9%	−49.03‰
$C_{16:1\omega9}$	-	-
$C_{16:1\omega7c}$	20.0%	−54.12‰
$C_{16:1\omega5c\&t}$	1.7%	−51.58‰
$C_{16:0}$	28.8%	−51.58‰
10Me-$C_{16:0}$	2.2%	−55.06‰
9Me$C_{16:0}$	0.7%	−54.78‰
8Me$C_{16:0}$	0.6%	−58.35‰
i$C_{17:0}$	0.8%	−52.70‰
$_{ai}$C17:0	1.3%	−44.67‰
cy$C_{17:0\omega5,6}$	0.8%	−49.49‰
$C_{17:0}$	0.8%	−52.79‰
$C_{18:2}$	-	-
$C_{18:1\omega9}$	17.6%	−52.48‰
$C_{18:1\omega7c}$	8.3%	−50.78‰
$C_{18:1\omega5}$	0.7%	−48.22‰
$C_{18:0}$	5.6%	−48.60‰

Supplementary Table: Collected specimens (*Typhlatya* spp.), listed with the sampling site and type of water mass where the specimens were found, as well as their bulk δD and $\delta^{13}C$ values. Calculated percent CH_4-derived carbon in the biomass of the individual shrimp is also reported.

sample ID	sampling site	δD ‰ ± std.dev.		$\delta^{13}C$ ‰ ± std.dev.		water mass	% CH_4-derived carbon
CB-02	Cenote Bang	-		−29.27	± 0.14	MBW	3%
CB-04	Cenote Bang	-		−49.13	± 0.11	MBW	55%
CB-05	Cenote Bang	−152.35	± 1.60	− 38.56	± 0.05	MBW	28%
CB-06	Cenote Bang	−134.01	± 1.60	− 36.68	± 0.05	MBW	23%
CB-07	Cenote Bang	−124.97	± 1.60	− 31.82	± 0.05	MBW	10%
CB-08	Cenote Bang	−192.95	± 1.60	− 43.65	± 0.05	MBW	41%
CB-09	Cenote Bang	−141.03	± 1.60	− 32.80	± 0.05	MBW	13%
CB-10	Cenote Bang	−150.49	± 1.60	− 31.74	± 0.05	MBW	10%
CB-11	Cenote Bang	−95.73	± 1.60	− 34.99	± 0.05	MBW	18%
CB-12	Cenote Bang	−146.68	± 1.60	− 35.01	± 0.05	MBW	18%
CB-13	Cenote Bang	−114.44	± 1.60	− 29.35	± 0.05	MBW	4%
CB-14	Cenote Bang	−98.75	± 1.60	− 30.52	± 0.05	MBW	7%
JH-02	Cenote Jail House	−147.67	± 1.90	− 26.94	± 0.36	MBW	0%
JH-03	Cenote Jail House	−119.51	± 1.90	− 33.32	± 0.36	MBW	14%
CO-02	Cenote Odyssey	−180.38	± 1.90	− 22.52	± 0.36	SGW	0%
TA-01	Cenote N.W.H.	−195.02	± 1.90	− 33.33	± 0.36	MBW	14%
TA-02	Cenote N.W.H.	−158.11	± 1.90	− 34.28	± 0.36	MBW	16%
TA-04	Cenote N.W.H.	−197.17	± 1.90	− 44.99	± 0.36	MBW	44%
CC-06	Cenote Crustacea	−150.08	± 1.90	− 32.78	± 0.36	MBW	12%
CC-07	Cenote Crustacea	−219.22	± 1.90	− 41.39	± 0.36	SGW	35%
CC-08	Cenote Crustacea	−171.24	± 1.90	− 41.39	± 0.36	MBW	35%
CC-09	Cenote Crustacea	−215.93	± 1.90	− 45.30	± 0.36	SGW	45%
CC-10	Cenote Crustacea	−223.64	± 1.90	− 42.29	± 0.36	SGW	37%
CC-11	Cenote Crustacea	−185.37	± 1.90	− 38.45	± 0.36	MBW	27%
CC-12	Cenote Crustacea	−164.71	± 1.90	−32.92	± 0.36	SGW	13%
CC-16	Cenote Crustacea	−205.29	± 1.90	−37.51	± 0.36	MBW	25%
DZ-01	Cenote Cervera	−189.12	± 1.90	−42.96	± 0.10	SGW	39%
Mean value ± std. error:		**−162.96**	**± 7.38**	**−36.07**	**± 1.21**	**-**	**21%**

Supplementary Table: Water samples collected manually with 60 ml syringes were processed in the field within 8 hours after collection. Processing included dividing each sample into subsamples in the order shown above (left to right). *Filter used was a 0.45 μm Acrodisc® inorganic membrane syringe filter.

PROCESSING WATER SAMPLES COLLECTED WITH 60 ML SYRINGES

subsample analysis	CH_4 conc. & $\delta^{13}C$-CH_4	DIC conc.	$\delta^{13}C$-DIC	ions	DOC conc. & $\delta^{13}C$-DOC
order processed in the field lab	1	2	3	4	5
vial volume	30 ml	5 ml	2 ml	1.5 ml	8 ml
vial type	glass serum	glass serum	glass serum	plastic	glass
vial cleaning	baked 450 °C / 4 h	baked 450 °C / 4 h	baked 450 °C / 4 h	milli-Q rinse	baked 450 °C / 4 h
septa / cap	butyl rubber	Teflon	Teflon	plastic	Teflon
septa / cap cleaning	milli-Q rinse	-	-	milli-Q rinse	acid wash
subsample volume	~20 ml	3 ml	>1.5 ml	>1 ml	>6 ml
filter used*	no	no	yes	yes	yes
field storage	fridge	freezer	freezer	fridge	freezer
transportation	cool	blue ice	blue ice	cool	dry ice
storage temp.	<7 °C	−20 °C	−20 °C	<7 °C	−20 °C
analytical method	GC & GC-IRMS	Coulometer	GC-IRMS	IC	HTC-IRMS

Supplementary Table: Details of the samples used in the study. Analyses Performed included IC = Ion Chromatography; DIC = Coulometry; CH_4 = Gas Chromatography; $\delta^{13}C$-CH_4 = Gas-Chromatography-Isotope Ratio Mass Spectrometry (GC-IRMS); $\delta^{13}C$ -DIC = GC-IRMS; $\delta^{13}C$ -DOC = High Temperature Catalytic Oxidation (HTCO)-IRMS; CSIA = Compound-specific $\delta^{13}C$ isotopic analysis of fatty acids; Quinone = High Performance Liquid Chromatography-Mass Spectrometry; 16S = 16S rRNA gene clone library sequencing.

Sample ID	Type	Date Collected	Sampling Location	Water Mass	Analyses Performed
13	water	Dec-2013	C. Bang	MBW	IC, DIC, CH_4, DOC, $\delta^{13}C$-DIC, $\delta^{13}C$-CH_4, $\delta^{13}C$-DOC
14	water	Dec-2013	C. Bang	MBW	IC, DIC, CH_4, DOC, $\delta^{13}C$-DIC, $\delta^{13}C$-DOC
15	water	Dec-2013	C. Bang	MBW	IC, DIC, CH_4, DOC, $\delta^{13}C$-DIC, $\delta^{13}C$-CH_4, $\delta^{13}C$-DOC
16	water	Dec-2013	C. Bang	MBW	IC, DIC, CH_4, DOC, $\delta^{13}C$-DIC, $\delta^{13}C$-CH_4, $\delta^{13}C$-DOC
17	water	Dec-2013	C. Bang	MFW	IC, DIC, CH_4, DOC, $\delta^{13}C$-DIC, $\delta^{13}C$-CH_4, $\delta^{13}C$-DOC
18	water	Dec-2013	C. Bang	MFW	IC, DIC, CH_4, DOC, $\delta^{13}C$-DIC, $\delta^{13}C$-CH_4, $\delta^{13}C$-DOC
19	water	Dec-2013	C. Bang	MBW	IC, DIC, CH_4, DOC, $\delta^{13}C$-DIC, $\delta^{13}C$-CH_4, $\delta^{13}C$-DOC
20	water	Dec-2013	C. Bang	MBW	IC, DIC, CH_4, DOC, $\delta^{13}C$-DIC, $\delta^{13}C$-CH_4, $\delta^{13}C$-DOC
21	water	Dec-2013	C. Bang	MBW	IC, DIC, CH_4, DOC, $\delta^{13}C$-DIC, $\delta^{13}C$-CH_4, $\delta^{13}C$-DOC
22	water	Dec-2013	C. Bang	MBW	IC, DIC, CH_4, DOC, $\delta^{13}C$-DIC, $\delta^{13}C$-CH_4, $\delta^{13}C$-DOC
23	water	Dec-2013	C. Bang	SGW	IC, DIC, CH_4, DOC, $\delta^{13}C$-DIC, $\delta^{13}C$-CH_4, $\delta^{13}C$-DOC
24	water	Dec-2013	C. Bang	MBW	IC, DIC, CH_4, DOC, $\delta^{13}C$-DIC, $\delta^{13}C$-CH_4, $\delta^{13}C$-DOC
84	water	Aug-2014	C. Bang	MBW	IC, DIC, CH_4, DOC, $\delta^{13}C$-DIC, $\delta^{13}C$-CH_4, $\delta^{13}C$-DOC
85	water	Aug-2014	C. Bang	MBW	IC, DIC, CH_4, DOC, $\delta^{13}C$-DIC, $\delta^{13}C$-CH_4, $\delta^{13}C$-DOC
86	water	Aug-2014	C. Bang	MBW	IC, DIC, CH_4, DOC, $\delta^{13}C$-DIC, $\delta^{13}C$-CH_4, $\delta^{13}C$-DOC
87	water	Aug-2014	C. Bang	MBW	IC, DIC, CH_4, DOC, $\delta^{13}C$-DIC, $\delta^{13}C$-CH_4, $\delta^{13}C$-DOC
88	water	Aug-2014	C. Bang	MBW	IC, CH_4, DOC, $\delta^{13}C$-DIC, $\delta^{13}C$-CH_4, $\delta^{13}C$-DOC
89	water	Aug-2014	C. Bang	SGW	IC, CH_4, DOC, $\delta^{13}C$-DIC, $\delta^{13}C$-CH_4, $\delta^{13}C$-DOC
90	water	Aug-2014	C. Bang	SGW	IC, DIC, CH_4, DOC, $\delta^{13}C$-DIC, $\delta^{13}C$-CH_4, $\delta^{13}C$-DOC
92	water	Aug-2014	C. Bang	MFW	IC, DIC, CH_4, $\delta^{13}C$-DIC
93	water	Aug-2014	C. Bang	MFW	IC, CH_4, DOC, $\delta^{13}C$-DIC, $\delta^{13}C$-CH_4, $\delta^{13}C$-DOC
94	water	Aug-2014	C. Bang	MBW	IC, DIC, DOC, $\delta^{13}C$-DIC, $\delta^{13}C$-CH_4, $\delta^{13}C$-DOC
95	water	Aug-2014	C. Bang	MBW	IC, DIC, CH_4, DOC, $\delta^{13}C$-DIC, $\delta^{13}C$-DOC
127	water	Jan-2015	C. Bang	SGW	IC, DIC, CH_4, $\delta^{13}C$-DIC, $\delta^{13}C$-CH_4
128	water	Jan-2015	C. Bang	SGW	IC, DIC, CH_4, $\delta^{13}C$-DIC, $\delta^{13}C$-CH_4
129	water	Jan-2015	C. Bang	SGW	IC, DIC, CH_4, $\delta^{13}C$-DIC, $\delta^{13}C$-CH_4
130	water	Jan-2015	C. Bang	SGW	IC, DIC, CH_4, $\delta^{13}C$-DIC, $\delta^{13}C$-CH_4
131	water	Jan-2015	C. Bang	SGW	IC, DIC, CH_4, $\delta^{13}C$-DIC, $\delta^{13}C$-CH_4
132	water	Jan-2015	C. Bang	SGW	IC, DIC, CH_4, $\delta^{13}C$-DIC, $\delta^{13}C$-CH_4
133	water	Jan-2015	C. Bang	SGW	IC, DIC, CH_4, $\delta^{13}C$-DIC

Sample ID	Type	Date Collected	Sampling Location	Water Mass	Analyses Performed
134	water	Jan-2015	C. Bang	SGW	IC, DIC, δ^{13}C-DIC
157	water	Jan-2015	C. Bang	MBW	IC, DIC, CH_4, δ^{13}C-DIC, δ^{13}C-CH_4
158	water	Jan-2015	C. Bang	MBW	IC, DIC, CH_4, δ^{13}C-DIC, δ^{13}C-CH_4
159	water	Jan-2015	C. Bang	MFW	IC, DIC, CH_4, δ^{13}C-DIC, δ^{13}C-CH_4
160	water	Jan-2015	C. Bang	MBW	IC, DIC, CH_4, δ^{13}C-DIC, δ^{13}C-CH_4
161	water	Jan-2015	C. Bang	MBW	IC, DIC, CH_4, δ^{13}C-DIC, δ^{13}C-CH_4
162	water	Jan-2015	C. Bang	MBW	IC, DIC, CH_4, δ^{13}C-DIC, δ^{13}C-CH_4
173	water	Jan-2015	C. Bang	MBW	IC, DIC, CH_4, δ^{13}C-DIC, δ^{13}C-CH_4
174	water	Jan-2015	C. Bang	MBW	IC, DIC, CH_4, δ^{13}C-DIC, δ^{13}C-CH_4
175	water	Jan-2015	C. Bang	MBW	IC, DIC, CH_4, δ^{13}C-DIC
180	water	Jan-2015	C. Bang	MFW	IC, DIC, CH_4, δ^{13}C-DIC, δ^{13}C-CH_4
181	water	Jan-2015	C. Bang	MFW	IC, DIC, CH_4, δ^{13}C-DIC, δ^{13}C-CH_4
182	water	Jan-2015	C. Bang	MBW	IC, DIC, CH_4, δ^{13}C-DIC, δ^{13}C-CH_4
124	water	Jan-2015	C. Bang	POOL	IC, DIC, CH_4, δ^{13}C-DIC, δ^{13}C-CH_4
125	water	Jan-2015	C. Bang	POOL	IC, DIC, CH_4, δ^{13}C-DIC, δ^{13}C-CH_4
126	water	Jan-2015	C. Bang	POOL	IC, DIC, CH_4, δ^{13}C-DIC, δ^{13}C-CH_4
183	water	Jan-2015	Coastal sea	SEA	IC, DIC, CH_4, δ^{13}C-DIC, δ^{13}C-CH_4
184	water	Jan-2015	Coastal sea	SEA	IC, DIC, CH_4, δ^{13}C-CH_4
185	water	Jan-2015	Coastal sea	SEA	IC, DIC, CH_4, δ^{13}C-DIC, δ^{13}C-CH_4
P-01	water filtrate	Jun-2015	C. Bang	MFW	δ^{13}C-POC
P-02	water filtrate	Jun-2015	C. Bang	SGW	δ^{13}C-POC
P-03	water filtrate	Jun-2015	C. Bang	MBW	δ^{13}C-POC
P-04A	water filtrate	Jun-2015	C. Bang	POOL	δ^{13}C-POC
P-04B	water filtrate	Jun-2015	C. Bang	POOL	δ^{13}C-POC
P-05	water filtrate	Jun-2015	Coastal sea	SEA	δ^{13}C-POC
P06-POM	water filtrate	Jan-2016	C. Bang	MFW	δ^{13}C-POC
P08-POM	water filtrate	Jan-2016	C. Bang	MFW	δ^{13}C-POC
P09-POM	water filtrate	Jan-2016	Coastal sea	SEA	δ^{13}C-POC
P10-POM	water filtrate	Jan-2016	C. Bang	POOL	δ^{13}C-POC
P11-POM	water filtrate	Jan-2016	C. Bang	MBW	δ^{13}C-POC
P12-POM	water filtrate	Jan-2016	C. Bang	SGW	δ^{13}C-POC
P13-POM	water filtrate	Jan-2016	C. Bang	MBW	δ^{13}C-POC
P14-POM	water filtrate	Jan-2016	C. Bang	SGW	δ^{13}C-POC
P09A-LIP	water filtrate	Jan-2016	Coastal sea	SEA	Quinone
P09B-LIP	water filtrate	Jan-2016	Coastal sea	SEA	Quinone
P09C-LIP	water filtrate	Jan-2016	Coastal sea	SEA	Quinone
12-M-LIP	water filtrate	Jan-2016	C. Bang	POOL	Quinone
6-M-LIP	water filtrate	Jan-2016	C. Bang	POOL	Quinone
7-M-LIP	water filtrate	Jan-2016	C. Bang	POOL	Quinone
P10-LIP	water filtrate	Jan-2016	C. Bang	POOL	Quinone
P07-LIP	water filtrate	Jan-2016	C. Bang	POOL	Quinone

Sample ID	Type	Date Collected	Sampling Location	Water Mass	Analyses Performed
P11-LIP	water filtrate	Jan-2016	C. Bang	MBW	Quinone
P13-LIP	water filtrate	Jan-2016	C. Bang	MBW	Quinone
10-M-LIP	water filtrate	Jan-2016	C. Bang	MFW	Quinone
5-M-LIP	water filtrate	Jan-2016	C. Bang	MFW	Quinone
8-M-LIP	water filtrate	Jan-2016	C. Bang	MFW	Quinone
9-M-LIP	water filtrate	Jan-2016	C. Bang	MFW	Quinone
P-06-LIP	water filtrate	Jan-2016	C. Bang	MFW	Quinone
P-08-LIP	water filtrate	Jan-2016	C. Bang	MFW	Quinone
P-12-LIP	water filtrate	Jan-2016	C. Bang	SGW	Quinone
P-14-LIP	water filtrate	Jan-2016	C. Bang	SGW	Quinone
M-01	water filtrate	Jan-2016	Coastal sea	SEA	16S
M-02	water filtrate	Jan-2016	Coastal sea	SEA	16S
M-03	water filtrate	Jan-2016	Coastal sea	SEA	16S
P-07	water filtrate	Jan-2016	C. Bang	POOL	16S
M-05	water filtrate	Jan-2016	C. Bang	POOL	16S
M-10	water filtrate	Jan-2016	C. Bang	POOL	16S
M-11	water filtrate	Jan-2016	C. Bang	POOL	16S
M-12	water filtrate	Jan-2016	C. Bang	MFW	16S
M-13	water filtrate	Jan-2016	C. Bang	MFW	16S
M-14	water filtrate	Jan-2016	C. Bang	MFW	16S
M-16	water filtrate	Jan-2016	C. Bang	MFW	16S
M-17	water filtrate	Jan-2016	C. Bang	SGW	16S
M-21	water filtrate	Jan-2016	C. Bang	SGW	16S
M-04	water filtrate	Jan-2016	C. Bang	MBW	16S
M-07	water filtrate	Jan-2016	C. Bang	MBW	16S
M-09	water filtrate	Jan-2016	C. Bang	MBW	16S
CB-02	shrimp	Feb-2013	C. Bang	MBW	CSIA and bulk δ13C
CB-04	shrimp	Aug-2013	C. Bang	MBW	CSIA and bulk δ13C
CB-05	shrimp	Jun-2014	C. Bang	MBW	bulk $\delta^{13}C$ and δD
CB-06	shrimp	Jun-2014	C. Bang	MBW	bulk $\delta^{13}C$ and δD
CB-07	shrimp	Jun-2014	C. Bang	MBW	bulk $\delta^{13}C$ and δD
CB-08	shrimp	Jun-2014	C. Bang	MBW	bulk $\delta^{13}C$ and δD
CB-09	shrimp	Jun-2014	C. Bang	MBW	bulk $\delta^{13}C$ and δD
CB-10	shrimp	Jun-2014	C. Bang	MBW	bulk $\delta^{13}C$ and δD
CB-11	shrimp	Jun-2014	C. Bang	MBW	bulk $\delta^{13}C$ and δD
CB-12	shrimp	Jun-2014	C. Bang	MBW	bulk $\delta^{13}C$ and δD
CB-13	shrimp	Jun-2014	C. Bang	MBW	bulk $\delta^{13}C$ and δD
CB-14	shrimp	Jun-2014	C. Bang	MBW	bulk $\delta^{13}C$ and δD
JH-02	shrimp	Jul-2013	C. Jailhouse	MBW	bulk $\delta^{13}C$ and δD
JH-03	shrimp	Jul-2013	C. Jailhouse	MBW	bulk $\delta^{13}C$ and δD
CO-02	shrimp	Aug-2013	C. Odyssey	SGW	bulk $\delta^{13}C$ and δD

Sample ID	Type	Date Collected	Sampling Location	Water Mass	Analyses Performed
TA-01	shrimp	Aug-2013	C. N.W.H.	MBW	bulk $\delta^{13}C$ and δD
TA-02	shrimp	Aug-2013	C. N.W.H.	MBW	bulk $\delta^{13}C$ and δD
TA-03	shrimp	Aug-2013	C. N.W.H.	MBW	bulk $\delta^{13}C$ and δD
TA-04	shrimp	Aug-2013	C. N.W.H.	MBW	bulk $\delta^{13}C$ and δD
DZ-01	shrimp	Dec-2013	C. Cervera	SGW	bulk $\delta^{13}C$ and δD
CC-06	shrimp	Jul-2013	C. Crustacea	MBW	bulk $\delta^{13}C$ and δD
CC-07	shrimp	Jul-2013	C. Crustacea	SGW	bulk $\delta^{13}C$ and δD
CC-08	shrimp	Jul-2013	C. Crustacea	MBW	bulk $\delta^{13}C$ and δD
CC-09	shrimp	Jul-2013	C. Crustacea	SGW	bulk $\delta^{13}C$ and δD
CC-10	shrimp	Jul-2013	C. Crustacea	SGW	bulk $\delta^{13}C$ and δD
CC-11	shrimp	Jul-2013	C. Crustacea	MBW	bulk $\delta^{13}C$ and δD
CC-12	shrimp	Jul-2013	C. Crustacea	SGW	bulk $\delta^{13}C$ and δD
CC-13	shrimp	Jul-2013	C. Crustacea	SGW	bulk $\delta^{13}C$ and δD
CC-14	shrimp	Jul-2013	C. Crustacea	MBW	bulk $\delta^{13}C$ and δD
CC-16	shrimp	Jul-2013	C. Crustacea	SGW	bulk $\delta^{13}C$ and δD
CBSF-01	insect	Jun-2015	near C. Bang	SOIL	bulk $\delta^{13}C$ and δD
CBSF-02	insect	Jun-2015	near C. Bang	SOIL	bulk $\delta^{13}C$ and δD
CBSF-03	insect	Jun-2015	near C. Bang	SOIL	bulk $\delta^{13}C$ and δD
CBSF-04	insect	Jun-2015	near C. Bang	SOIL	bulk $\delta^{13}C$ and δD
SO-01	soil	Jun-2015	near C. Bang	SOIL	bulk $\delta^{13}C$
SO-02	soil	Jun-2015	near C. Bang	SOIL	bulk $\delta^{13}C$
SO-03	soil	Jun-2015	near C. Bang	SOIL	bulk $\delta^{13}C$ and δD

Supplementary Table: All observed phylogenetic affiliations based on sequence reads from 16S rRNA gene sequences. Number of sequencing reads were assigned to OTUs using RDP reference database at 97% sequence identity. Percentage of total sequence reads[§] per sample assigned to taxa are shown below. Phy. = Phylum, Cl. = Class, Or. = Order.

	water mass	MFW				MBW			SGW		POOL				SEA		
	sample ID	M16	M14	M13	M12	M9	M7	M4	M21	M17	M11	P07	M5	M10	M3	M2	M1
	[§]sequence reads	10886	13434	10892	14363	7276	3708	3842	5629	4444	12386	9118	15240	13612	3724	7891	8077
Phy.	**Cl.** **Or.** **Family**	**% of sequence reads per sample**															
Acidobacteria		0.00	0.09	0.00	0.00	0.18	0.65	0.00	0.00	0.71	0.00	0.62	0.35	0.00	0.00	0.00	0.00
Actinobacteria																	
	Actinobacteria																
	Actinomycetales	0.79	0.25	0.27	0.14	0.94	0.13	0.08	0.00	2.52	0.50	0.27	0.75	0.00	0.16	0.05	0.05
	Others	0.00	0.00	0.00	0.00	0.00	0.32	0.00	0.39	0.33	0.00	0.00	0.24	0.00	0.00	0.43	0.37
Bacteroidetes																	
	Flavobacteriia																
	Flavobacteriales																
	Flavobacteriaceae	0.06	0.00	0.12	0.00	0.08	0.16	0.00	11.94	0.09	0.00	0.00	0.13	0.02	0.00	13.67	9.46
	Others	0.17	0.04	0.11	0.05	0.31	0.86	0.80	0.20	1.67	0.07	0.75	0.30	0.00	0.72	0.43	0.09
	Sphingobacteriia																
	Sphingobacteriales	0.12	0.05	0.18	0.17	0.12	1.08	0.82	0.00	0.13	0.17	0.83	0.25	0.06	0.53	0.00	0.24
	Others	0.11	0.06	0.00	0.11	0.26	0.67	1.00	13.25	0.00	0.08	1.06	0.27	0.02	0.66	13.75	15.10
	Unclassified	0.12	0.00	0.14	0.02	0.12	0.78	0.67	0.00	0.00	0.00	0.71	0.18	0.00	0.53	0.00	0.00
Chloroflexi																	
	Anaerolineae																
	Anaerolineales																
	Anaerolineaceae	0.00	0.34	0.00	0.00	0.31	1.02	0.00	0.00	0.20	0.25	0.04	0.00	0.19	0.00	0.00	0.00
	Others	0.02	0.25	0.34	0.00	0.03	0.00	0.18	0.00	0.49	0.19	0.13	0.00	0.06	0.00	0.00	0.00

				water mass	MFW				MBW			SGW		POOL				SEA		
				sample ID	M16	M14	M13	M12	M9	M7	M4	M21	M17	M11	P07	M5	M10	M3	M2	M1
				[§]sequence reads	10886	13434	10892	14363	7276	3708	3842	5629	4444	12386	9118	15240	13612	3724	7891	8077
Phy.	**Cl.**	**Or.**	**Family**		**% of sequence reads per sample**															
Cyanobacteria																				
	Chloroplast																			
		Chloroplast																		
			Bacillariophyta		0.00	0.00	0.00	0.00	0.05	0.57	0.00	0.48	0.00	0.02	0.00	0.00	0.00	0.00	1.20	0.97
			Others		0.00	0.00	0.00	0.00	0.00	0.16	0.00	0.25	0.00	0.00	0.00	0.00	0.00	0.00	0.20	0.15
	Cyanobacteria																			
		Chroococcales																		
			GpIIa		0.00	0.00	0.00	0.00	0.00	0.00	0.00	4.67	0.00	0.00	0.12	0.00	0.00	0.00	5.34	5.15
	Others				0.00	0.00	0.00	0.00	0.00	0.22	0.00	0.14	0.00	0.00	0.00	0.00	0.00	0.00	0.19	0.00
Firmicutes																				
	Bacilli																			
		Bacillales																		
			Staphylococcaceae		0.18	0.00	0.00	0.04	0.33	0.00	0.26	0.00	1.81	0.00	0.05	0.00	0.00	0.00	0.00	0.00
		Lactobacillales																		
			Aerococcaceae		0.00	0.00	0.00	0.00	0.00	0.00	0.00	0.00	1.32	0.05	0.00	0.00	0.00	0.00	0.00	0.00
	Others				0.00	0.15	0.24	0.00	0.33	0.00	0.00	0.00	0.09	0.00	0.58	0.38	0.00	0.56	0.33	0.48
Nitrospinae																				
	Nitrospinia																			
		Nitrospinales																		
			Nitrospinaceae		0.00	0.00	0.00	0.00	0.00	0.00	0.00	0.00	0.25	0.00	0.00	0.00	0.00	0.00	0.00	0.00
Nitrospirae																				
	Nitrospira																			
		Nitrospirales																		
			Nitrospiraceae		0.00	0.00	0.19	0.00	0.00	0.75	0.59	0.00	0.11	0.00	0.47	0.00	0.00	0.19	0.00	0.00

				water mass	MFW				MBW			SGW		POOL				SEA		
				sample ID	M16	M14	M13	M12	M9	M7	M4	M21	M17	M11	P07	M5	M10	M3	M2	M1
				[§]sequence reads	10886	13434	10892	14363	7276	3708	3842	5629	4444	12386	9118	15240	13612	3724	7891	8077
Phy.	**Cl.**	**Or.**	**Family**		**% of sequence reads per sample**															
Parcubacteria					0.45	0.10	0.11	0.00	0.57	0.05	1.42	0.00	0.00	0.16	2.26	0.31	0.02	2.26	0.00	0.00
Planctomycetes																				
	Planctomycetia																			
		Planctomycetales			0.19	0.03	0.00	0.06	0.52	0.73	0.77	0.76	0.76	0.00	0.59	0.22	0.04	0.45	1.39	0.69
		Others			0.00	0.02	0.00	0.03	0.29	1.13	0.26	0.00	0.00	0.00	0.60	0.17	0.03	0.00	0.10	0.00
Proteobacteria																				
	Alphaproteobacteria																			
		Caulobacterales																		
			Caulobacteraceae		0.27	0.00	0.00	0.00	0.20	0.00	0.00	0.00	1.05	0.00	0.00	0.25	0.04	0.00	0.00	0.00
			others		0.00	0.00	0.00	0.00	0.00	0.00	0.00	0.00	0.00	0.00	0.00	0.00	0.00	0.00	0.10	0.00
		Kiloniellales																		
			Kiloniellaceae		0.00	0.00	0.00	0.00	0.00	0.00	0.00	2.08	0.00	0.00	0.00	0.00	0.00	0.00	1.98	2.24
		Rhizobiales																		
			Methylocystaceae		0.00	0.31	0.63	0.34	0.00	0.48	0.00	0.00	0.00	0.60	0.00	0.44	0.27	0.00	0.00	0.00
		Rhodobacterales																		
			Rhodobacteraceae		0.00	0.00	0.00	0.00	0.40	0.83	0.00	34.38	1.99	0.00	0.23	0.36	0.00	0.77	30.01	32.83
		Rhodospirillales																		
			Rhodospirillaceae		0.00	0.10	0.17	0.19	0.18	0.27	0.00	11.53	0.29	0.14	0.00	0.13	0.10	0.00	11.70	12.42
			Others		0.00	0.00	0.00	0.00	0.00	0.00	0.05	0.41	0.00	0.05	0.00	0.00	0.00	0.00	0.65	0.78
		SAR11			0.00	0.00	0.00	0.00	0.00	0.00	0.00	0.71	0.00	0.00	0.00	0.00	0.00	0.00	1.10	1.05
		Sphingomonadales																		
			Erythrobacteraceae		0.16	0.00	0.15	0.00	0.15	0.00	0.00	0.00	0.91	0.00	0.00	0.24	0.06	0.00	0.00	0.00
			Others		0.42	0.00	0.00	0.00	0.16	0.00	0.00	0.00	0.47	0.17	0.00	0.40	0.00	0.00	0.00	0.00
		Others			0.40	0.00	0.00	0.00	0.00	0.48	0.67	0.18	1.12	0.00	0.14	0.11	0.02	0.00	0.48	0.30

			water mass	MFW				MBW			SGW		POOL				SEA		
			sample ID	M16	M14	M13	M12	M9	M7	M4	M21	M17	M11	P07	M5	M10	M3	M2	M1
			[§]sequence reads	10886	13434	10892	14363	7276	3708	3842	5629	4444	12386	9118	15240	13612	3724	7891	8077
Phy.	**Cl.**	**Or.**	**Family**	**% of sequence reads per sample**															
	Betaproteobacteria																		
		Burkholderiales																	
			Burkholderiaceae	7.42	1.36	1.40	1.40	31.17	1.27	0.41	0.00	0.11	1.35	0.16	22.25	1.28	0.37	0.19	0.14
			Comamonadaceae	6.46	0.43	1.03	0.62	9.78	9.80	1.11	0.27	0.00	0.67	0.47	9.66	0.84	0.61	0.00	0.24
			Others	1.30	1.65	1.86	2.18	0.41	0.89	0.21	0.00	0.25	2.63	0.17	0.53	2.15	0.00	0.00	0.00
		Gallionellales																	
			Gallionellaceae	1.46	0.28	0.62	0.33	2.33	18.83	0.00	0.00	0.00	0.25	0.00	2.18	0.32	0.00	0.00	0.00
		Hydrogenophilales																	
			Hydrogenophilaceae	0.00	0.33	0.34	0.26	0.00	0.00	0.00	0.00	0.00	0.32	0.00	0.00	0.62	0.00	0.00	0.00
		Methylophilales																	
			Methylophilaceae	0.00	0.15	0.51	0.33	0.00	0.00	0.31	0.00	0.00	0.29	0.12	0.07	0.38	0.00	0.00	0.00
		Neisseriales																	
			Neisseriaceae	2.54	0.00	0.00	0.00	1.25	0.35	0.00	0.34	0.00	0.00	0.11	0.54	0.00	0.37	0.00	0.11
		Nitrosomonadales																	
			Nitrosomonadaceae	0.00	0.00	0.00	0.00	0.00	0.00	0.00	0.00	0.00	0.00	0.00	0.00	0.05	0.00	0.00	0.00
		Rhodocyclales																	
			Rhodocyclaceae	0.39	1.42	2.16	1.38	0.76	0.65	0.49	0.00	0.00	1.02	0.53	1.51	1.66	0.00	0.00	0.00
		Others		7.30	61.30	61.19	57.28	11.79	3.18	4.48	0.00	1.58	60.89	2.74	12.59	63.02	1.41	0.61	0.26
	Deltaproteobacteria																		
		Bdellovibrionales																	
			Bdellovibrionaceae	0.00	0.00	0.00	0.00	0.00	0.00	0.18	0.00	0.29	0.10	0.10	0.00	0.06	0.00	0.00	0.00
			Others	0.11	0.04	0.24	0.07	0.34	0.05	0.41	0.00	0.00	0.36	2.55	0.48	0.15	1.14	0.00	0.00
		Desulfobacterales																	
			Desulfobacteraceae	0.00	0.00	0.00	0.00	0.00	0.00	0.00	0.00	0.00	0.00	0.13	0.05	0.00	0.00	0.00	0.00

			water mass	**MFW**				**MBW**			**SGW**		**POOL**				**SEA**		
			sample ID	M16	M14	M13	M12	M9	M7	M4	M21	M17	M11	P07	M5	M10	M3	M2	M1
			[§]sequence reads	10886	13434	10892	14363	7276	3708	3842	5629	4444	12386	9118	15240	13612	3724	7891	8077
Phy.	**Cl.**	**Or.**	**Family**	**% of sequence reads per sample**														
			Desulfobulbaceae	0.00	0.00	0.00	0.10	0.00	0.00	0.00	0.00	0.00	0.18	0.00	0.00	0.07	0.00	0.15	0.00
		Syntrophobacterales																	
			Syntrophaceae	0.41	1.46	1.93	2.40	0.70	0.51	0.00	0.00	0.00	2.37	0.08	0.83	1.37	0.00	0.00	0.00
			Syntrophobacteraceae	0.00	0.05	0.00	0.00	0.00	0.00	0.00	0.00	0.00	0.04	0.00	0.00	0.03	0.00	0.00	0.00
		Others		0.00	0.91	0.85	0.44	0.11	0.27	0.13	0.18	0.69	0.75	0.48	0.23	0.33	0.11	0.27	0.00
	Epsilonproteobacteria																		
		Campylobacterales																	
			Campylobacteraceae	0.00	0.27	0.50	0.36	0.16	0.00	0.15	0.21	0.00	0.60	0.22	0.12	0.38	0.29	0.00	0.14
			Helicobacteraceae	2.64	4.88	6.29	7.17	3.50	2.18	0.00	0.25	0.25	6.57	0.13	4.93	5.78	0.00	0.08	0.19
		Nautiliales																	
			Nautiliaceae	0.00	1.21	1.34	1.53	0.00	0.00	0.00	0.00	0.00	1.53	0.00	0.00	1.20	0.00	0.00	0.00
		Others		0.04	0.96	0.73	1.05	0.00	0.38	0.00	0.00	0.00	1.13	0.00	0.02	0.62	0.00	0.00	0.00
	Gammaproteobacteria																		
		Alteromonadales																	
			Alteromonadaceae	0.00	0.00	0.00	0.00	0.00	0.00	0.00	0.98	0.27	0.00	0.00	0.00	0.00	0.00	1.23	0.89
			Shewanellaceae	0.40	0.00	0.17	0.23	0.27	0.00	0.33	0.00	0.94	0.00	0.07	0.23	0.00	0.32	0.00	0.00
		Chromatiales																	
			Chromatiaceae	1.91	0.00	0.00	0.28	1.54	0.67	0.33	0.00	0.69	0.00	0.00	0.80	0.27	0.00	0.00	0.00
			Ectothiorhodospiraceae	0.00	0.00	0.00	0.00	0.12	0.00	0.00	0.00	0.00	0.00	0.00	0.00	0.00	0.00	0.00	0.00
			Halothiobacillaceae	0.00	0.59	0.60	0.88	0.00	0.00	0.00	0.00	0.00	1.01	0.00	0.00	0.45	0.00	0.00	0.00
		Methylococcales																	
			Methylococcaceae	0.22	2.89	6.16	4.27	0.26	5.17	0.00	0.00	0.00	5.39	0.00	0.30	6.68	0.00	0.00	0.00
		Oceanospirillales																	
			Halomonadaceae	0.00	0.00	0.00	0.00	0.00	0.00	0.00	0.07	0.00	0.00	0.00	0.00	0.00	0.00	0.09	0.10

				water mass	MFW				MBW			SGW		POOL				SEA		
				sample ID	M16	M14	M13	M12	M9	M7	M4	M21	M17	M11	P07	M5	M10	M3	M2	M1
				[§]sequence reads	10886	13434	10892	14363	7276	3708	3842	5629	4444	12386	9118	15240	13612	3724	7891	8077
Phy.	**Cl.**	**Or.**	**Family**		**% of sequence reads per sample**															
			Litoricolaceae		0.00	0.00	0.00	0.00	0.00	0.00	0.00	4.16	0.00	0.00	0.00	0.00	0.00	0.00	2.89	2.84
		Pseudomonadales																		
			Moraxellaceae		56.04	11.97	4.32	12.60	20.99	36.20	55.78	0.00	52.44	3.31	36.06	23.85	6.01	68.28	0.72	0.84
			Pseudomonadaceae		1.80	0.12	0.39	0.77	0.86	0.48	4.27	0.00	1.79	0.31	0.54	0.81	0.99	0.21	0.00	0.00
		Thiotrichales																		
			Thiotrichaceae		0.18	0.00	0.00	0.00	0.19	1.08	0.00	0.52	0.00	0.00	0.00	0.16	0.00	0.00	0.38	0.24
		Vibrionales																		
			Vibrionaceae		0.00	0.00	0.00	0.00	0.00	0.00	0.00	1.49	0.16	0.00	0.00	0.00	0.00	0.00	1.08	0.77
		Others			0.82	0.14	0.40	0.14	0.40	1.16	0.13	5.76	2.70	0.30	0.03	0.55	0.70	0.00	5.07	5.30
	Unclassified				0.28	0.23	0.32	0.19	0.55	0.27	2.29	0.16	0.74	0.68	3.78	0.82	0.16	1.83	0.35	0.27
Verrucomicrobia					0.38	0.04	0.18	0.00	0.82	2.72	2.70	0.91	0.38	0.00	5.17	1.29	0.03	3.96	0.90	0.67
Others					0.00	0.14	0.09	0.31	0.05	0.43	0.15	0.18	1.76	0.17	0.32	0.33	0.16	0.11	0.35	0.22
Unclassified					3.36	2.68	3.40	1.73	3.83	1.97	16.09	1.05	9.73	4.14	29.71	6.93	2.02	11.59	0.95	1.89
Crenarchaeota																				
	Thermoprotei				0.00	2.03	0.00	0.33	0.23	0.00	0.00	0.00	0.00	0.55	0.00	0.28	0.59	0.00	0.00	0.00
Euryarchaeota																				
	Methanobacteria																			
		Methanobacteriales																		
			Methanobacteriaceae		0.06	0.00	0.00	0.00	0.00	0.00	0.00	0.00	0.00	0.00	0.00	0.00	0.00	0.00	0.00	0.00
	Methanomicrobia																			
		Methanocellales																		
			Methanocellaceae		0.00	0.00	0.00	0.00	0.14	0.00	0.00	0.00	0.00	0.00	0.00	0.07	0.00	0.00	0.00	0.00
		Methanosarcinales																		
			Methanosarcinaceae		0.00	0.00	0.00	0.00	0.07	0.00	0.00	0.00	0.00	0.00	0.00	0.00	0.00	0.00	0.00	0.00

water mass				**MFW**				**MBW**			**SGW**		**POOL**				**SEA**		
sample ID				M16	M14	M13	M12	M9	M7	M4	M21	M17	M11	P07	M5	M10	M3	M2	M1
[$]sequence reads				10886	13434	10892	14363	7276	3708	3842	5629	4444	12386	9118	15240	13612	3724	7891	8077
Phy.	**Cl.**	**Or.**	**Family**	**% of sequence reads per sample**															
			Methanotrichaceae	0.00	0.00	0.00	0.00	0.12	0.00	0.00	0.00	0.00	0.00	0.00	0.13	0.00	0.00	0.00	0.00
	Thermoplasmata																		
		Methanomassiliicoccales																	
			Methanomassiliicoccaceae	0.06	0.25	0.00	0.13	0.00	0.00	0.00	0.00	1.83	0.00	0.00	0.17	0.00	0.00	0.00	0.00
	Others			0.00	0.00	0.00	0.00	0.00	0.00	0.00	0.00	1.43	0.02	0.00	0.00	0.00	0.00	0.00	0.20
	Unclassified			0.04	0.04	0.00	0.05	0.03	0.00	0.00	1.99	0.00	0.08	0.00	0.14	0.23	0.00	1.48	2.28
Pacearchaeota				0.32	0.10	0.17	0.00	0.86	0.00	1.06	0.00	0.62	0.25	3.39	0.83	0.29	1.57	0.00	0.00
Thaumarchaeota																			
	Nitrosopumilales																		
		Nitrosopumilaceae																	
			Nitrosopumilus	0.06	0.00	0.00	0.00	0.00	0.00	0.21	0.14	3.84	0.00	0.27	0.00	0.00	0.00	0.10	0.06
	Nitrososphaerales																		
		Nitrososphaeraceae																	
			Nitrososphaera	0.18	0.11	0.00	0.00	0.00	0.00	0.10	0.00	0.38	0.00	0.00	0.08	0.00	0.00	0.00	0.00
Woesearchaeota				0.36	0.17	0.13	0.05	0.84	0.13	1.11	0.00	0.83	0.31	3.24	0.76	0.17	0.98	0.00	0.00